8-2023

Intercalation and high-pressure investigations of black arsenic phosphorus: unraveling material transformations.

Dinushika Vithanage
University of Louisville

INTERCALATION AND HIGH-PRESSURE INVESTIGATIONS OF BLACK ARSENIC PHOSPHORUS: UNRAVELING MATERIAL TRANSFORMATIONS

By

Dinushika Vithanage
B.Sc., University of Peradeniya, Sri Lanka, 2017
M.Sc., University of Louisville, Kentucky, USA, 2021

A Dissertation Submitted
to the Faculty of the
College of Arts and Sciences of the University of Louisville
in Partial Fulfillment of the Requirements
for the Degree of

Doctor of Philosophy
in Physics

Department of Physics and Astronomy
University of Louisville
Louisville, Kentucky

August 2023

INTERCALATION AND HIGH-PRESSURE INVESTIGATIONS OF BLACK ARSENIC PHOSPHORUS: UNRAVELING MATERIAL TRANSFORMATIONS

By

Dinushika Vithanage
B.Sc., University of Peradeniya, Sri Lanka, 2017
M.Sc., University of Louisville, Kentucky, USA, 2021

Dissertation approved on

July 28, 2023

by the following Dissertation Committee:

Dissertation Director
Dr. Gamini Sumanasekera

Dr. Jacek Jasinski

Dr. Ming Yu

Dr. Chakram Jayanthi

ACKNOWLEDGEMENTS

I would like to extend my heartfelt gratitude and appreciation to my esteemed supervisors, Prof. Gamini Sumanasekera and Dr. Jacek Jasinski, for their invaluable guidance and support throughout my research journey. Their expertise and mentorship have played a pivotal role in shaping me as a researcher.

First and foremost, I am immensely grateful to Prof. Sumanasekera for his continuous guidance, valuable advice, and hands-on support in designing and troubleshooting experiments. His vast knowledge in condensed matter physics has been instrumental in expanding my understanding of the field and has contributed significantly to my growth as a researcher. I am deeply indebted to Prof. Sumanasekera and his wife, Prof. Wasana Sumanasekera, for their support and assistance from the day I arrived in the United States. I would also like to extend my sincere thanks to Dr. Jasinski for his valuable support and guidance. His expertise and knowledge in materials characterization and data analysis, have played a significant role in the success of this project and has greatly inspired and contributed to my growth as a researcher. I consider myself incredibly fortunate to have had the opportunity to work under the mentorship of both Dr. Sumanasekera and Dr. Jasinski, who possess vast knowledge and genuine care for their students.

In addition, I would like to express my gratitude to Dr. Ming Yu, who not only served as a member of my dissertation committee but also played a crucial role as the lead theorist in our research group. Her theoretical calculations greatly enhanced the quality and validity of my experimental work, and I am deeply thankful for her contributions. I would also like to acknowledge Dr. C.S. Jayanthi, the Chair of the Department of Physics and Astronomy, for her valuable advice as a dissertation committee member and for providing me with the opportunity to be a part of her department as a graduate student.

Furthermore, I extend my gratitude to Dr. Manthila Rajapakse, Dr. Milinda Bharatha, Dr. Chandana Wijayasiri, and Dr. Bhupendra Karki for their invaluable support in my research work. Their assistance has played a significant role in shaping the outcomes of my study. Moreover, I feel fortunate to have had the privilege of working with lab-mates who have been not only helpful but also wonderful individuals. Special thanks to Dr. Usman Abu and Hiruni Weerahennadige for their collaboration and companionship.

I am also thankful to the staff members of the Physics Department, including Josh Rimmer, Missy Klotz, Rea Diehlmann, and others, for their support throughout my academic journey. I am grateful for the funding provided by the US Department of Energy, which made this project possible. In addition, I am thankful for the financial assistance provided by the GSC Grant and GNAS Grant, which contributed to the successful completion of this project. Further, I would like to acknowledge the support received from the Conn Center.

I am truly blessed to have the companionship and support of incredible friends like Hiruni, Dilmi, Prasadi and Ruchini, who have made me feel like family. Their presence

and encouragement have played a significant role in making this experience truly fulfilling and meaningful.

Lastly, I would like to express my deepest gratitude to my parents, my husband; Damith and my brother for their unwavering support and for everything they have done to shape me into the person I am today. Their love and encouragement have been invaluable throughout this journey. I believe that this achievement will make them proud and serve as a reminder of their unwavering support and sacrifices.

ABSTRACT

INTERCALATION AND HIGH-PRESSURE INVESTIGATIONS OF BLACK ARSENIC PHOSPHORUS: UNRAVELING MATERIAL TRANSFORMATIONS

Dinushika Vithanage

July 28, 2023

Black arsenic phosphorus (b-As_yP_{1-y}) alloys have emerged as intriguing materials within the realm of two-dimensional (2D) materials, following the discovery of black phosphorus (BP). These alloys possess capability to overcome major limitations of BP and exhibit potential for tunability and enhancement of properties making them promising materials for a wide range of applications, including lithium-ion batteries. Inspired by the intriguing findings obtained for BP, this research focuses on understanding the structural modifications that can be achieved in b-As_yP_{1-y} alloys through the application of intercalation and high pressure.

The initial phase of our investigation was dedicated to synthesizing b-As_yP_{1-y} alloys under controlled laboratory conditions using the chemical vapor transport (CVT) method. The characterization techniques revealed a structural expansion correlated with increasing arsenic (As) concentration. For the highest As concentration, segregation of a new phase (identified as g-As) from the b-As_yP_{1-y} phase was observed.

The subsequent phase focused on investigating the structural evolution of b-As_yP_{1-y} alloys during lithium (Li) intercalation, with varying As concentration (y). In-situ Raman spectroscopy was utilized to analyze the real-time vibrational modes of the alloys during Li intercalation, employing a dedicated in-situ electrochemical cell. The vibrational modes of b-As_yP_{1-y} alloys encompass a total of eight distinct modes, corresponding to P-P bonds (A^1_g, A^2_g, B_{2g}), As-As bonds (A^1_g, A^2_g, B_{2g}), and As-P bonds (two modes). A monotonic redshift of all the vibrational modes of all b-As_yP_{1-y} samples was observed during the initial stages of the intercalation process due to the softening of each mode caused by the intercalation driven donor-type charge-transfer from Li to b-As_yP_{1-y}. The emergence of a new peak identified as the E_g mode of gray As, above an intercalation threshold, is indicative of the presence of an intercalation-driven structural phase segregation process. Further, A_{1g} mode of gray As emerging after this intercalation threshold lies in close proximity of A^2_g Raman mode of As-As bonds in b-As_yP_{1-y}. All the peaks beyond the intercalation threshold show an upshift due to the co-existence of gray As with b-As_yP_{1-y} alloys causing strain and thus hardening of the phonon modes. In the sample with the highest As concentration phase segregation takes place during the synthesis process. Computational modeling reveals the co-existence of gray As in the b-As_yP_{1-y} alloys with high As concentrations. It also confirms the existence of a local structural segregation taking place at a critical Li concentration during the intercalation process.

The final stage of this project was focused on the structural evolution of b-As_yP_{1-y} alloys under hydrostatic pressure using in-situ Raman spectroscopy. High-pressure experiments were conducted using a Diamond Anvil Cell (DAC), which revealed pressure-induced shifts in vibrational modes in b-As_yP_{1-y} alloys. Two distinct pressure regimes were

observed. In the first regime (Region I), all vibrational modes exhibited a monotonic upshift, indicating phonon hardening due to hydrostatic pressure. In the second regime (Region II), $As_{0.4}P_{0.6}$ and $As_{0.6}P_{0.4}$ alloys displayed a linear blueshift (or negligible change in some modes) at a reduced rate, suggesting local structural reorganization with less compression on the bonds. Notably, the alloy with the highest As concentration, $As_{0.8}P_{0.2}$, exhibited anomalous behavior in the second pressure regime, with a downward shift observed in all As-As and As-P Raman modes (and some P-P modes). Interestingly, the emergence of new peaks corresponding to the E_g mode and A_{1g} mode of the g-As phase was observed in this pressure range, indicating compressive strain-induced structural changes. The anomalous change in Region II confirms the formation of a new local structure, characterized by elongation of the P-P, As-As, and As-P bonds along the zigzag direction within the b-As_yP_{1-y} phase, possibly near the grain boundary. Additionally, a g-As phase undergoes compressive structural changes. This study underscores the significance of intercalation and pressure in inducing structural transformations and exploring novel phases in two-dimensional (2D) materials, including b-As_yP_{1-y} alloys.

TABLE OF CONTENTS

LIST OF TABLES

LIST OF FIGURES

CHAPTER 1
INTRODUCTION & THEORETICAL BACKGROUND

Two-dimensional (2D) materials have emerged as an intriguing and rapidly expanding research field in the scope of condensed matter physics and material science. These materials possess unique physical and chemical properties due to their remarkably thin structure, setting them apart from their bulk counterparts[1]. Notably, their atomic-layered arrangement results in a high surface-to-volume ratio, enabling enhanced interaction with the surrounding environment and heightened responsiveness to external factors[2]. Additionally, 2D materials exhibit impressive mechanical strength, further contributing to their intriguing characteristics. Their reduced dimensionality gives rise to extraordinary properties, making them highly promising for a wide range of applications, including electronics[3, 4], optoelectronics[3, 5], photonics[6], energy storage[7-9], energy conversion[10], superconductors[11], catalysis[12, 13], and sensors[2].

Following the revolutionary discovery of graphene, a diverse range of 2D materials, including phosphorene[14], hexagonal boron nitride (h-BN) [15, 16], silicene[17], germanene[18], MXenes[19] and transition metal dichalcogenides (TMDs)[20], have been discovered and extensively investigated, broadening new avenues. Phosphorene, also known as black phosphorus (BP) in its bulk form, has attracted significant attention, as the newest member of the 2D material family. Its unique properties, such as a tunable

direct bandgap (0.3 eV and 2 eV for bulk[21] and monolayer[22] BP, respectively), high carrier mobility[23-25], and strong in-plane anisotropy[26], render it suitable for use in photonic, thermoelectric, sensing, and optoelectronic applications. However, its rapid degradation in the environment limits its durability and potential applications. By alloying phosphorus with arsenic, the environmental stability of BP can be enhanced while preserving its unique structure and properties[27]. This alloying process allows for the precise tuning of their characteristics, inspiring research advancements and interest in b-As_yP_{1-y} alloys.

1.1. Black Arsenic Phosphorus

The metastable form of arsenic; black arsenic (b-As), exhibits similar electronic and optical properties[28,29] to BP, including its orthorhombic puckered honeycomb crystal structure. Consequently, further modifications to BP have been made by alloying it with the congener material arsenic, resulting in b-As_yP_{1-y} alloys. These alloys possess unique crystal structure, high anisotropy, electrical[30], optical[31], and thermal[32],[33] properties similar to BP, but with modifications. Various applications based on b-As_yP_{1-y} alloys have been reported to date, including Er-doped fiber ultrashort laser generators[34], thermoelectronics[33], photonic microheaters[35], and Li-ion batteries[36]. The bandgap of b-As_yP_{1-y} alloys can be tuned down to approximately 0.15eV, indicating their potential as promising candidates for mid-infrared photodetectors.[37-40] Experimental reports confirm that of b-As_yP_{1-y} alloy-based photodetectors exhibit high detectivity beyond 4.9 x 10^9 Jones in the mid-infrared range of 3- 5 μm.[37] As b-As_yP_{1-y} alloys have a similar orthorhombic honeycomb puckered structure as BP (with slight changes), they possess strong in-plane anisotropic optical absorption and Raman scattering.[39] Furthermore, a monolayer of b-As_yP_{1-y} can be a highly

efficient donor in solar cells due to its high electronic mobility and direct band gap of 1.54eV, according to theoretical reports.[41] Overall, b-As_yP_{1-y} alloys exhibit outstanding thermal, optical, electrical, and photoelectric properties, including a very narrow bandgap, anisotropic infrared absorption, and bipolar transfer characteristics, making them promising for infrared photodetectors and high-performance field effect transistors (FETs)[42].

1.1.1. Crystal structure

Elements of group V are known to form two types of layered structures, the α (A17) phase and β (A7) phase. The α phase has an orthorhombic honeycomb puckered crystal structure with the space group *Cmca*. The β phase is a rhombohedral buckled layered crystal structure with the space group *R3m*. For phosphorus, the α phase, known as BP, is stable, while the β phase, known as blue phosphorus, is unstable under ambient pressure. Unlike BP, most stable allotropes of other pnictogens are in β phase which has rhombohedral crystal structure that exist as gray As, gray Sb and metallic Bi[43]. Figure 1.1 shows the structures of (a) gray As (g-As), (b) black As (b-As), (c) BP, and (d) blue P. For each of the V_yP_{1-y} (V = As, Sb, Bi) systems, a critical composition is expected to transform between the α phase and the β phase.

G-As has the buckled structure analogous to Blue P[44]. BP has the honeycomb puckered structure, along with overall orthorhombic lattice symmetry. Chen et al. has reported b-As, the analogue of BP with an orthorhombic puckered layered crystal structure, being an extremely anisotropic layered semiconductor crystal[28], with higher or comparable electronic, thermal, and electric transport anisotropies between the armchair (AC) and

zigzag (ZZ) directions than any other known 2D crystals. Hence, b-As opens a pathway to novel research ideas and applications. However, the abundance of naturally occurring b-As is very limited. Since it is a metastable phase, impurities are necessary for its stabilization.

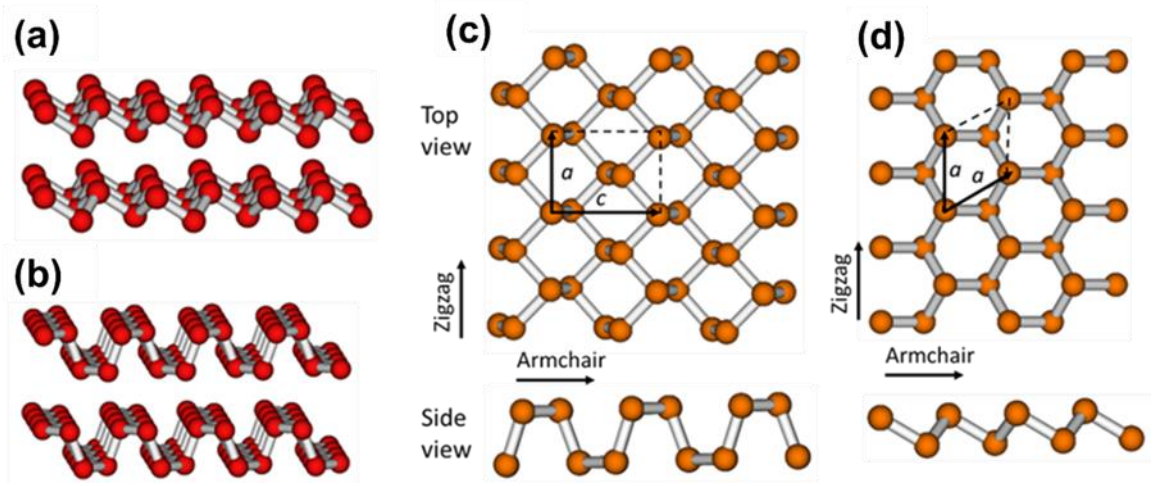

Figure 1.1: Structures of (a) rhombohedral (gray) arsenic, and (b) orthorhombic arsenic[43], (c) Top and side views of black phosphorene (orthorhombic), and (d) blue phosphorene (rhombohedral). The red and yellow balls denote the As and P atoms, respectively.

1.1.2. Characteristics of b-As_yP_{1-y}

Above mentioned exotic properties make As to be a promising candidate to be alloyed with BP, while preserving or enhancing its unique properties and overcoming its drawbacks. Gas-transport synthesis process is expected to transform a mixture of g-As and red P into b-As_yP_{1-y} alloys with orthorhombic crystal structure for a wide range of stoichiometries ($0 < y < 0.83$)[11]. However, since As atoms are much larger in diameter than P atoms, As atoms in the primitive unit cell show slight outward displacement, which results in increased unit cell parameters[45,30]. A relative lattice expansion of 0.0645 is

reported with increasing As concentration[33]. Accordingly, volume of the unit cell also increases with increasing As concentration. Therefore, these b-As_yP_{1-y} alloys have strong in-plane covalent bonding and weak interlayer van der Waals (vdW) interactions, sharing the common features with many other layered 2D materials.[39] With different compositions, b-As_yP_{1-y} alloys have many unique properties analogous to BP. Strong in-plane anisotropic properties of b-As_yP_{1-y} alloys are revealed by polarization-resolved infrared absorption measurements.[45] Furthermore, based on infrared absorption measurements, Liu et al. have reported decrease of the band gap with increasing As concentration of b-As_yP_{1-y} alloys [39]. Specifically, the band gap of bulk materials can be tuned over a range of 0.3eV to 0.15eV when As concentration changes from y = 0 to 0.83. Theoretical calculations predict that monolayer As-P possess electron mobility of ~10 000 $cm^2V^{-1}s^{-1}$ which is 10 times higher than phosphorene[46]. Back-gate field-effect transistors (FETs) fabricated by Liu et al. using b-$As_{0.83}P_{0.17}$ have shown a hole mobility of 110 $cm^2V^{-1}s^{-1}$, an ambipolar transport behavior and an on/off current ratio of 1.9×10^3.[39] The broad and high photoresponsivity of b-$As_{0.83}P_{0.17}$ in the mid-infrared (MIR) region, along with higher air stability facilitated by h-BN encapsulation, makes it a promising photodetector and opens to applications in MIR region, such as space communication, infrared imaging, and biomedical sensing.[38] b-As_yP_{1-y} alloys with higher energy storage capabilities than pure BP and good Coulombic efficiencies show promising potential for use in Li-ion batteries (LIBs). For example, Luxa et al. has reported b-As_yP_{1-y}-based LIBs with capacities over 1000 $mAhg^{-1}$ in the first discharge cycle.[36] However, poor cycling and a capacity loss, upon subsequent cycling have been measured for those structures. This signifies the need for continued research on improving properties and performance of such LIBs.

The incorporation of As into the BP structure, resulting in b-As_yP_{1-y}, offers significantly enhanced resistance to degradation compared to BP when exposed to oxygen and humidity. The stabilization of the thermoelectric power (TEP) in $As_{0.4}P_{0.6}$ occurs at a slower rate than in BP, showing a 1.4 times difference, while BP's resistance decay is four times faster than that of $As_{0.4}P_{0.6}$ under ambient conditions. This divergence in behavior can be attributed to the closer redox potential of b-As_yP_{1-y} to O_2/O_2^- (-4.5 eV) compared to BP, reducing charge transfer effects and degradation at the surface-water interface. As a result, b-As_yP_{1-y} alloys address the primary limitation of BP and demonstrate potential as viable alternatives in various applications[27].

Further modifications to lattice structure can be made by application of external stimuli. External factors cause strain on the lattice structure, resulting in changes in its electronic structure, subsequently affecting properties such as bandgaps, electrical properties, magnetic properties, optical properties, thermal conductivities, catalytic properties, phase transition, and interlayer coupling.[47] Alloying, intercalation, and inducing high-pressure are well-known methods used to modify crystal structures. Additionally motivated by previous work reported, this study extensively examines the structural changes of b-As_yP_{1-y} under charge transfer and high-pressure utilizing numerous characterization methods.

1.2. Introduction to Intercalation

Introducing foreign atoms or ions in between layers of host material is known as intercalation. The weakly bonded layers in two-dimensional (2D) materials allows for the accommodation of intercalants, making them highly favorable host materials. Intercalation

plays a powerful role in modifying the interlayer interactions, doping, and modifying electronic structure of these materials. This technique also enables the transformation of materials into entirely distinct structures or phases, making it a critical tool for controlling the properties of layered materials, facilitating their transition across phase diagrams, and triggering significant structural transformations across diverse applications[48]. In the field of intercalation, a range of strategies have developed. These include chemical intercalation, which involves intercalation from gaseous[49, 50] or liquid[49, 51] phases, as well as electrochemical intercalation, which employs solid[52, 53] or liquid[54-56] electrolytes.

1.2.1. Intercalation Mechanism

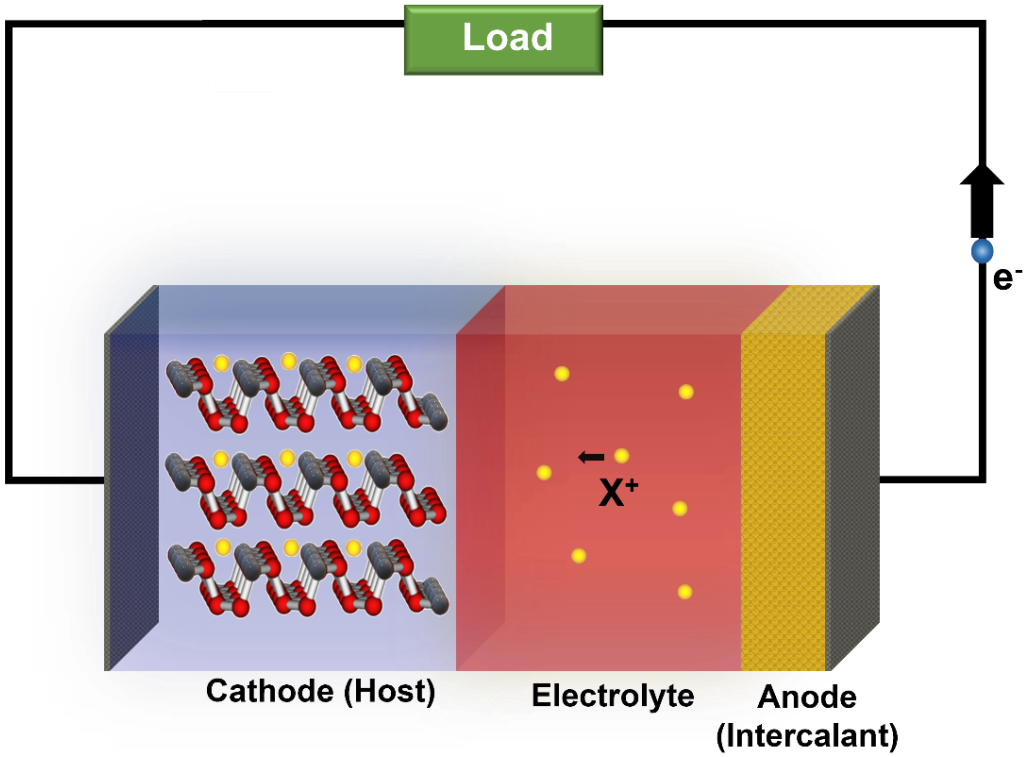

Figure 1.2: Schematic of electrochemical intercalation

In this study, the electrochemical intercalation method was employed due to its high controllability over the process. The intercalation process was manipulated by applying an external bias between the electrodes, enabling real-time characterization. In electrochemical intercalation, a typical electrochemical cell arrangement was utilized, with the intercalant serving as the anode and the host material functioning as the cathode (figure 1.2).

The migration of ions was facilitated by the presence of an ionically conducting liquid or solid-state electrolyte, which was driven by the application of current or voltage in the system. When using a liquid electrolyte, ions exhibit higher mobility compared to a solid electrolyte, and the voltage profile of intercalation compounds is well-defined in liquid electrolytes. Precise doping levels in electrochemical intercalation can be achieved by controlling the applied electrochemical voltage or current[57]. The specific concentration of intercalated species plays a crucial role in fine-tuning material properties, facilitating comprehensive experimental studies, and fostering potential advancements in the field of two-dimensional (2D) materials.

Intercalants can be classified as either donor or acceptor compounds depending on their contribution. In the process of intercalation, materials with donor characteristics contribute electrons and integrate into the interlayer spaces of the host material. The electrochemical reaction can be symbolically expressed as:

$$H + xD^{+} + xe^{-} \Longrightarrow DxH$$

where, H and D are host material and donor species, respectively[8]. Alkaline and alkaline earth metals, including Li, Na, and Mg, are extensively employed as donor-type intercalants in the investigation and practical utilization of layered materials[58-61].

In contrast, acceptor-type intercalants, accept electrons from the host material and intercalate into the interlayer spaces of the host material, during the intercalation process. These intercalants tend to have a higher electron affinity and can effectively capture and incorporate electrons from the host lattice, resulting in changes to the electronic structure and properties of the material. Examples of acceptor-type intercalants include $FeCl_3$[57], H_2SO_4[62] and others. Electrochemical reaction of acceptor type can be represented as,

$$H + xA^- \Rightarrow AxH + xe^-$$

where A is the acceptor compound. Electrochemical intercalation exhibits enhanced reversibility, facilitating efficient intercalation process[49].

1.2.2 Application of Intercalation

The intercalation of alkali metals like lithium is of great interest due to their unique properties and potential applications in energy storage devices, such as rechargeable lithium batteries. In the case of graphite, which is often used as an anode material in Li-ion batteries (LIBs), intercalation of lithium in layered materials like graphite offers several advantages for energy storage applications. It allows for the reversible insertion of charge carriers into the interlayer spacing of the electrode, which helps to avoid problems associated with standard electrochemical reactions, such as volumetric expansion and strain generated during charging/discharging cycles.

Since, BP has been explored for its use in Li and Na ion batteries, effect of intercalation using different intercalants, including Li, Ca, K, Rb[63], I, and NH_3 with BP[64] have been studied quite extensively. Transmission electron microscopy (TEM)[65] and Raman[54] *in-situ* characterization techniques allows to observe time evolution changes during Li intercalation. Specifically, while TEM provides *in-situ* direct visualization, *in-situ* Raman probing reveals fundamental insight into changes in atomic vibrational modes. *In-situ* Raman study of electrochemical Li intercalation into BP by Rajapakse et al. has shown that, in addition to peak broadening, a monotonic red shift corresponding to A_g^1, B_{2g} and A_g^2 phonon modes takes place due to lithiation-induced structural expansion[54]. However, there has been hardly any work reported on *in-situ* Raman study on electrochemical Li intercalation in b-As_yP_{1-y} alloys, yet. Only work that has been done so far comprises of few theoretical and experimental research on applicability of b-As_yP_{1-y} in Li ion batteries. However, one of the main problems with this material is its rapid environmental degradation and limited durability. The problem of fast degradation, within a matter of hours/days for phosphorene, especially in the presence oxygen, and light has been studied and well documented[66-69]. Recently, our group has demonstrated that alloying with arsenic enhances the environmental stability of BP, while preserving the unique structure and material's properties[27].

Here, in this work, we study lithium intercalation into b-As_yP_{1-y} alloys, as this is relevant to the application of these materials in LIBs. In addition, the intercalation process can also induce significant changes in the host material's structure, electronic properties, and even its crystallographic arrangement. For example, the intercalation of lithium ions into certain transition-metal dichalcogenides (TMDs) can modulate their catalytic

performance[70]. Additionally, intercalation of lithium in materials like MoS_2 can result in enhanced phonon scattering, c-axis strain, and stacking disorder, leading to unique thermal properties[71]. Therefore, understanding the intercalation process of lithium in b-As_yP_{1-y} alloys can led to designing and optimizing these alloys with tailored properties for various applications.

1.3. Introduction to High-pressure Phenomena

The application of strain is a highly effective approach for tuning the properties of two-dimensional (2D) materials. Among the numerous techniques available for inducing strain, the utilization of pressure is a promising method that prevents introducing defects into the material's structure. It offers significant advantages in the synthesis of new material phases with enhanced properties and in the exploration of existing phases. Under high pressure conditions, crucial material characteristics, including interatomic distances, electron configuration, density, and free energy, can be deliberately modified[72]. Significantly, pressure exerts a great influence on the equilibrium of reactions, rendering it vital in the fabrication of metastable materials. A number of thermodynamically metastable materials, synthesized under high-pressure conditions, demonstrate remarkable kinetic stability over extended periods when exposed to ambient pressure. The high-pressure synthesis of metastable materials holds considerable importance as it provides access to novel and valuable substances.

High-pressure research is heavily dependent on techniques. The primary tools utilized in the high-pressure science and technology are diamond-anvil cells (DACs) and

'large-volume' synthesis presses. These tools encompass designs such as the 'belt', multi-anvil, toroidal, and piston-cylinder configurations, accompanied by large-scale shockwave facilities[73]. In recent years, significant progress in instrumentation and techniques has extensively broadened the scope of experiments feasible in high-pressure research. The diamonds utilized in the diamond anvil cell (DAC) exhibit transparency to a wide spectrum of electromagnetic radiation, making the DAC compatible with a wide array of characterization techniques. Notably, the DAC facilitates various probing techniques, including X-ray and neutron diffraction, as well as spectroscopic methods such as Raman spectroscopy, Fourier transform infrared (FTIR) spectroscopy, and photoluminescence (PL) spectroscopy. Recent advancements in the design of diamond anvil cells have enabled to achieve pressures on the order of 10^{12} Pa [74]. Present-day laboratory conditions allow for achieving pressures in the range of 10^{14} Pa via shock waves. However, when considering the universe, the highest known pressures exist within the cores of neutron stars, found to be in magnitudes around 10^{30} Pa.

1.3.1. Phase Transitions in the Context of Gibbs Energy (G)

The Gibbs free energy (G) of a system is a measure of the amount of usable energy that can do work in the system. The stability of the final phase in a structural transition process is determined by the Gibbs free energy (G) of the system. To achieve the equilibrium phase at specific temperature and pressure, it is necessary to minimize the Gibbs free energy of the system during the transition process. The following explains Gibbs free energy,

$$G(P, T) = U + PV - TS$$

where U is the internal energy, P is pressure, V is the volume, T is the temperature and S is the entropy. In high-pressure experiments, the system involves external parameters such as pressure (P) and temperature (T), while other variables within the Gibbs free energy function (such as U, V, and S) are allowed to adjust freely in order to minimize Gibbs free energy. In other words, these experiments are conducted within the framework of a statistical constant pressure ensemble.

With an increase in pressure, the distances between atoms or molecules within a material decrease, causing the lattice to compress. This compression induces modifications in the potential energy between these entities, thereby influencing their interactions and ultimately impacting the Gibbs energy of the system. The change in Gibbs free energy (ΔG) during a process provides valuable insights into the energetics and spontaneity of the reaction. Under high pressures, the landscape of Gibbs energy in the material experiences modifications, favoring particular configurations of atoms or molecules that minimize the system's overall energy. The compressed lattice enables the formation of stronger chemical bonds or the rearrangement of atoms into more stable arrangements.

The rate at which a process transforms from its initial state to the final equilibrium is determined by the activation energy, also known as kinetic barriers[75]. Figure 1.3 represents the energy profile diagram. In cases where the transformation rate is lowered due to a high kinetic barrier, and there exists a metastable phase with a lower energy barrier, the crystal may undergo a transformation to the metastable phase instead of the stable one[76]. Many metastable phases exhibit such lengthy lifetimes that they cannot be experimentally distinguished from equilibrium phases. Remarkably, semiconductor materials naturally

exhibit a progressive tendency to transform into denser structures through a series of high-pressure structural transitions. Due to their metastability and the intrinsic inclination towards high-pressure phase changes, investigations of semiconductors under high pressure hold significant importance.

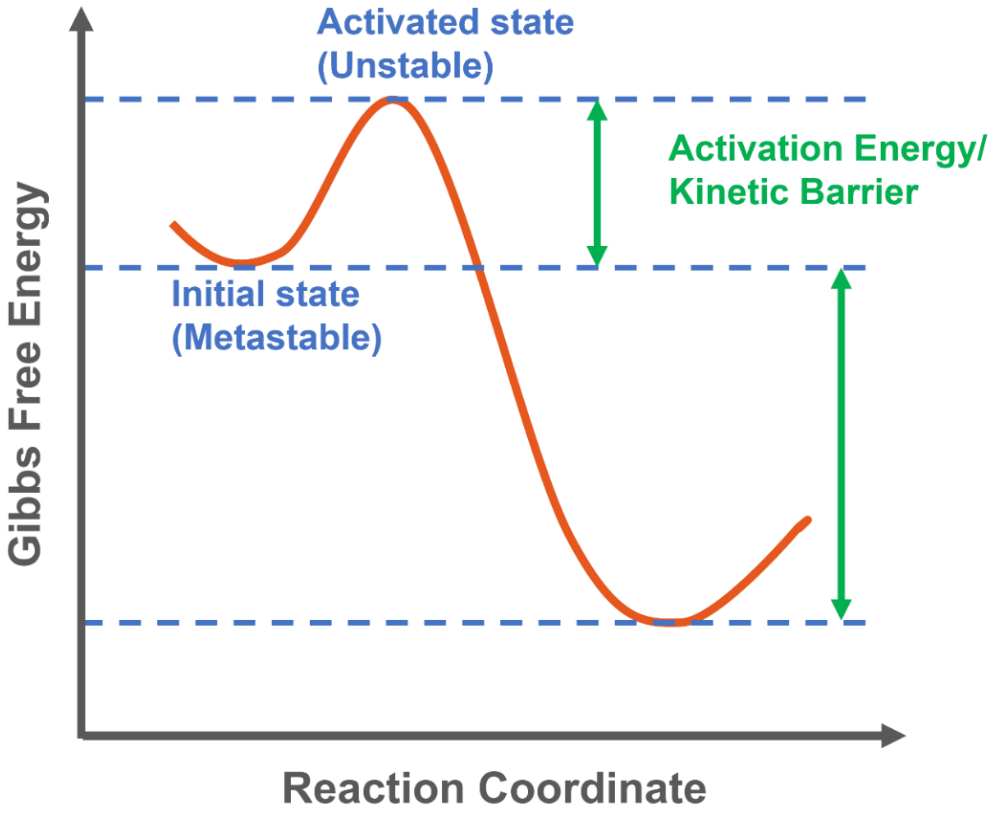

Figure 1.3: Energy Profile Diagram of a Phase Transformation.

Understanding the energy transformation during high-pressure conditions, is essential for predicting and controlling phase transitions and the formation of stable phases in materials. It provides valuable insights into the behavior of materials under extreme pressure and facilitates the design and synthesis of novel materials with tailored properties.

1.3.2. Application of High-pressure

Strained 2D materials have been extensively studied over the years. Particularly, first-principal calculations predict that lithium-intercalated BP, under high-pressure conditions, could transform into the blue-P structure. However, experimental work by Rajapakse et al. has shown that high pressure applied to intercalated BP induces structural reorganization in BP[77]. Interestingly, recent work by Chaofeng Gao et al. reported a phase transition from b-As to gray arsenic (g-As)[78] under high pressure. It has been observed that the onset of g-As structure occurs at a critical pressure 3.48 GPa, and both b-As and g-As coexists between 3.48 and 5.37 GPa before b-As completely converts to g-As above 5.37 GPa. The process has been shown to be reversible up to 3 GPa, with a conversion of back to b-As. However, above 5.37 GPa, the transformed g-As structure remains even after pressure was released[78]. Previous studies on Li intercalation to b-As_yP_{1-y} alloys complement the result obtained by Chaofeng Gao et al, as they have also reported a Li-intercalation driven phase transition of b-As_yP_{1-y} alloys (α phase) to a rhombohedral structure (β phase)[78] with the emergence of new peaks characteristic of gray arsenic after a critical degree of lithiation. The coexistence of both phases indicates a partial phase transition due to lithiation. However, the response of b-As_yP_{1-y} alloys under high pressure has not been studied thus far, despite their intriguing properties and potential applications.

Apart from the previously mentioned investigations on Li intercalation, this study additionally focuses on understanding the effect of high-pressure on the crystal structure of b-As_yP_{1-y} alloys by investigating their vibrational modes using in-situ Raman spectroscopy. Specifically, the study examines the structural variations of b-As_yP_{1-y} alloys with varying As concentrations under hydrostatic pressure generated by a Diamond Anvil

Cell (DAC). Tuning properties under strain is important for achieving high-performance devices and exploring new opportunities.

CHAPTER 2

EXPERIMENTAL TECHNIQUES

2.1. Synthesis of b-As_yP_{1-y} alloys

2.1.1. Chemical Vapor Transport (CVT) Method

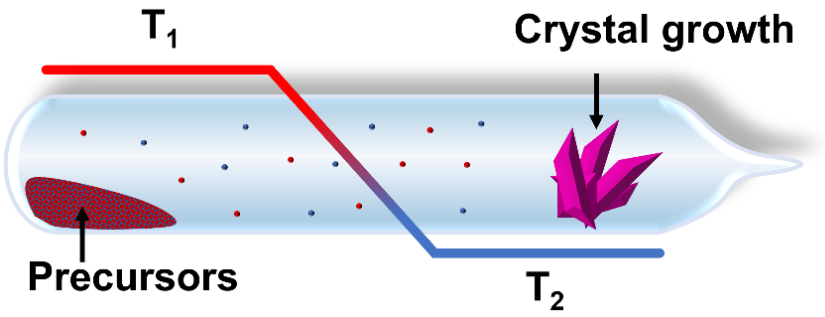

Figure 2.01: Schematic of CVT crystal growth. T_1 and T_2 indicate high and low temperature zones, respectively.

Chemical vapor transport (CVT) method is used to synthesize b-As_yP_{1-y} alloys followed by our previous work[33]. In the CVT method, precursor solid material is transported from a source to a cooler region by means of a chemical vapor. This technique involves the vaporization of the source material at a high temperature followed by its subsequent crystallization or condensation at a lower temperature region. The schematic diagram illustrating the process is shown in Figure 2.01.

As precursors, stoichiometric amounts (molar ratios) of red phosphorus (Sigma, >97%) and gray arsenic (Sigma, 99.99%) of total weight of 300 mg were added into a quartz ampoule along with Sn (10 mg, Alfa Aesar, 99.8%) and SnI_4 (5 mg, Alfa Aesar, >95%) as mineralizing agents. Open end of the quartz ampoule including precursors was connected to the high vacuum system consisting mechanical pump and a diffusion pump as shown in figure 2.02 and figure 2.03. Then it was evacuated down to 10^{-6} Torr. While maintaining ampoule under the vacuum, it was sealed using oxy acetylene flame torch, melting from the constriction (figure 2.04).

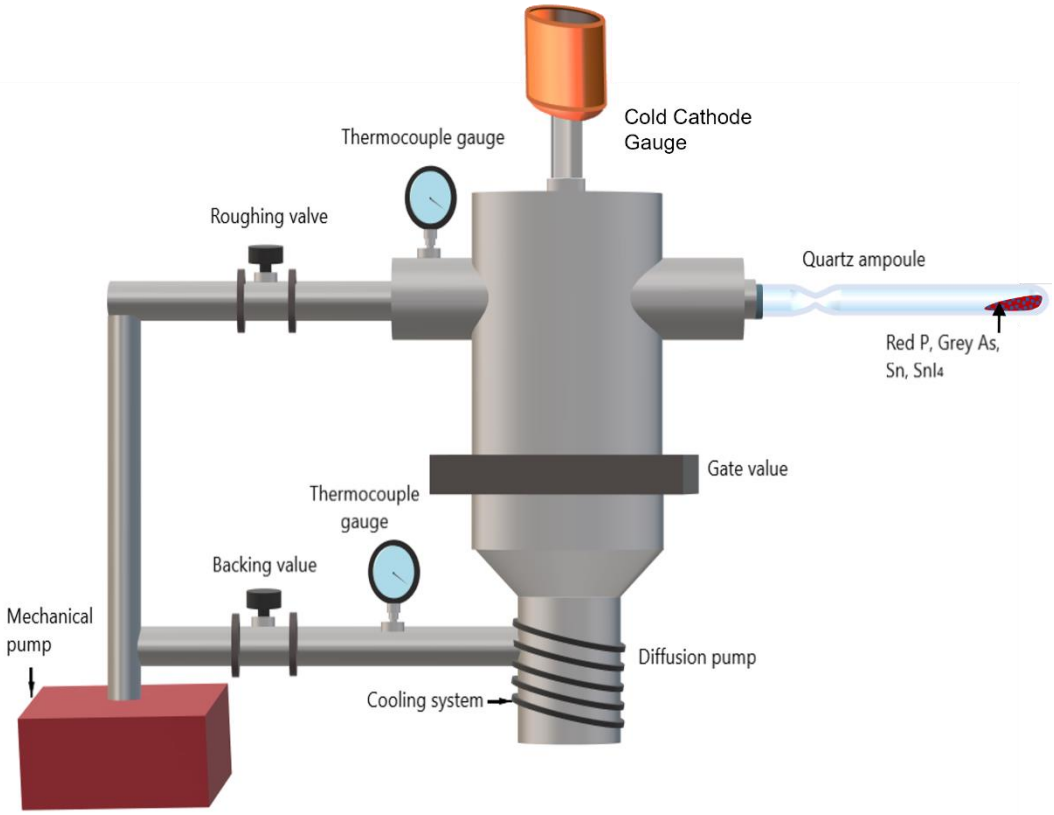

Figure 2.02: Schematic diagram of high vacuum system

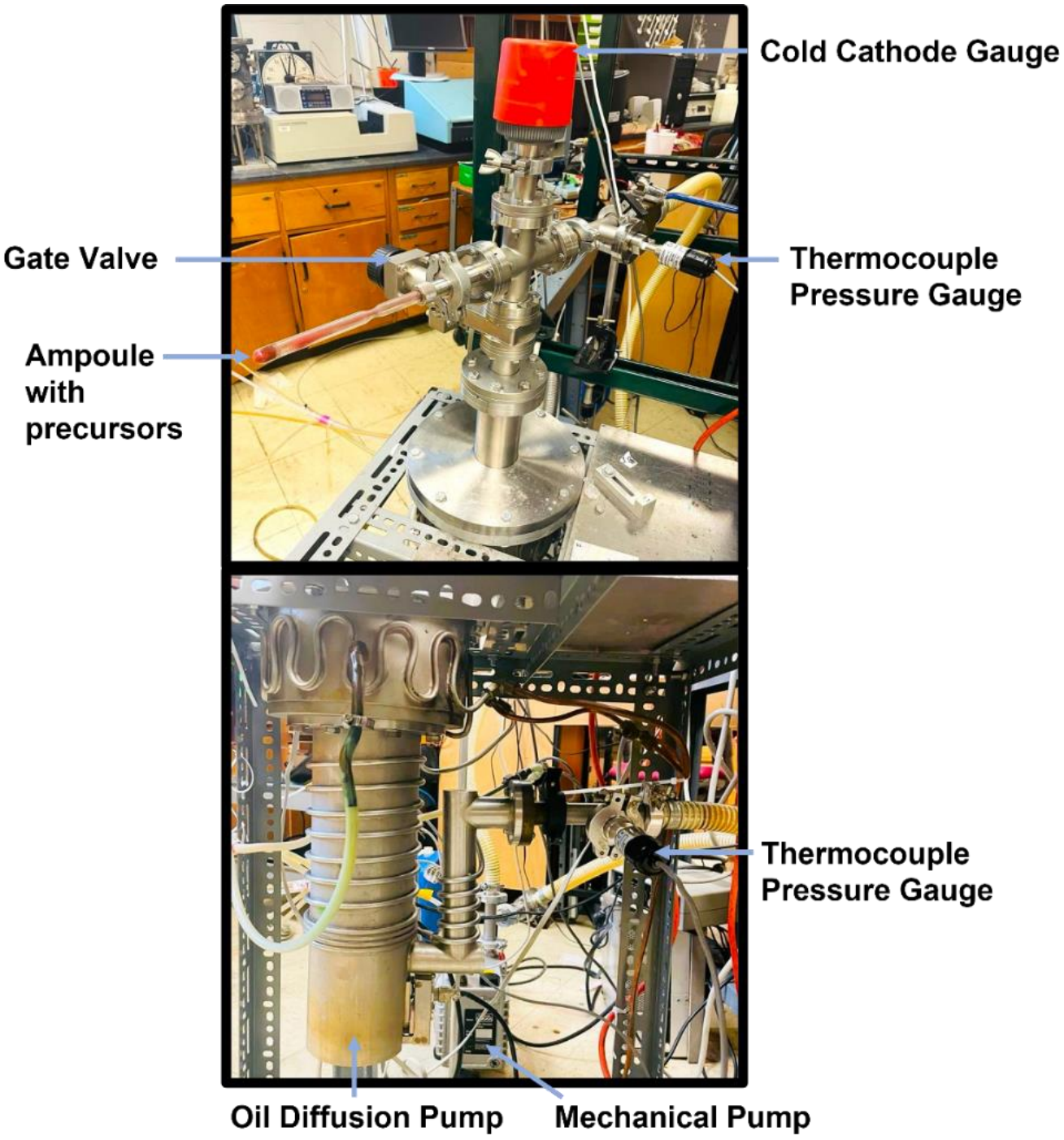

Figure 2.03: The high-vacuum system

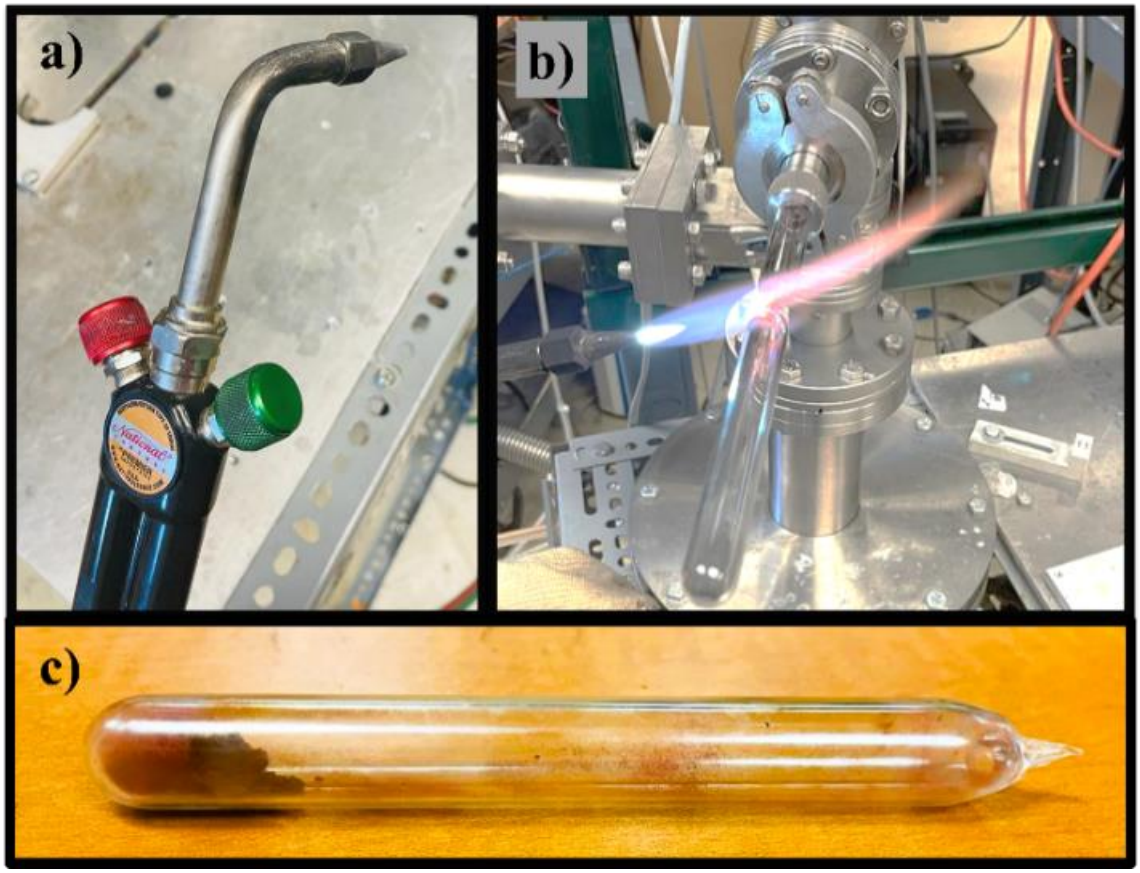

Figure 2.04: a) Oxy-acetylene torch b) Tube sealing using Oxy-acetylene torch c) Sealed ampoule.

Quartz ampoules were used because it can stand higher temperatures due to its high melting point of 1650°C. Pyrex ampoules start to rupture due around 610°c. These quartz ampoules are custom built by Custom Glassblowing of Louisville, Inc. Having a total length of 18.4cm and the constriction is made 7.6cm from open end for easier sealing without causing damage to the vacuum system due to heat of the oxy acetylene flame torch. It made it difficult to seal quartz, since the melting point of quartz is higher. Therefore, wall thickness of quartz ampoules was customized to reduce to 1.25mm. However, it required careful control of oxy acetylene flame torch to seal quartz ampoules. Thin walls of quartz ampoules were not able to endure, vapor pressure during crystal growth. Hence,

amount of precursors used were reduced to 300mg to avoid explosion of the ampoule during heating.

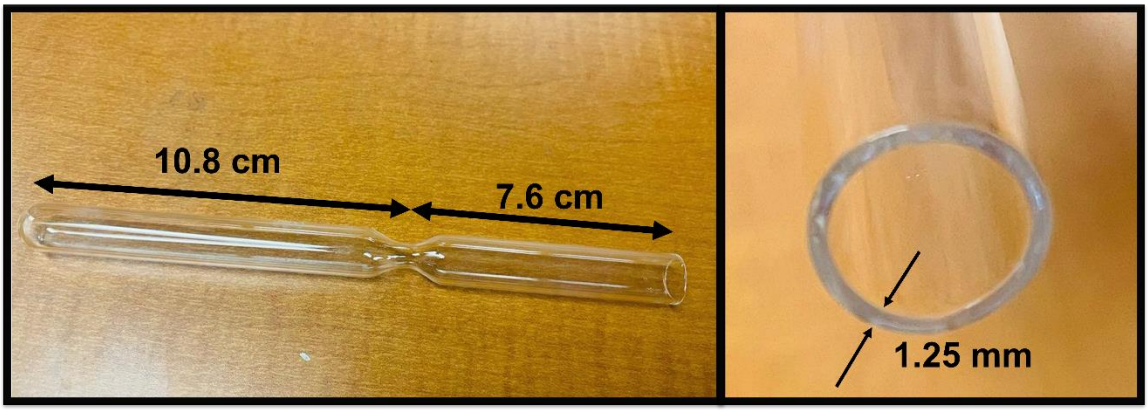

Figure 2.05: The quartz ampoules used for sample synthesis.

Sealed ampoule was placed in a two-zone furnace. (The furnace included three individually programmable zones, but only two-zones were used for this work). A temperature difference of 50°C was maintained between the hot zone and the cold zone of the furnace. Sealed ampoule was placed in a two-zone furnace, with precursors at the hot end. Then the temperature at the hot end was increased to 650 °C from 3hours, maintained it for 1 hour and slowly cooled down in 15hours in steps. Detailed temperature profile is shown in figure 2.06(b). Resultant As_yP_{1-y} alloys were grown in the cold end.

Synthesized series of As_yP_{1-y} alloys include, $As_{0.2}P_{0.4}$, $As_{0.4}P_{0.6}$, $As_{0.5}P_{0.5}$, $As_{0.6}$P0.4 and $As_{0.8}P_{0.2}$. Figure 2.07 shows an image of a synthesized black arsenic phosphorus alloy. Then the alloys were characterized via Raman, EDX and XRD spectroscopic techniques and SEM, TEM microscopic techniques. Detailed characterization information is discussed in the results section.

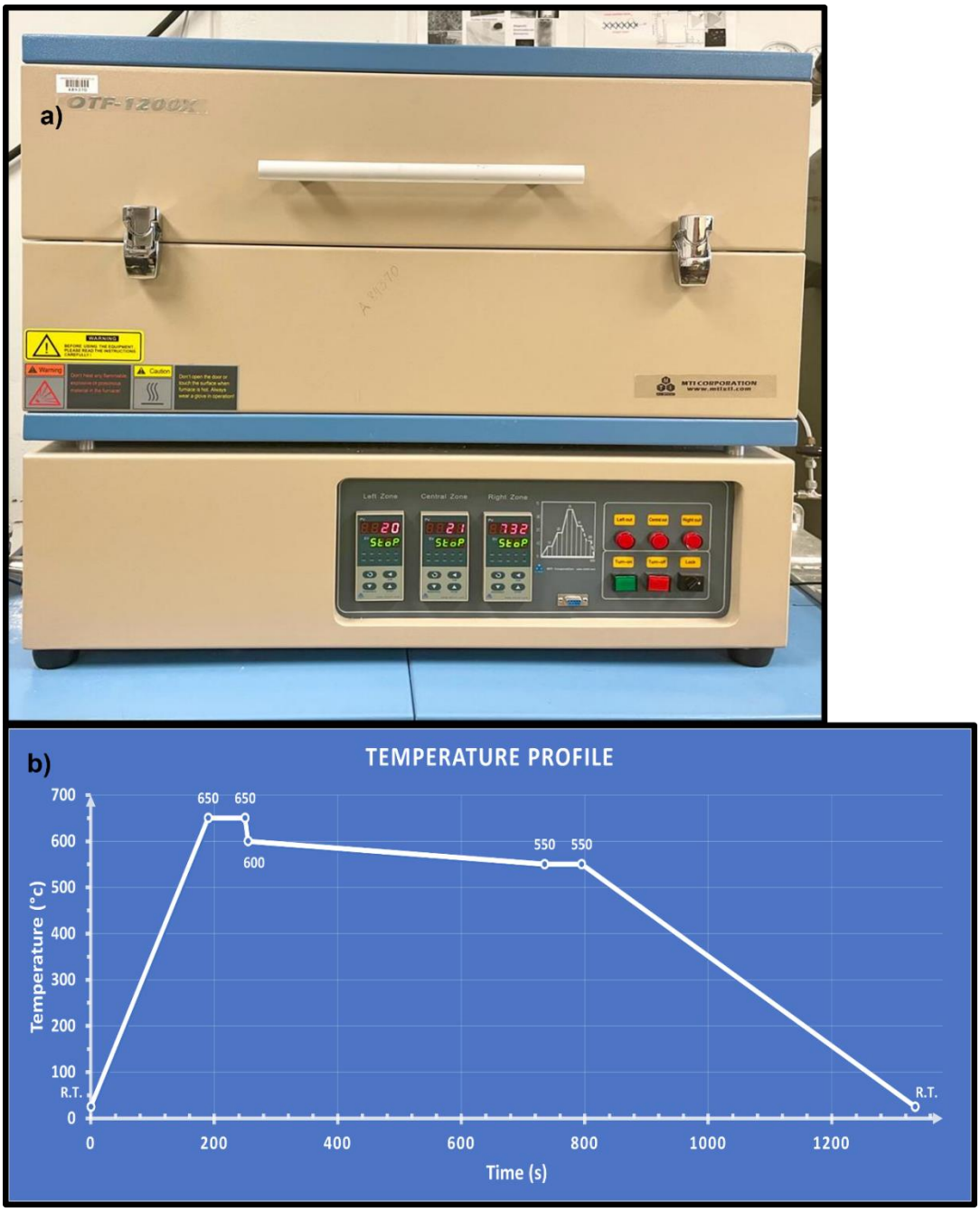

Figure 2.06:(a) The two-zone furnace (b) Temperature profile at the hot end.

Figure 2.07: Black arsenic phosphorus alloy

2.2 Characterization Techniques

Spectroscopic Techniques

A spectroscopic technique is a method that utilizes electromagnetic radiation (light) to interact with matter to extract valuable information about its properties. The measurement and analysis of the interaction between light and a sample, results in a spectrum that provides information about the sample's composition, structure, and other characteristics.

There are various spectroscopic techniques, each utilizing different regions of the electromagnetic spectrum (e.g., ultraviolet, visible, infrared, microwave, etc.) and specific principles of interaction (e.g., absorption, emission, scattering) to gather information about the sample. Spectroscopic characterization techniques involved in the presented work include, Raman spectroscopy, Photoluminescence spectroscopy (PL), X-ray diffraction spectroscopy (XRD), Energy Dispersion X-ray spectroscopy (EDS or EDX). In addition, microscopic methods involved are Transmission Electron Microscopy (TEM) and

Scanning Electron Microscopy (SEM). Each technique has its own distinctive range of capacities. Henceforth, the general principles underlying each technique and the revealed characteristics of series of As_yP_{1-y} alloys will be discussed.

2.2.1 Raman Spectroscopy

Raman spectroscopy is a widely utilized technique based on the principle of light scattering or photon interaction. The phonon energies associated with a specific material, produces a distinctive Raman spectrum for each material, analogous to a unique fingerprint, offering valuable insights into molecular vibrations, as well as the chemical and structural characteristics of the observed material. The discovery of this effect can be credited to Indian physicist C.V. Raman (1888-1970), who was awarded the Nobel Prize in 1930 for his pioneering work. With the advent of commercial lasers in the 1960s, Raman spectroscopy has gained widespread use as a technique for material characterization.

Raman scattering manifests when a sample is subjected to a monochromatic light source, commonly a laser. A small fraction (approximately 1%) of the incident photons/light undergoes scattering, while the majority of photons transmit through the sample. During this process, an incident photon encounters an electron within the sample, resulting in the absorption of photon energy and the subsequent excitation of the electron to a virtual higher energy state. Subsequently, the electron transitions from the virtual state to a lower energy state, emitting a scattered photon. The disparity in energy between the scattered and incident photons distinguishes light scattering into three distinct types.

Elastic scattering of photons corresponds to Rayleigh scattering, in which the scattered photon retains the same energy as the incident photon. Although, Rayleigh scattering is dominant, it does not yield substantial spectral information.

Raman scattering is a phenomenon associated with the inelastic scattering of photons. It can be further classified into two types: Stokes scattering and Anti-Stokes scattering. Stokes scattering occurs when the scattered photon possesses lower energy than the incident photon. The energy difference observed in Stokes scattering arises from the absorption of energy, leading to the creation of a phonon—a quantum of vibrational energy. Consequently, the excited electron remains in a higher energy state than its initial state.

Conversely, in Anti-Stokes scattering, the excited electron (in the virtual state) transitions to a lower energy level compared to its initial state. As a result, the scattered photon possesses higher energy than the incident photon. This additional energy is acquired through the absorption of a phonon. Referring to the energy level diagram presented in Figure 2.08, the equations for energy conservation can be expressed as follows.

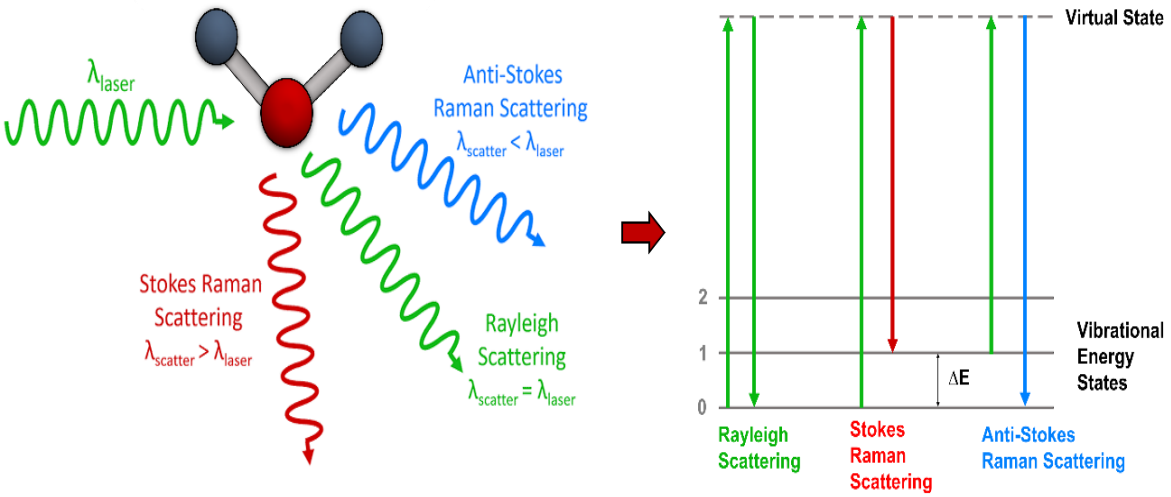

Figure 2.08: Schematic representation and energy states diagram illustrating scattering phenomenon.

$h\nu_i = h\nu_s$; Rayleigh's scattering

$h\nu_i = h\nu_s + \Delta E$; Stokes scattering

$h\nu_i = h\nu_s - \Delta E$; Anti-stokes scattering.

where,

h – Plank's constant

ν_i – frequency of the incident photon

ν_s – frequency of the scattered photon

ΔE- energy of the phonon

Then $h\nu_i$ is the energy of the incident phonon and $h\nu_s$ is the energy of the scattered phonon.

Through measurement and analysis of the energy shifts (wavelength differences) between the scattered photons and the incident photons, Raman spectroscopy yields valuable information regarding the vibrational energy levels and associated molecular structure of the sample. The resulting Raman spectrum exhibits distinctive peaks or bands, each corresponding to specific vibrational modes of the molecular species within the sample.

A Raman spectrometer typically consists of a laser source, a sample holder, a monochromator, a detector, and a data analysis system. The diagram of a Raman spectrometer is shown in figure 2.09. The Raman system employed in this study includes a He-Ne red laser with a wavelength of 633 nm. A 50-X Nikon objective lens (T Plan EPI SLWD) with a 22 mm working distance was used in the Leica microscope integrated into

the Raman spectrometer. White light is used during target selection and focus, and a 633nm red light laser is used for exposure. Raman spectra were collected using a Renishaw inVia spectrometer (figure 2.10), which incorporated a charge-coupled device (CCD) detector and a 1200 lines per millimeter grating. The spectrometer offered an effective resolution of 0.5 cm^{-1}.

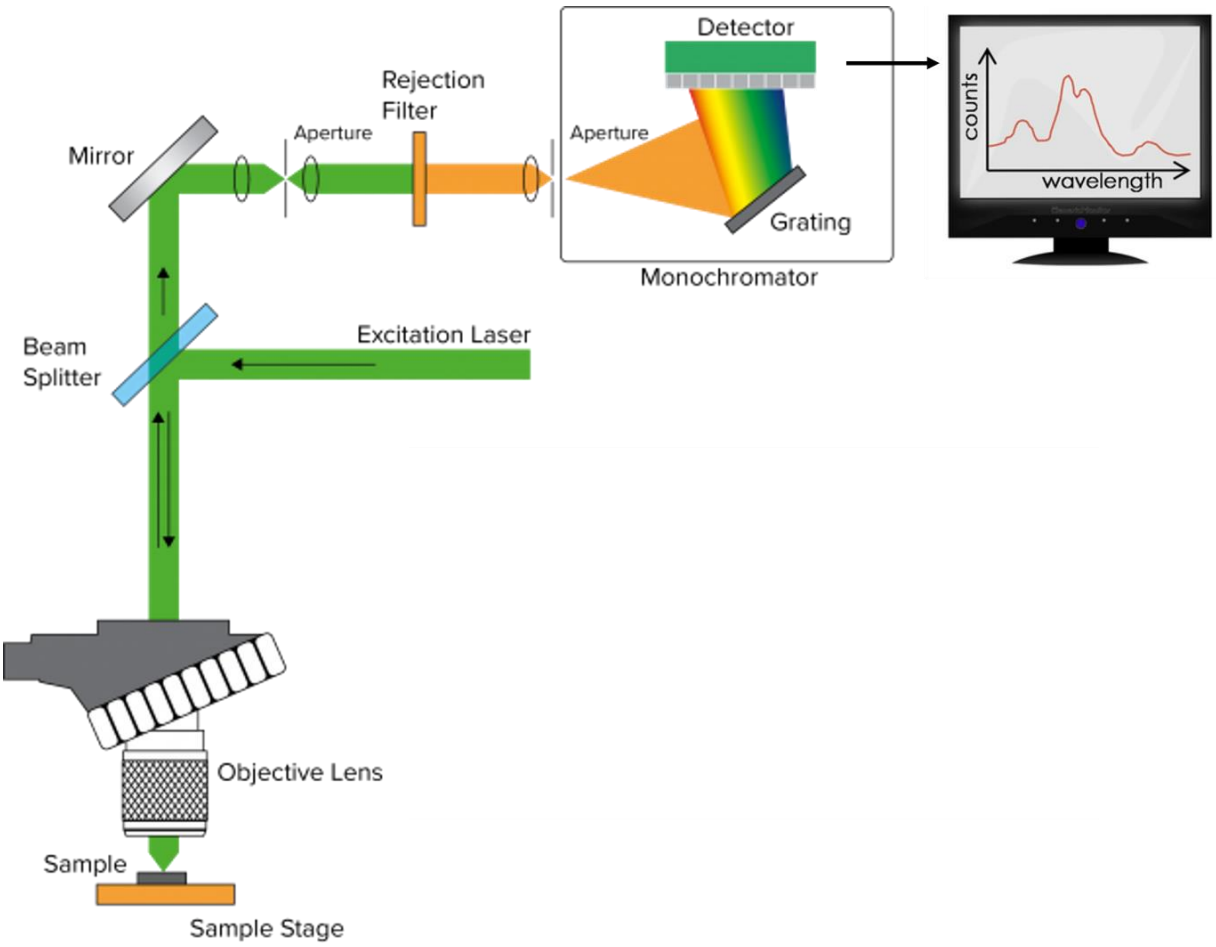

Figure 2.09: Schematic diagram of a Raman spectrometer illustrating the key components and the light path for Raman scattering analysis.

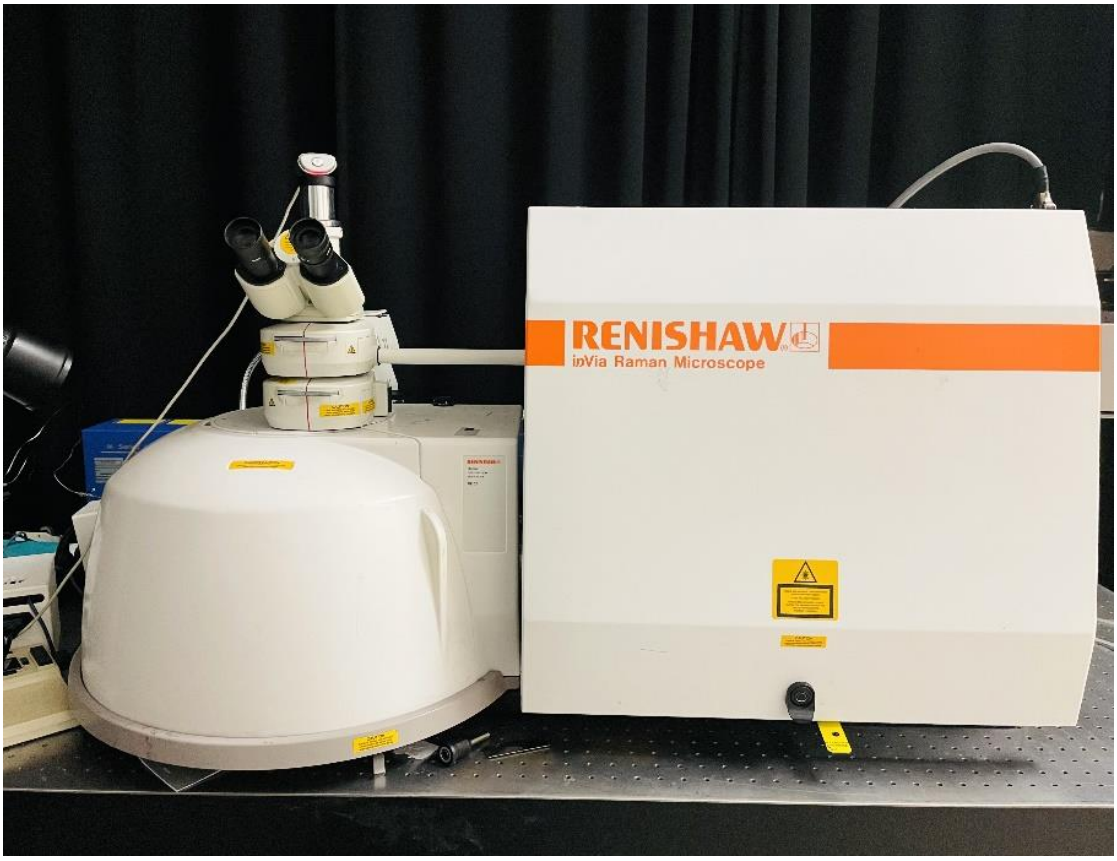

Figure 2.10: The Renishaw inVia Raman spectrometer

Beyond its role in identification, Raman spectroscopy exhibits sensitivity to variations in material structure induced by external factors such as intercalation and pressure. These external factors influence the vibrational energies of the material, making Raman spectroscopy a valuable tool for studying the systematic evolution of material structures under different conditions. This capability has been extensively employed in the investigation of series of black arsenic phosphorous in this study.

As previously mentioned, Raman spectroscopy provides a spectrum of vibrational energies for a material. A crystalline material can be modeled as a mass-spring system, allowing vibrations to occur along various spatial directions within the material. These vibrations, referred to as vibrational modes, manifest as distinct peaks in the Raman

spectrum. However, it is important to note that not all vibrational modes are Raman-active, meaning not all modes appear in the Raman spectra. For a vibrational mode to be Raman-active, it must induce a change in molecular polarizability.

For instance, black phosphorous (BP) exhibits a total of 12 atomic vibrational modes[79] (also known as phonon modes). Within this set, six modes are classified as Raman-active, two modes are infrared-active, three modes are acoustic, and one mode is silent.[80,79,81] Among the six Raman active modes, only three modes are experimentally observable in bulk black phosphorus (BP). It is discussed in detail in the next chapter.

2.2.2 Photoluminescence Spectroscopy

Photoluminescence (PL) spectroscopy is a valuable tool for studying how materials emit light when excited by photons. It reveals the optical and electronic properties of materials. The main light interaction method used in photoluminescence is the absorption of photons and subsequent emission of light by materials. When a material is illuminated with photons of higher energy (typically from a light source such as a laser), the photons can be absorbed by the atoms or molecules within the material. This absorption promotes electrons to higher energy levels or excited states (photo - excitation). Figure 2.11 illustrates energy state diagram of the photoluminescence phenomenon.

After a short period of time, the excited electrons return to their lower energy states, releasing the excess energy as photons. This emitted light is the photoluminescence signal. The wavelength of the emitted light is generally longer than that of the absorbed photons due to energy losses within the material.

There are two main types of photoluminescence: fluorescence and phosphorescence. Fluorescence happens when excited electrons quickly return to their original states, emitting light within a very short time. Phosphorescence involves a slower process, where the emission of light continues even after the excitation source is removed.

Therefore, the primary interaction method in photoluminescence is the absorption of photons by the material, followed by the re-emission of light as the excited electrons relax to lower energy levels. Photoluminescence spectroscopy finds extensive application in various fields, including but not limited to determining band gaps, evaluating material quality, investigating molecular structure and crystallinity, studying recombination mechanisms, as well as detecting impurity levels and defects.

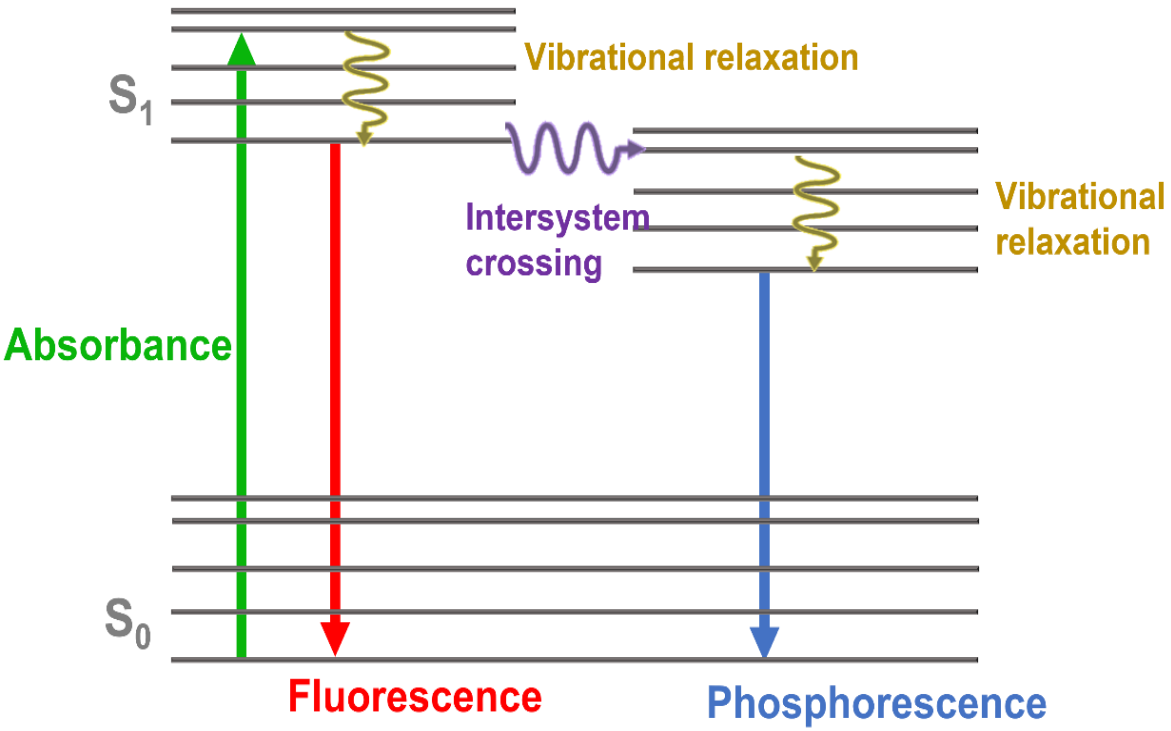

Figure 2.11: Energy states diagram illustrating the photoluminescence phenomenon.

The Renishaw InVia Raman spectrometer facilitates the performance of photoluminescence spectroscopic measurements. Pressure calibration inside the diamond anvil cell (DAC) in high-pressure experiments is conducted using the photoluminescence spectra of Ruby, which will be discussed in detail in this chapter.

2.2.3. X-ray Diffraction (XRD)

X-ray diffraction (XRD) is a nondestructive analytical technique widely utilized to investigate both physical and chemical properties of crystalline powders, thin films, epitaxial films, and bulk solid materials. Generally, its applications include the determination of crystal structure, lattice parameters, phase composition, as well as the measurement of crystallite size, strain, and the degree of crystallinity in amorphous materials. XRD offers invaluable insights into the spatial arrangement of atoms within crystalline substances, enabling the characterization and understanding of their structural characteristics at the atomic and molecular levels.

X-ray wavelengths, due to their comparable range to atomic sizes and interatomic spacings, offer a valuable tool for acquiring atomic-scale information. When a monochromatic and collimated X-ray beam interacts with a crystalline sample, the lattice structure of the crystal leads to the diffraction of the X-rays at specific angles. This diffraction phenomenon gives rise to a distinctive pattern of diffracted X-rays, where constructive or destructive interference occurs in accordance with Bragg's law. As a consequence, distinct peaks manifest at specific angles within the diffraction pattern (see figure 2.12).

$$2d\ sin\theta = n\lambda$$

where, d- the distance between atomic layers

θ – The angle between the incident X-ray and the sample surface

λ- the wavelength of the incident X-ray

n- an integer (diffraction order)

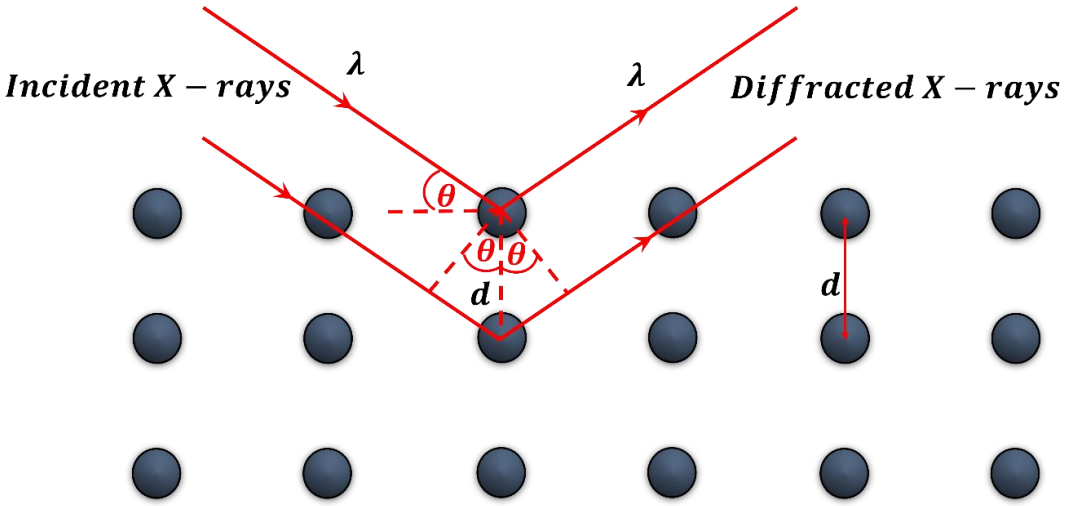

Figure 2.12: Schematic representation of Bragg's law

A typical x-ray diffractometer includes essential components such as an x-ray source, sample holder, and x-ray detector. Either the sample holder or the x-ray source can be rotated, allowing for the adjustment of the incident angle θ. At each incident angle, the x-ray detector records the intensities of diffracted x-rays at an angle 2θ. Consequently, a graph illustrating the intensity as a function of 2θ, commonly referred to as an x-ray diffraction pattern, is obtained.

The X-ray diffraction (XRD) system scans the sample over a range of diffraction angles to obtain peaks that correspond to atomic planes in crystalline specimens. Analyzing the XRD peak pattern allows identification of crystalline phases, quantification of phase composition, calculation of residual stress from lattice parameters, characterization of crystallite size and micro strain from peak broadening, and analysis of epitaxial film growth. XRD provides valuable insights into the structural and compositional properties of crystalline materials.

The materials included in this project were characterized using the Bruker D8 Discover X-ray diffraction (XRD) instrument for XRD analysis (see figure 2.13). The acquired XRD spectra were carefully analyzed using the Diffrac eva software, in accordance with crystallographic data obtained from the ICCD PDF-2 database. Through this analysis, various crucial parameters were determined, including phase identification, lattice parameter determination, and Miller indices identification, among others.

Furthermore, the GSAS II software was employed to perform a comprehensive fitting and analysis of the XRD data, enabling a more detailed exploration and interpretation of the obtained results. The XRD data obtained are discussed in detail in the following chapter.

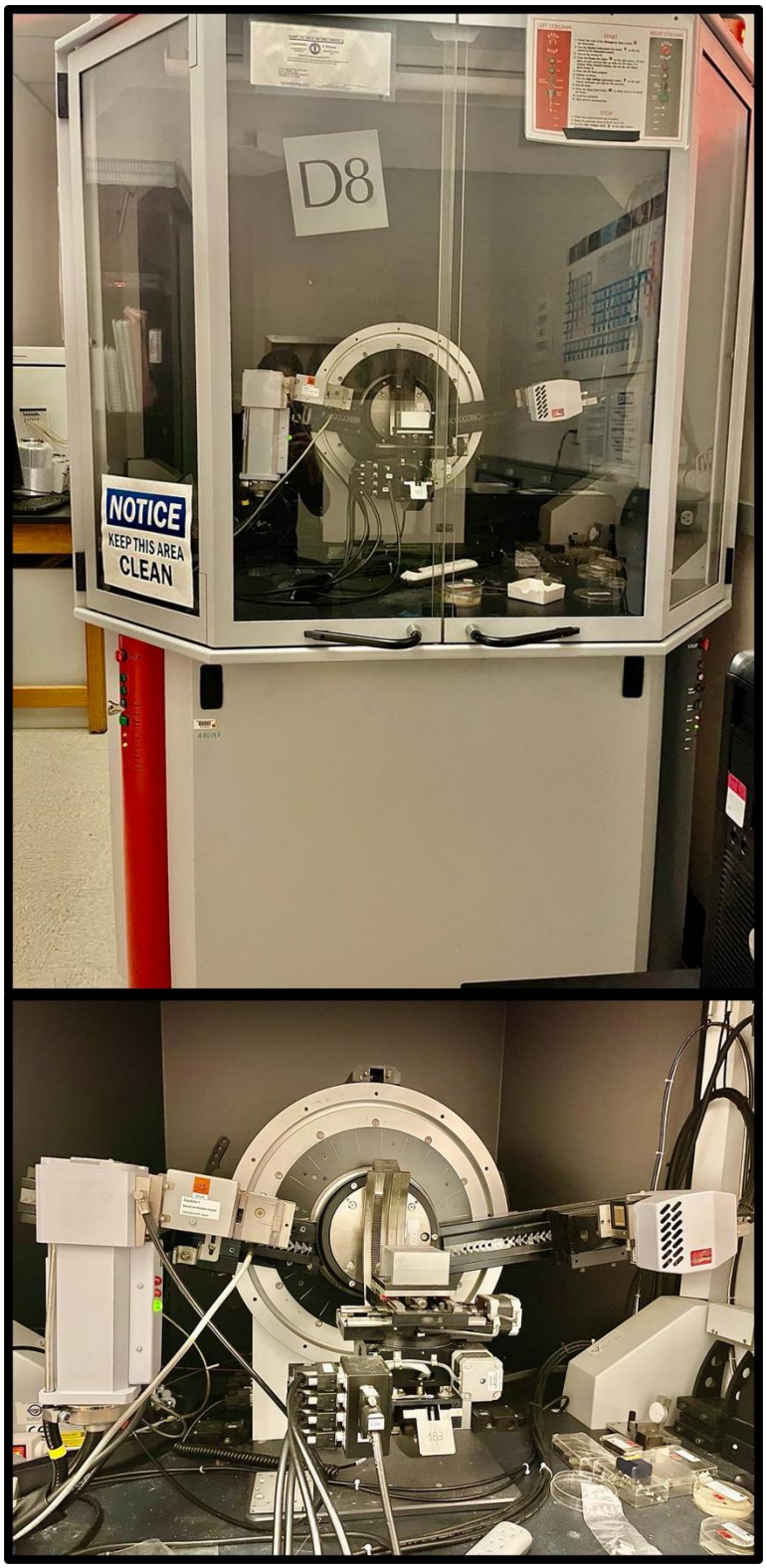

Figure 2.13: The Bruker D8 Discover X-ray diffractometer.

Microscopic Techniques

2.2.4. Scanning Electron Microscope (SEM)

Scanning Electron Microscopy (SEM) is an advanced imaging technique employed for the examination of surface morphology and topography of materials at high resolution. It utilizes a focused electron beam to interact with the sample, generating various signals that provide valuable information about the surface characteristics.

During SEM analysis, the specimen is placed within a vacuum chamber, and an electron gun produces a focused beam of electrons. Magnetic lenses are employed to precisely focus the electron beam onto the sample surface (see figure 2.14). When the primary electron beam interacts with the sample, multiple signals are generated, including secondary electrons (SE), backscattered electrons (BSE), and characteristic X-rays.

Secondary electrons are low-energy electrons emitted from the sample surface due to their interaction with the primary electron beam. These electrons convey detailed information regarding the surface topography and morphology of the sample.

Backscattered electrons, on the other hand, are high-energy electrons that are deflected or scattered back from the atomic nuclei of the sample. BSE signals provide contrast in composition and sensitivity to the average atomic number of the elements present in the sample. Furthermore, the primary electron beam can also displace inner-shell electrons within the sample, leading to the emission of characteristic X-rays when these vacancies are filled by outer-shell electrons. These X-rays carry elemental information about the composition of the sample.

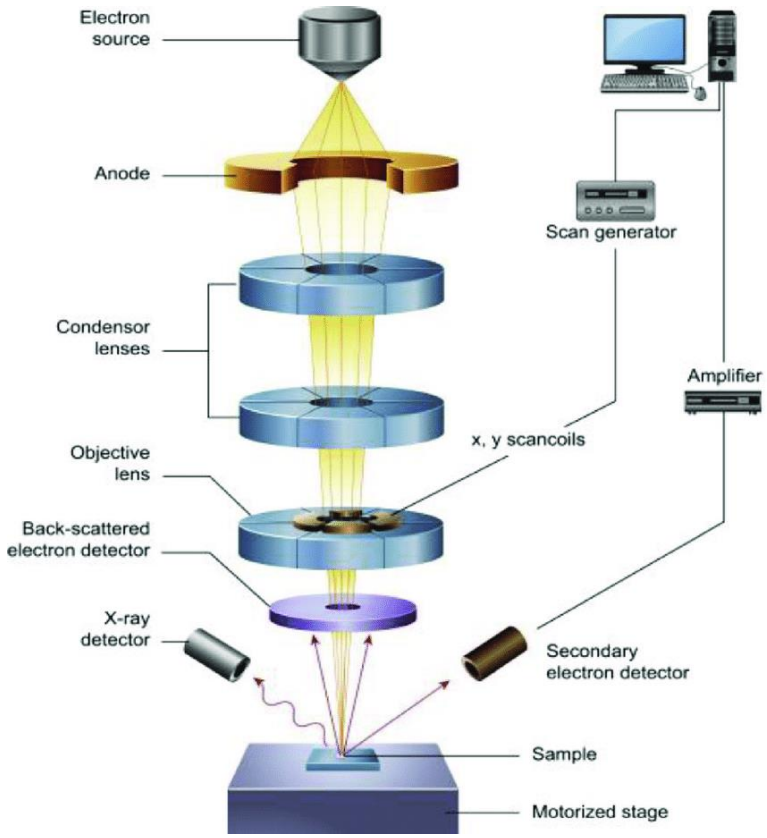

Figure 2.14: Schematic diagram of a Scanning Electron Microscope[82, 83]

The signals resulting from the electron-sample interaction are collected by detectors, which then transform them into images and spectra. SEM images provide highly resolved, three-dimensional representations of the sample surface, enabling detailed examination and analysis of its microstructure, particle size, and surface features.

SEM finds extensive applications across various scientific and industrial domains, including materials science, nanotechnology, biology, geology, and forensic science. It

serves as a powerful tool for investigating surface properties, morphology, and elemental composition of diverse samples.

2.2.5. Energy Dispersive X-ray Spectroscopy (EDS or EDX)

In addition to its imaging capabilities, SEM is commonly coupled with Energy-Dispersive X-ray Spectroscopy (EDX or EDS) to enable elemental analysis. In a typical SEM, when the electron beam collides with the samples, they interact with the beam and produce characteristic X-rays. These X-rays can be used to distinguish and measure the concentration of different elements in the sample because each element has a unique X-ray emission spectrum [84]. The X-rays result from the interaction of the primary electron beam with the nucleus of the sample's atoms. The primary electron beam excites the electrons in the atom's nucleus, causing one of them to be ejected and creating an electron hole. An electron from the outer shell of the atom then fills the electron hole, releasing the excess energy as the emitted X-ray. The emitted X-ray consists of both the X-ray continuum, generated by the deceleration of electrons, and the characteristic X-ray, produced when higher shell electrons fill the electron hole in the nucleus shell[85].

EDX analysis provides invaluable insights into the chemical composition and elemental distribution within the specimen. It enables the identification of specific elements, quantification of their concentrations, and spatial mapping of their distribution

across the sample. The sample characterization was performed using the TESCAN Vega3 SEM equipped with an EDX system, which is shown in figure 2.15.

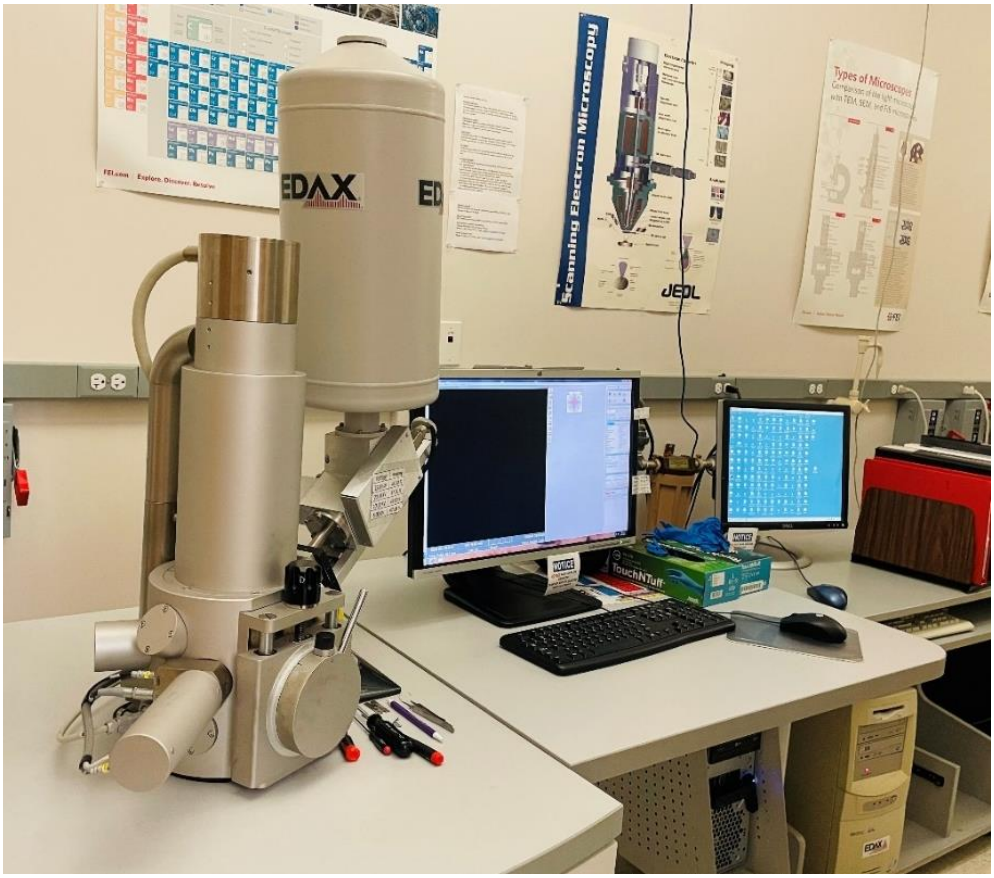

Figure 2.15: TESCAN Vega3 SEM

2.2.6. Transmission Electron Microscope (TEM)

Transmission Electron Microscopy (TEM) is a sophisticated imaging technique extensively employed in the fields of materials science and nanotechnology to investigate the microstructure and properties of materials at the atomic scale. By utilizing an accelerated beam of electrons, TEM enables the observation of internal features and morphology within a specimen, typically with a thickness of less than 100 nm.

TEM surpasses the magnification and resolution capabilities of optical microscopes, allowing the visualization of atomic-scale details. This enhanced resolution is attributed to the short wavelength of electrons, which is significantly smaller than that of visible light. Unlike scanning electron microscopes, which primarily examine sample surfaces, TEM provides higher resolution images by employing electromagnetic lenses to focus the electron beam and control its trajectory. Consequently, TEM is widely utilized to examine nanoscale surface roughness, crystallinity, defects, porosity, composition, and internal structure of materials.

However, TEM requires specimens that are semi-transparent to electrons and have a thickness below 100 nm. Conventional TEM systems, particularly those with high voltage and high resolution, necessitate high vacuum conditions to prevent electrical arcing and minimize electron collisions with gas atoms.In TEM, a high-energy electron beam is generated by an electron gun and directed onto a thin specimen using electromagnetic lenses (figure 2.16). As the electron beam passes through the specimen, it interacts with the atoms, undergoing scattering and diffraction processes. The unscattered transmitted electrons form an image on a fluorescent screen or are detected by a charge-coupled device (CCD) camera, revealing the internal structure of the specimen. Although the transmitted electrons contribute to the image formation, a fraction of the incident electrons may also scatter from the sample. Scattered electrons can be blocked using an aperture.

TEM offers several imaging modes, including bright-field imaging, dark-field imaging, and high-resolution imaging. These techniques provide valuable information about crystal structure, defects, grain boundaries, and other microstructural features of the sample.

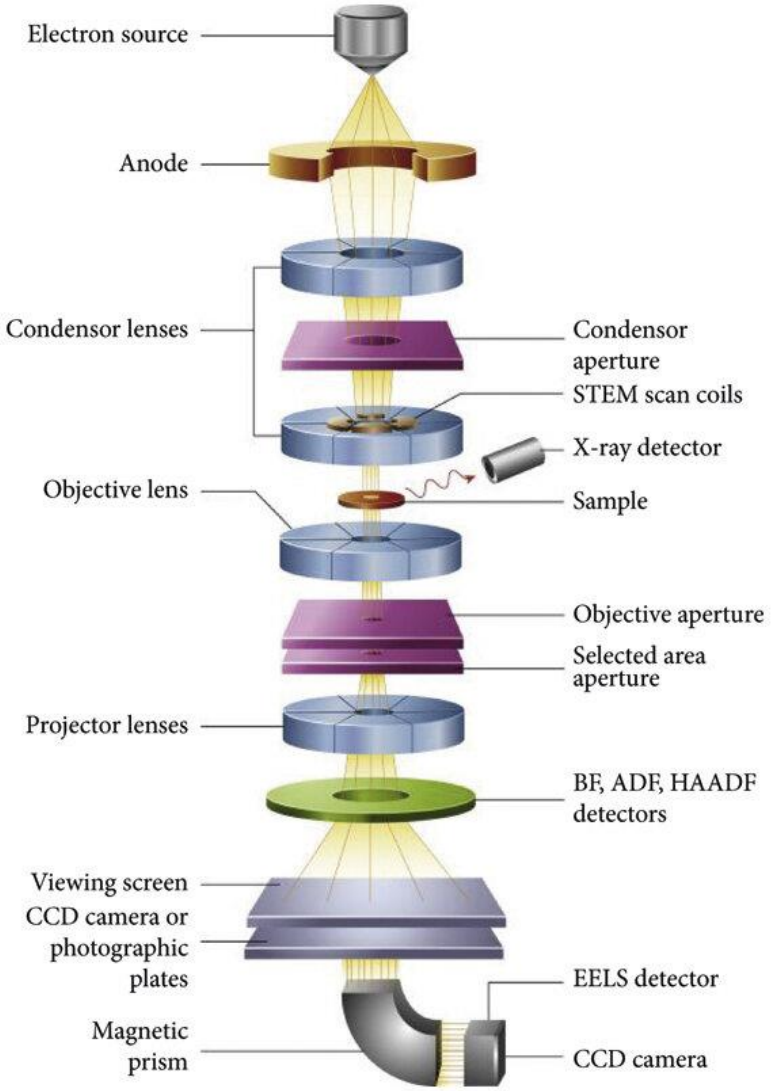

Figure 2.16: Schematic diagram of Transmission Electron Microscope (TEM)[86]

Additionally, TEM exploits the wave-particle duality of electrons, similar to the behavior of X-ray beams in X-ray diffraction (XRD). In TEM, the electron beam can also diffract upon interacting with the sample. When suitable conditions are met, the diffracted electrons can interfere constructively, allowing the application of Bragg's law. The resulting electron diffraction pattern from a specific crystalline sample comprises bright spots, with each spot representing a distinct crystallographic plane.

Figure 2.17: FEI Tecnai F20 FEG-TEM/STEM system.

The analysis of electron diffraction patterns aids in the identification of essential crystallographic information, such as the orientation of atomic planes and atomic arrangements. This capability is known as selective area electron diffraction (SAED), as the user can conveniently select the area of interest within the sample for diffraction pattern generation using a selected area aperture. In this study, high-resolution TEM images of black arsenic phosphorus were acquired using a 200-kV FEI Tecnai F20 FEG-TEM/STEM system (figure 2.17).

2.3. Electrochemical Li intercalation

Electrochemical intercalation, which involves the insertion of guest atoms or molecules into the crystal structure of host material, has been employed utilizing a conventional cell configuration resembling that of lithium-ion batteries. In an electrochemical cell, there are two key components: electrodes and an electrolyte. Specifically, Li serves as the anode material, while the cathode is composed of b-As_yP_{1-y} alloys. During the discharging process, lithium ions (Li^+) diffuse through the electrolyte from the electrochemically oxidized anode and intercalate into the cathode.

In order to investigate the intercalation process in real-time via in-situ Raman spectroscopic technique, a specially designed split test cell, manufactured by MTI Corporation, was employed. This Raman cell includes a transparent quartz window, which enables a direct observation of the electrode of interest. Consequently, the transparent window allows the focused laser beam from the Raman spectrometer to be directed onto the b-As_yP_{1-y} electrode. As a result, it becomes feasible to perform real-time characterization while the intercalation process is ongoing. Schematic of the setup is shown in figure 2.18. Both the external appearance and internal schematic of the in-situ cell are illustrated in Figure 2.19.

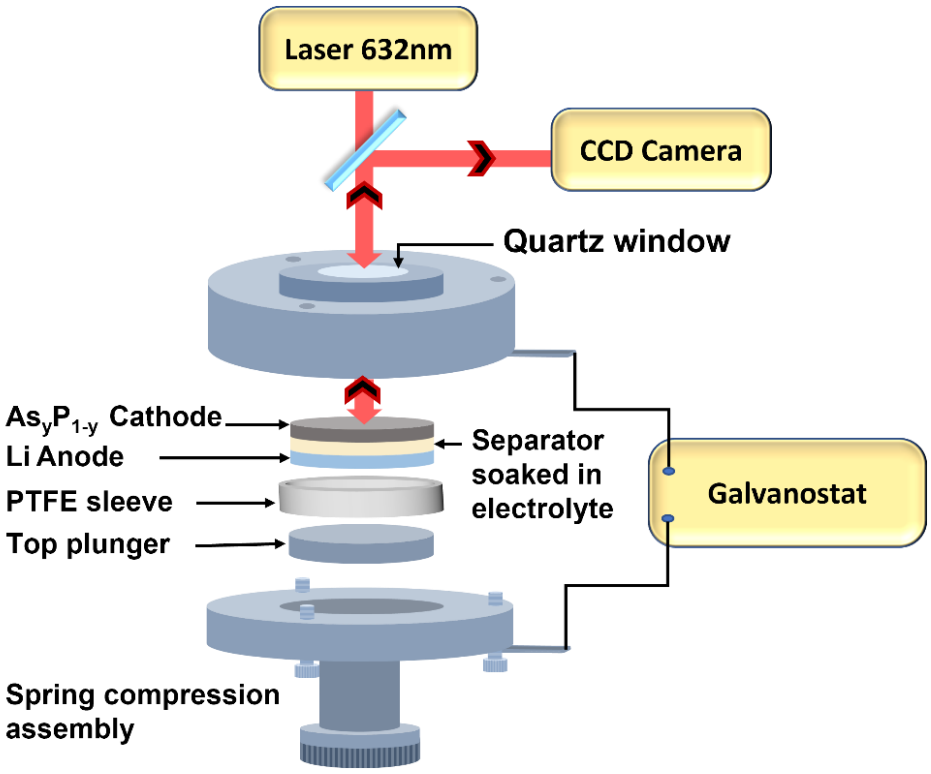

Figure 2.18: Schematic of the in-situ electrochemical intercalation setup

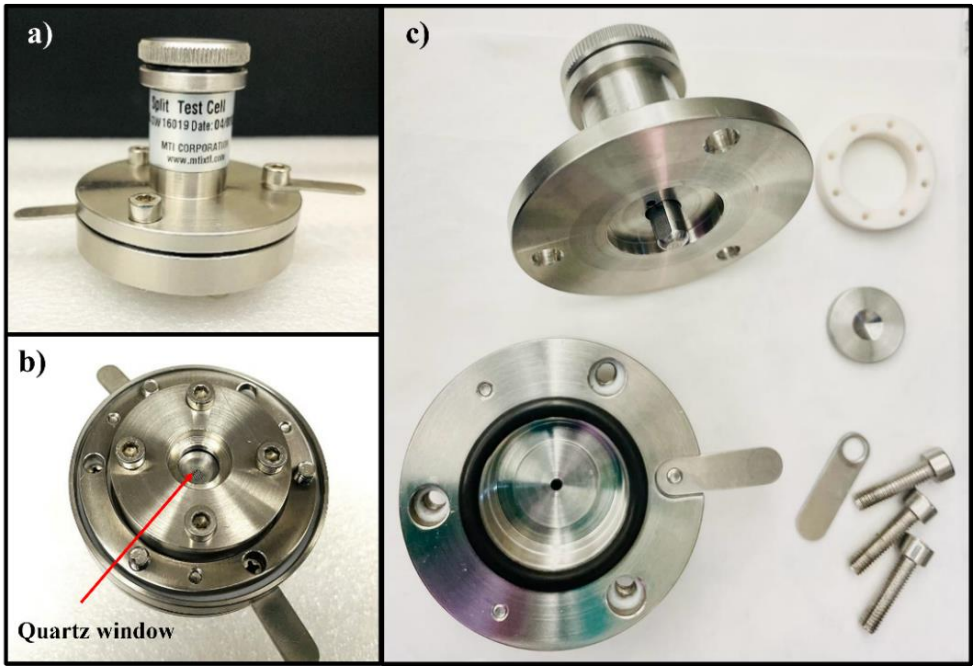

Figure 2.19: Split test cell a) top view b) bottom view c) internal view

Anode:

In an electrochemical cell, the anode is the electrode oxidation occurs, thereby serving as the negative terminal. Throughout the electrochemical reaction, the anode functions as the locus of electron generation and release into the external circuit.

The selection of anode materials for intercalation experiments depends on various factors, including their reversible intercalation capability, capacity, redox potential, and structural compatibility with the host material. Among these considerations, Li is the best-known anode material for battery applications. This recognition arises from the fact that Li's exceptional ability for reversible intercalation, wherein it can be inserted into and extracted from host materials without significant structural degradation. Furthermore, Li is lightest and the most electropositive among the alkali metals. Moreover, the low density of Li ($0.534 g/cm^{-3}$) contributes to its high specific capacity value of 3.86Ah/g.

The high intercalation capacity of Li allows for the efficient storage of a considerable number of ions per unit mass or volume. This high-capacity grants significant advantages in energy storage applications, as it enables the effective storage of a substantial amount of charge.

The redox potential of Li (-3.01V) proves to be complementary for the desired electrochemical reactions in intercalation systems. The redox potential determines the voltage and energy characteristics of the electrochemical cell. Notably, Li exhibits structural compatibility with numerous two-dimensional (2D) materials, such as graphite and transition metal oxides sulfides, without causing significant structural distortions or

irreversible changes. However, the effects of Li intercalation in b-As_yP_{1-y} alloys remain unreported, as of now.

Cathode:

In an electrochemical cell, the cathode serves as the electrode where reduction reactions take place (acting as the positive terminal), and where guest species undergo intercalation during the discharge cycle. It functions by accepting electrons from the external circuit, facilitating the storage of electrical energy through reversible intercalation processes. Upon charging the intercalation cell, the guest species are subsequently deintercalated from the cathode material.

This intercalation reaction is primarily favored by the host structure's low dimensionality, particularly in layered structures, which allows for the facile storage of charge-carrying ions between the layers. Additionally, the cathode should exhibit good electrical conductivity to enable effective charge exchange. To enhance conductivity, a conductive substance, such as b-As_yP_{1-y}, is mixed with a binder.

In this study, a mixture of polytetrafluoroethylene (PTFE) and acetylene black is used as the binder material for the cathode. These binder materials effectively bind the cathode material together as a cohesive pellet, contributing to enhanced conductivity (figure 2.20).

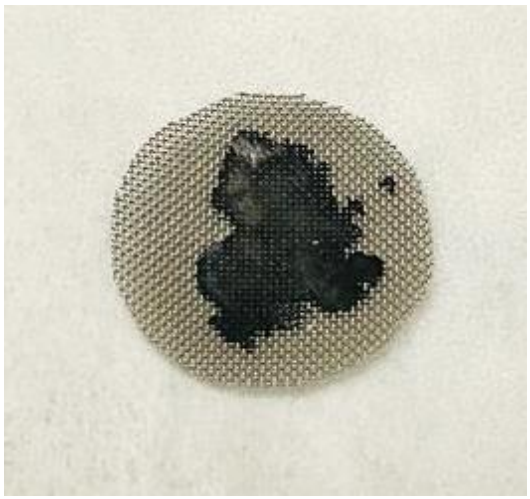

Figure 2.20: As_yP_{1-y} cathode

Electrolyte:

The electrolyte serves as a medium (whether in liquid or solid form), that facilitates the transport of ions between the cathode and anode within a cell. It is worth noting that electrolytes exhibit excellent ionic conductivity, making them effective conductors of ions. Typically, an electrolyte consists of a salt composed of the anode element, which is a common and suitable choice for this purpose. In this work, Li is utilized as the anode material, a 1 M solution of lithium hexafluorophosphate ($LiPF_6$) serves as the primary component of the electrolyte. This solution is combined with ethylene carbonate and dimethyl carbonate in a 1:1 ratio, enhancing its properties and characteristics.

Separator:

The separator used is a polymeric membrane placed between the anode and cathode (figure 2.21). Its primary purpose revolves around preventing short circuits between the anode and cathode, achieved through effective electrical insulation. Simultaneously, it permits the necessary passage of ions required for the electrochemical reactions to occur.

It effectively inhibits electron flow between the electrodes, indicating its excellent electrical insulation properties. Furthermore, this membrane serves as a permeable microporous layer, soaked by the electrolyte, to facilitate the smooth movement of ions from one electrode to the other. The separator also has a high ionic conductivity to enable the efficient transport of ions. Moreover, it exhibits chemical and electrochemical stability to withstand the harsh conditions within the cell.

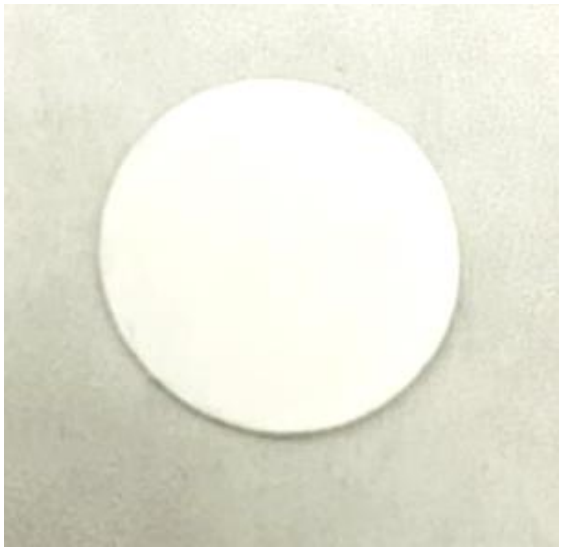

Figure 2.21: Separator

Current collector:

In order to enhance the conductivity of the cell, both the anode and cathode materials are affixed to current collectors. These collectors play a crucial role as connecting components by gathering the electrical current generated at the electrodes and establishing a connection with external loads. Commercially available current collectors typically consist of aluminum (Al) and copper (Cu) foils, which are widely utilized for this purpose.

However, in this work, circular stainless steel meshes serve as the current collectors (shown in figure 2.22). This stainless steel meshes are tightly bonded to the Li metal (anode) and mixture of b-As_yP_{1-y} and binder (cathode) through the application of hydraulic pressing. This ensures a secure attachment and establishes a reliable electrical pathway within the cell.

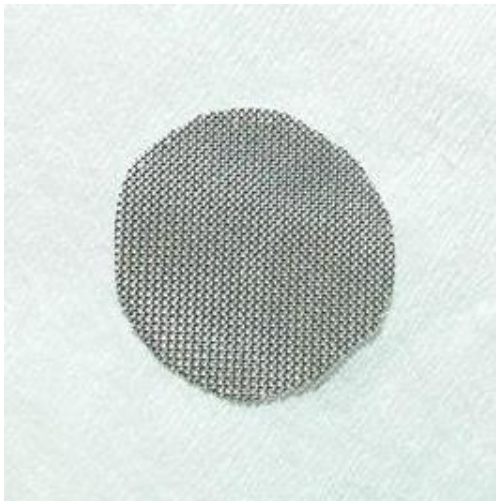

Figure 2.22: Current collector (Stainless steel mesh)

Subsequently, the split test cell was employed to assemble the electrochemical cell. The assembly process involved sandwiching the separator, which had been soaked in liquid electrolyte, between the Li anode and b-As_yP_{1-y} cathode, both firmly attached to the current collector. It is important to note that the entire cell assembly procedure was conducted within a glovebox environment to avoid any potential moisture and oxygen exposure.

The intercalation process was performed by discharging the assembled cell by applying a constant discharge current. (chronopotentiometry).

Chronopotentiometry

Chronopotentiometry is an electrochemical technique used to study the relationship between the applied current and the resulting potential or voltage response of an electrochemical cell. In chronopotentiometry, a known constant current is applied to the cell, typically using a potentiostat/galvanostat instrument. This method is also known as Galvanostatic discharge as the cell is being discharged under the constraint of a constant current across the external load. The potential or voltage response of the cell is continuously recorded or measured as a function of time. This technique allows for the investigation of various electrochemical processes, including charge transfer kinetics, electrode reactions, ion diffusion, and mass transport phenomena.

Figure 2.23: Metrohm Autolab PGSTAT302N potentiostat/galvanostat unit

The assembled cell was discharged by applying -0.2mA discharge current using the Metrohm Autolab PGSTAT302N potentiostat/galvanostat unit (figure 2.23). The Nova 2.1 Autolab controller software facilitates both the pre-programming of the galvanostat and the recording of measurements. The voltage-time profile is utilized to investigate the electrochemical process accurately.

The total cell discharge process was conducted while simultaneously acquiring real-time Raman spectra. The degree of lithiation, denoted as x, was calculated using the following electrochemical formula:

$$x = \frac{MIt}{emN_A}$$

Where M, I, e, N_A, and m represent the molar mass of b-As_yP_{1-y}, discharge current, elementary charge, Avogadro's number, and mass of b-As_yP_{1-y} (active mass), respectively. Since all these parameters are constants for a specific cell, and assuming a constant discharge current (galvanostatic), the degree of lithiation (x) exhibits a linear relationship with the discharge time (t).

2.4. High -pressure technique

The samples are subjected to high-pressure using Diamond Anvil Cell (DAC).

2.4.1 Diamond Anvil Cell

A Diamond Anvil Cell (DAC) is a device commonly employed in high-pressure experiments to generate extreme pressures on small samples. It comprises two opposing diamond anvils with small flat surfaces. When a sample is inserted between the diamond culets and the DAC compresses, the sample experiences exceedingly high-pressure levels. This setup allows to achieve high-pressures surpassing 100 gigapascals (GPa) with relative ease[87]. The initial development of an anvil device for high-pressure investigations involved the use of tungsten carbide (WC) by American physicist Percy Williams Bridgeman.

Subsequently, the utilization of diamonds as anvil materials was first documented in 1958 at the National Bureau of Standards by Charles E. Weir, Ellis R. Lippincott, and Elmer N. Bunting[88].

The diamond culets of a Diamond Anvil Cell (DAC) possess a relatively small surface area (A), typically ranging from 100 to 900 microns. Consequently, the application of a small force (F) on the DAC leads to the generation of high pressures at the diamond culets (P), following the fundamental relationship P=F/A. In terms of mineral hardness as defined by the Mohs scale, single crystal diamond stands as the hardest known material, possessing an absolute hardness value of 1500 and a relative hardness of 10. This exceptional hardness enables diamonds to withstand extremely high pressures.

The transparency of diamonds also serves as an advantage, as it allows electromagnetic radiation to pass through. This property facilitates the collection of in-situ spectroscopic data. Furthermore, the transparency of diamonds permits sample observation and enables mounting under an optical microscope.

Two diamond culets that are affixed to the backing plates of the cylinder and the piston of the DAC. A pre-indented gasket consisting of a drilled hole at the center is utilized to create a sample chamber between the diamonds. This chamber serves the purpose of housing the sample and accommodating the pressure medium, typically a liquid or a gas. The pressure medium is introduced to ensure uniform pressure distribution in all directions.

To pressurize the sample, it is placed within the sample chamber immersed in the pressure medium. The top piston, equipped with a diamond culet, exerts downward force on the sample chamber. This force can be applied using methods such as a gas membrane

or a screw-driven mechanism. As the top piston descends into the cylinder, which also possesses a diamond culet, the sample within the pressure medium experiences an increase in pressure. The schematic of the experimental setup is shown in figure 2.24.

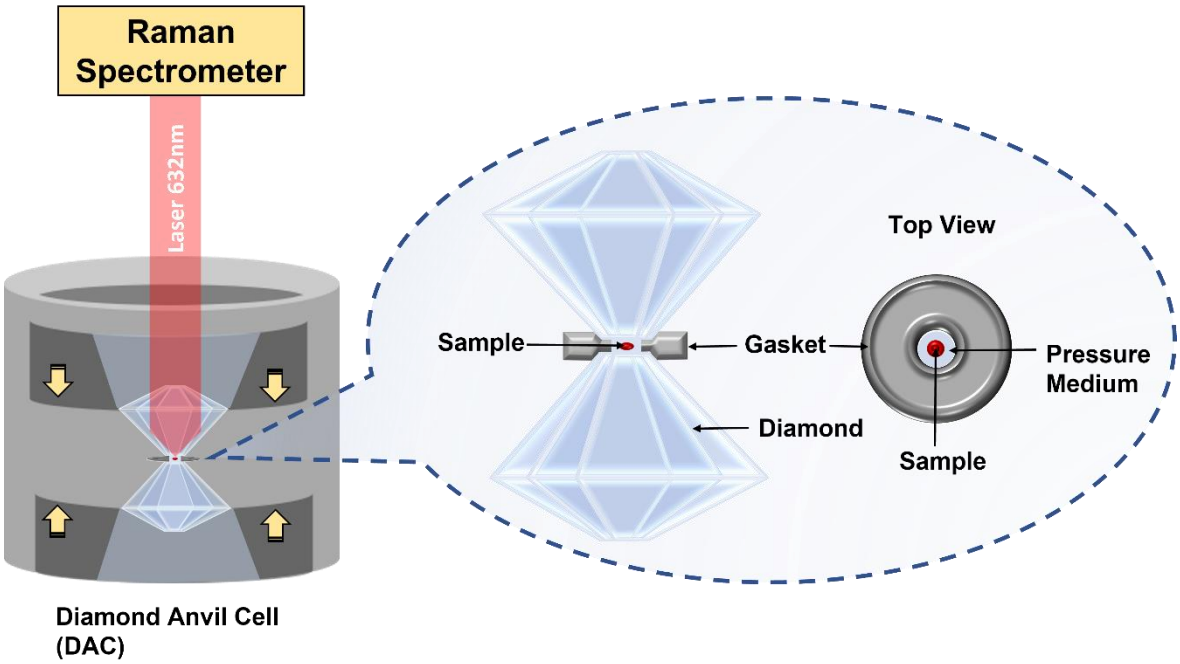

Figure 2.24: Schematic of the diamond anvil cell and the experimental setup for in-situ Raman spectroscopy.

Pressure is determined within the DAC by incorporating ruby powder alongside the sample. Ruby exhibits a photoluminescence spectrum that is dependent on pressure, enabling the calibration of pressure levels within the DAC. More information regarding this technique can be found in the subsequent section.

The DAC used in this study is the Diacell Helios DAC, driven by a gas membrane and manufactured by Almax Easy-Lab Inc. in Belgium. The diamonds employed in this DAC possess a culet size of 800 µm in diameter. Additionally, this DAC model is equipped with a resistive heater, enabling the execution of high-temperature experiments when

necessary. Figure 2.25 represents the a) cylinder and the b) piston of the DAC. The steps to assemble DAC are indicated in figure 2.26. Figure 2.27 illustrates the cross-section view of the DAC.

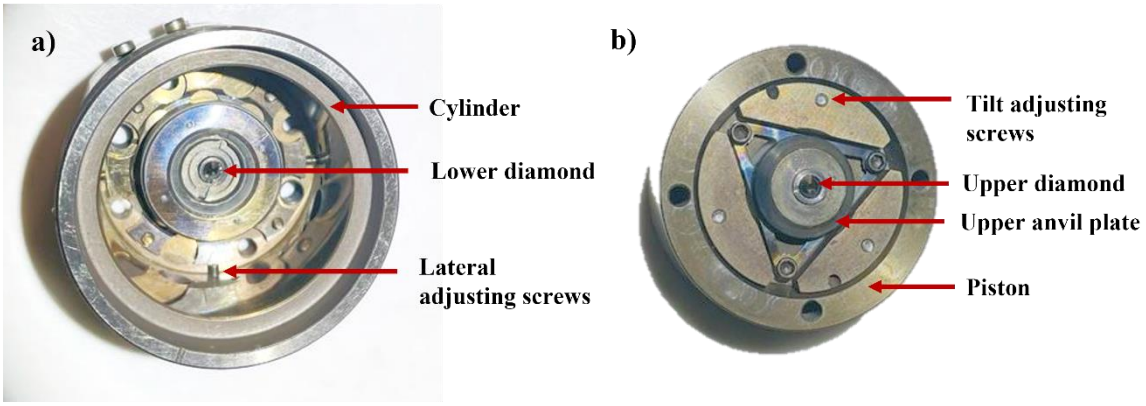

Figure 2.25: Top view of a) cylinder and b) piston of the DAC

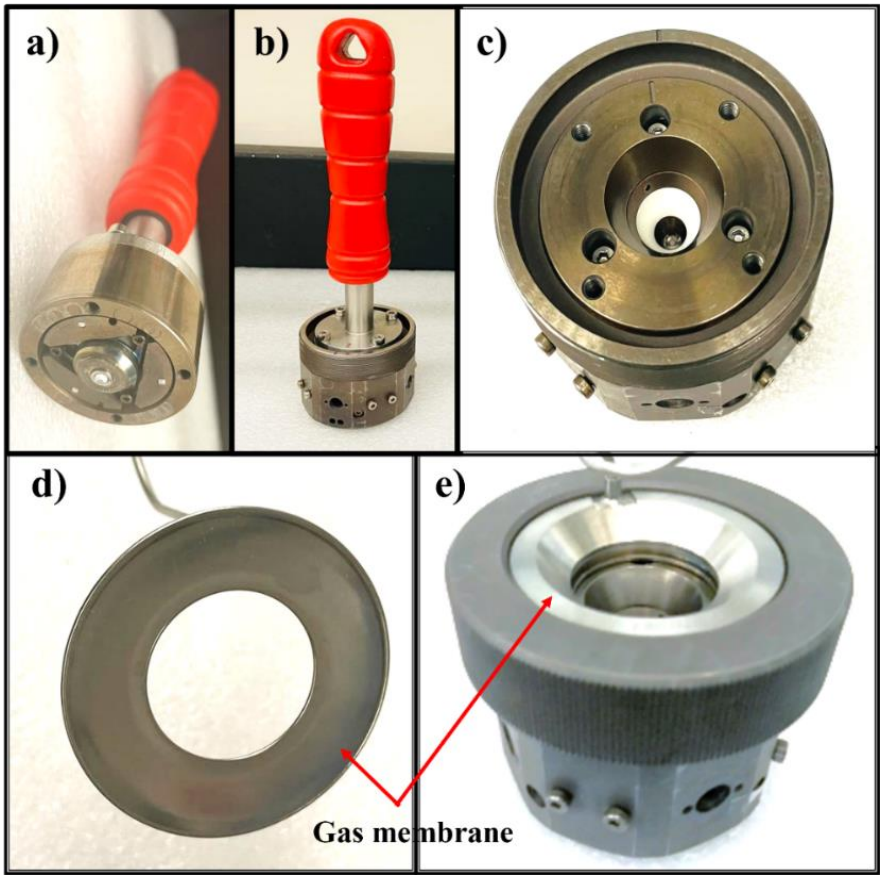

Figure 2.26: a) Piston attached to extractor b) Piston inserting into the cylinder c) Assembled piston and the cylinder d) Gas membrane e) Fully assembled DAC (Including gas membrane and the supporting ring)

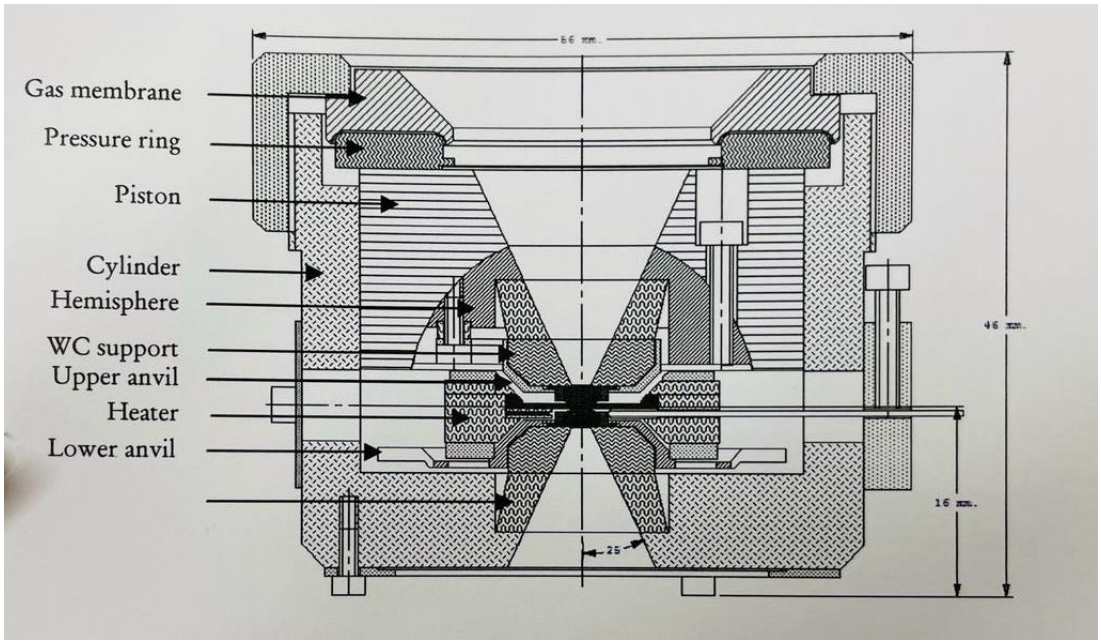

Figure 2.27: Cross section view of the Diacell Helios DAC

Choice of diamonds

The selection of appropriate diamonds for a DAC is of utmost importance due to the extreme strain they experience during high-pressure experiments. In the context of selecting diamonds for a DAC, the quality criteria are determined by "The 4Cs of diamonds." This methodology, developed by the diamond industry, evaluates the grade of diamonds based on four factors: Carat, Clarity, Color, and Cut[89]. Carat (ct) is the unit of measurement for the mass of gemstones, where 1 ct is equivalent to 200 mg.

The clarity of a diamond refers to the presence of impurities, both on its surface and within its interior. Assessing the clarity involves examining the diamond under an optical microscope at 10x magnification. Diamonds that exhibit no flaws under this magnification, such as Flawless (FL) and internally flawless (IF) diamonds, are considered the most expensive. These flawless stones are particularly perfect choice for spectroscopic

measurements. It is crucial to avoid impurities in the diamond, as they can lead to cracks in the anvils when subjected to high pressure. Additionally, impurities or defects can cause deviations in the optical path of beams or introduce unwanted peaks in spectroscopic measurements.

The color of a diamond is determined using the Gemological Institute of America (GIA) scale. This scale ranges from D, representing complete colorlessness, to Z, indicating a pale yellow or brown hue. Fluorescence from a diamond can elevate the background level and potentially overshadow the signal from the sample. For Raman experiments, diamonds with low fluorescence (Type IA) are preferred.

The "cut" of a diamond relates to the quality of its proportions and the positioning of its surfaces. When using DAC in experiments, the size of the culet plays a crucial role in determining the maximum achievable pressure. This is because the pressure magnification is defined by the ratio between the table and culet dimensions. The cut of diamonds also governs the accessible range in spectroscopic instruments (such as accessible 2θ range in XRD).

The Belgian company, Almax easyLab Inc., manufactures various diamond cuts and designs tailored for diverse high-pressure applications. Figure 2.28 illustrates the range of available options. In the present study, the Diacell Helios DAC model contains two 16-sided diamonds with a diameter of 3.10 mm and a culet size of 0.80 mm (Figure 2.29). These particular diamonds proved advantageous for in-situ Raman experiments due to their exceptionally low fluorescence characteristics.

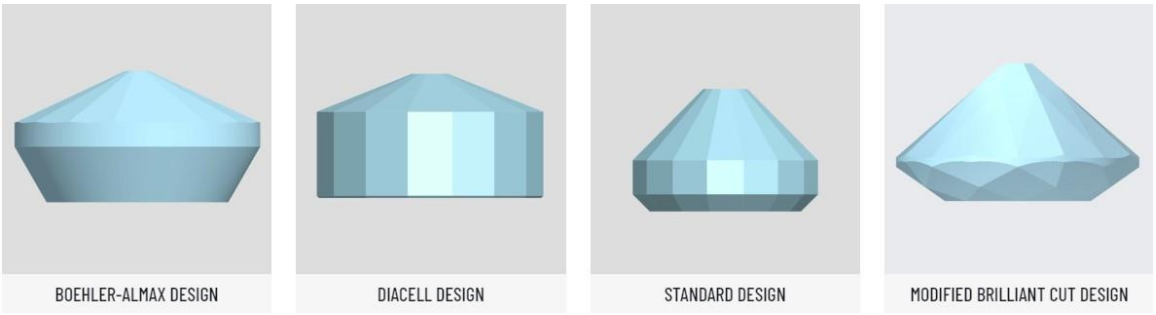

Figure 2.28: Diamond cuts and designs for different high-pressure applications. (Courtesy of Almax EasyLab Inc.)

In DACs, diamonds are supported by two backing plates, also referred to as anvil seats. These backing plates are typically composed of hard materials such as tungsten carbide (WC) and serve to secure the diamonds in place. Prior to attachment, thorough cleaning of both the diamond and backing plate surfaces is essential to eliminate any dust particles that may introduce pressure asymmetry, potentially leading to cracks. Depending on the specific DAC application, diamonds can be either glued or force-fitted onto the backing plates.

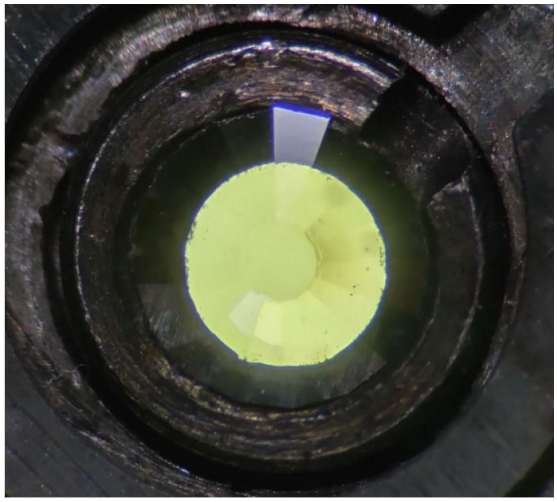

Figure 2.29: Diamonds used in Diacel Helios DAC (Diacel-cut, 16-sided)

Alignment of diamonds

Prior to conducting any experiment, it is crucial to ensure the proper alignment of the two diamond anvils. Misalignment can result in errors during pressure application and calibration and may even lead to diamond damage under high-pressure conditions. Therefore, meticulous alignment is essential to ensure that the culet surfaces of the two diamonds are parallel to each other. The culet surfaces must coincide and establish perfect contact during pressure application. Alignment procedures should be carried out under an optical microscope with utmost care and attention to detail. It is imperative to thoroughly examine the lateral directions of the diamonds under the microscope to verify accurate alignment.

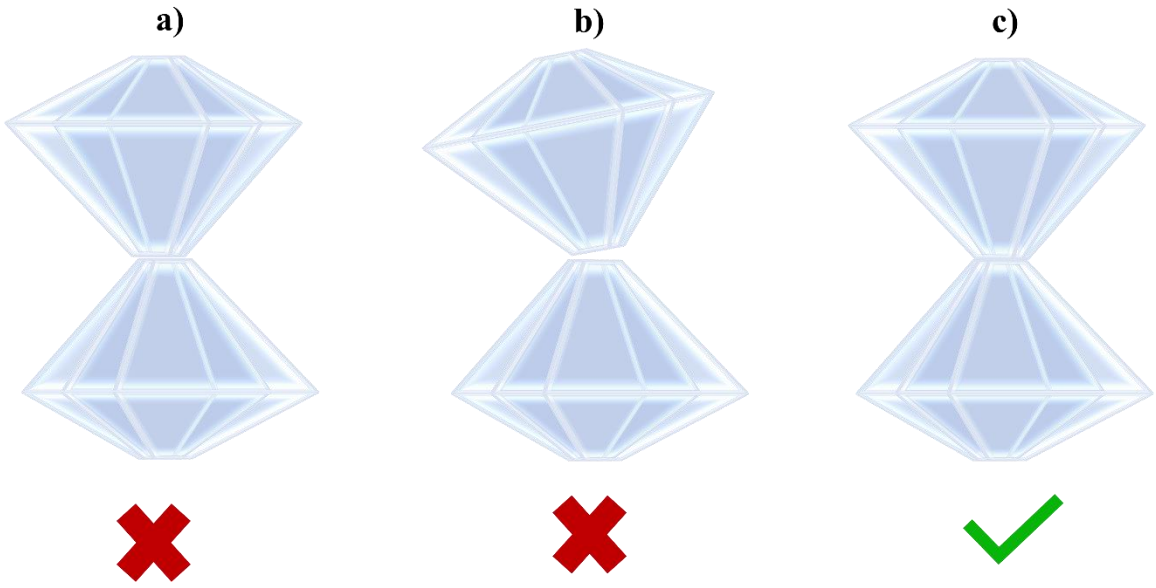

Figure 2.30: Schematics for possible diamond misalignments: (a). Lateral misalignment, (b). Tilt misalignment and (c). properly aligned diamonds.

Lateral misalignment and tilt misalignment are illustrated schematically in Figures 2.30 (a) and (b) respectively. Tilt misalignment, depicted in Figure 2.30 (b), results in the formation of Newton's Rings, which can be observed through the microscope. These Newton's Rings arise due to the presence of a minute air wedge between the two diamonds. Proper alignment of the diamonds should exhibit the appearance depicted in Figure 2.30 (c) from all lateral directions.

2.4.2. Gasket preparation

A gasket, typically made of a thin and deformable material such as metal, is employed to secure the sample between the diamond anvils in a Diamond Anvil Cell (DAC). The gasket serves a critical function as a sample chamber, effectively containing the sample together with the pressure medium and preventing any leakage. The choice of gasket material is paramount and should consider various factors, including the nature of the sample, the desired pressure range, compatibility with the pressure-transmitting medium, and any specific experimental requirements such as temperature or resistance.

The selection of a suitable gasket material entails finding a material capable of withstanding the desired pressure range without deformation or failure, while also being chemically compatible with both the sample and the pressure medium. In this study, Inconel gaskets with a diameter of 10 mm and a thickness of 0.2 mm were used (figure 2.31). Inconel refers to a trademarked family of nickel-chromium-based superalloys. Notably, Inconel possesses remarkable resistance to oxidation and corrosion, enabling it to withstand extreme pressures and high temperatures.

To prepare the gasket for use, it is necessary to subject it to indentation between the diamond anvils within the DAC while applying a certain level of pressure. The extent of indentation should be determined based on the desired pressure range to be achieved. This process results in the gasket bearing imprints of the diamond shapes. As a customary practice, the gasket is indented to ensure that the thickness of the imprinted central region becomes approximately one-third of the initial gasket thickness (figure 2.32).

Figure 2.31: Inconel gaskets

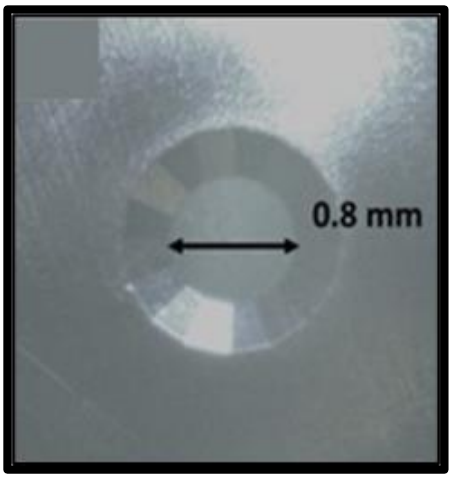

Figure 2.32: Indented gasket

Prior to indentation, it is crucial to thoroughly clean the gasket. Excessive pressure on insufficiently cleaned gaskets may lead to potential diamond fracture or damage. Hence, proper cleaning procedures should be followed to maintain the integrity of the diamonds.

Subsequently, a sample chamber is created by drilling a small circular hole, typically ranging from 0.1 to 0.3 mm in diameter, at the center of the indented portion. This micro-drilling process is carried out using a specialized apparatus known as an Electric Discharge Machine (EDM). The EDM facilitates precise drilling of the desired hole size and location, ensuring the formation of a well-defined sample chamber within the gasket.

Electrical Discharge Machining (EDM), also known as spark erosion or spark machining, employs electric discharges to eliminate material from the workpiece. In this process, the drilling tool, acting as the electrode, and the workpiece (in this case, the gasket), also serving as an electrode, are immersed in a dielectric fluid. An electric voltage is applied between the tool and the workpiece, resulting in a succession of rapid electrical sparks within the small gap separating them. These sparks generate intense heat, causing the workpiece material to melt and vaporize, thereby eroding and eliminating material from the workpiece.

The precise alignment of the tool with the workpiece is accomplished by assisting a low-power microscope (Unitron ZSB 823986 optical microscope). For this work, the Hylozoic Products micro EDM unit is utilized, equipped with an electronics unit for tool control, a tool-setting limit, and a machining unit for regulating the peak power and discharge energy (figure 2.33 (a)). By accurately controlling the parameters of the electrical discharge, it is possible to manage the material removal rate as well as the shape and size of the hole. Prior to drilling, the appropriate settings must be predetermined based on the

desired dimensions of the hole to be created. Magnified view of the gasket after drilling is shown in figure 2.33(c).

Table 2.1: Parameters settings for EDM

Hole Diameter (mm)	Discharge Energy (µJ)	Peak power (W)
0.03 – 0.15	0.05 – 0.2	0.02 – 0.
0.15 – 0.4	0.2 – 0.5	0.1 – 0.4
0.4 – 1.5	0.5 – 20	0.2 - 0.8

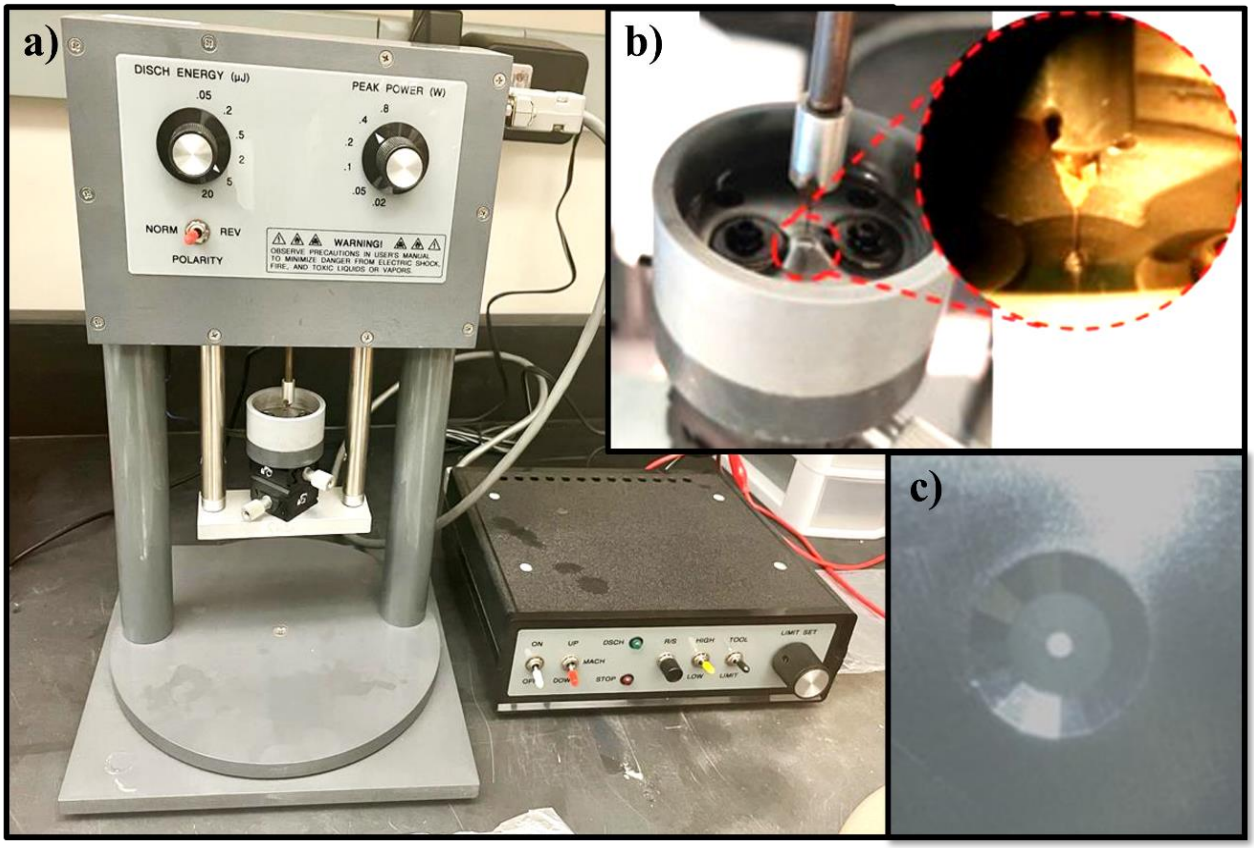

Figure 2.33: a) EDM unit b) Magnified view of drilling action c) Drilled gasket

Sample mounting

Once the gasket has been indented and drilled, it is prepared for sample mounting. The sample is carefully positioned at the center of the drilled gasket, which is submerged in a pressure-transmitting medium (PTM). It is essential to ensure that the sample does not come into direct contact with the gasket, as this would hinder the uniform distribution of pressure through hydrostatic pressure. Ideally, the sample should experience equal pressure in all directions.

To facilitate sample mounting, the sample needs to be crushed into smaller sizes to fit within the circular hole of the gasket, typically with a diameter of 0.2mm. The mounting of the sample is performed using micron-scale needle tips under the observation of a microscope. Once the sample is in place within the gasket hole, the sample chamber is filled with the PTM. This can be accomplished using a micro pipette to ensure precise and controlled filling of the chamber.

The choice of a pressure medium holds significant importance in high-pressure experiments. Selection criteria for a pressure medium should consider the desired pressure range, sample properties, and specific experimental requirements. In general, a liquid pressure transmitting medium (PTM) should possess characteristics such as softness, low compressibility, and chemical inertness to ensure minimal interaction with the sample of interest. Additionally, it is crucial for the PTM to have a high hydrostatic limit in order to prevent any undesired phase transitions resulting from the applied pressure.

While pressure transmitting mediums can be found in gas, liquid, and solid phases for high-pressure experiments, liquid PTMs are often favored over their gas and solid

counterparts due to their ease of loading and handling. In the scope of this study, dimethylformamide (DMF) was employed as the liquid PTM for high-pressure experiments. DMF is a colorless liquid known for its low evaporation rate, in addition to possessing the desired softness, low compressibility, and chemical inertness previously mentioned. Furthermore, the absence of additional Raman peaks within the range of interest (150-500 cm^{-1}) supports DMF as a favorable choice for this study.

The subsequent step involves the cautious insertion of the piston, equipped with the diamond culet, into the cylinder containing the gasket and the sample. It is vital to ensure that the sample remains undisturbed during this process, and any introduction of air bubbles within the pressure transmitting medium (PTM) is avoided. Microscopic view of a properly mounted sample is shown in figure 2.34.

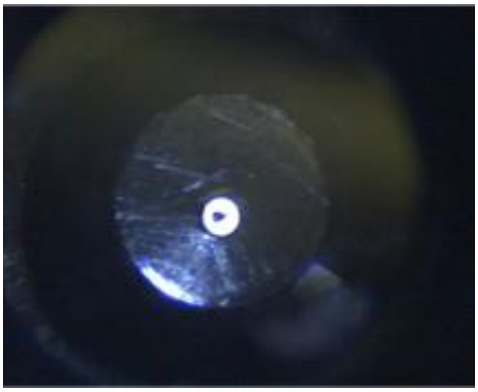

Figure 2.34: The mounted sample as seen under the microscope.

2.4.3 Pressure calibration

After the sample has been mounted, the pressure is generated by the downward movement of the piston in the DAC, facilitated by a gas membrane. This gas membrane, constructed from stainless steel, possesses the ability to expand when filled with gas. Positioned atop the piston, it exerts a downward force as it expands, thereby exerting pressure on the diamonds. The GM controller unit is responsible for regulating the air pressure supplied to the gas membrane from an external source of gas. In this work, a nitrogen gas tank including pressurized gas (3500 psi) was utilized. The GM controller unit comprises a shut-off valve and a release valve to govern the gas flow, while a digital display indicates the pressure (in bar) within the gas membrane (figure 2.35). It is important to note that although the pressure inside the DAC cannot be directly measured.

Figure 2.35: GM controller unit

The Ruby Pressure

The utilization of Ruby's photoluminescence (PL) spectrum for pressure calibration in high-pressure experiments is a well-established technique. This is attributed to the distinctive peak shifts observed in the range of 690-700 nm, known as the Ruby R1 and R2 lines. These peaks exhibit significant variations in their positions with applied pressure, providing a reliable means for precise pressure determination. Notably, the Ruby R2 line shifts are particularly favored for pressure calibration due to their dependence solely on density compression. They remain unaffected by nonhydrostatic stresses and crystal orientation, ensuring more accurate pressure measurements. In contrast, the R1 line shifts are influenced by nonhydrostatic environments and may introduce errors into the calibration process[90]. Therefore, the preference for utilizing the Ruby R2 line as a pressure calibration reference arises from its inherent insensitivity to nonhydrostatic factors, enhancing the reliability and accuracy of high-pressure measurements.

The method involves placing a small ruby chip or microcrystalline powder inside the sample being studied under high pressure. As pressure is applied, the spectral lines of the ruby material shift to higher wavenumbers [90-93]. By measuring the shift in the fluorescence emission wavelength of the ruby, the applied pressure on the sample can be calibrated. The relationship between the wavelength shift and gas pressure is known, allowing for easy calculation of the internal pressure (P) within the DAC using following equations[93, 94].

$$P = 1870\frac{\Delta\lambda}{\lambda_0}\ (1 + 5.9\frac{\Delta\lambda}{\lambda_0})$$

$$\frac{\Delta\lambda}{\lambda_0} = \frac{\lambda - \lambda_0}{\lambda_0}$$

Where λ_o and λ represent the wavelengths of the Ruby R2 line at ambient pressure and the desired pressure P, respectively. By establishing a correlation between the pressure-induced shift in the ruby R2 line and the known gas pressures (obtained from the GM controller, in bar), a calibration curve can be generated (shown in figure 2.36). Subsequently, employing the aforementioned equation in conjunction with the calibration curve, it becomes possible to determine the pressure inside the DAC in gigapascals (GPa).

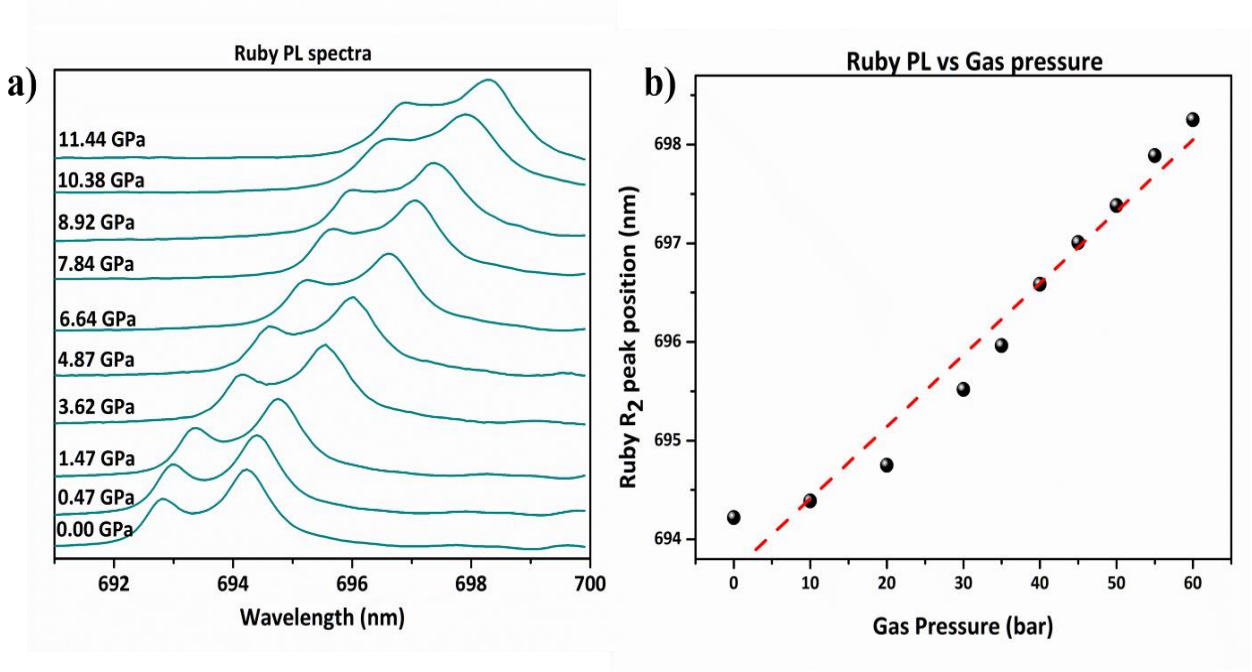

Figure 2.36: Pressure dependence of Ruby PL spectra

Figure 2.37: Experimental setup for high-pressure experiment

CHAPTER 3
RESULTS AND DISCUSSION

Black arsenic phosphorus (b-As_yP_{1-y}) exhibits analogous characteristics to black phosphorus (BP) with slight modifications, particularly when the concentration of arsenic (As) is below 83%. In the primitive unit cell of b-As_yP_{1-y}, the As atoms undergo a subtle outward displacement due to their larger atomic diameter compared to phosphorus (P)[30, 45]. As a consequence, the unit cell parameter and volume of b-As_yP_{1-y} increase as the concentration of As is elevated. Prior to exploring the response of b-As_yP_{1-y}, to intercalation and high-pressure, it is vital to understand the alterations in its characteristics that occur with varying concentrations.

The synthesized series of b-As_yP_{1-y} alloys include four different compositions: b-$As_{0.4}P_{0.6}$, b-$As_{0.5}P_{0.5}$, b-$As_{0.6}P_{0.4}$, and b-$As_{0.8}P_{0.2}$. In order to verify the quality of the synthesized As_yP_{1-y} alloys, several characterization techniques were employed. Atomic vibrational modes were determined and characterized by means of Raman Spectroscopy measurements using Renishaw inVia spectrometer with 632 nm He−Ne laser. X-ray diffraction (XRD) measurements performed using Bruker Discover 8 were used to verify the crystal structure and evaluate lattice parameters of synthesized materials. The morphology and elemental composition of investigated materials were evaluated using transmission electron microscopy (TEM) and energy dispersive x-ray (EDS)

spectroscopy, respectively. These measurements were carried out using FEI Tecnai F20 transmission electron microscope equipped with EDAX TEAM EDS spectrometer. In addition, g-As (corresponding to y = 1) and BP (corresponding to y = 0) were characterized as reference materials.

3.1. Properties of pristine b-As_yP_{1-y} alloys

3.1.1. Vibrational properties of pristine b-As_yP_{1-y} alloys

Raman spectra obtained for gray As, BP, and different alloys are shown in Figure 3.01(a). Black phosphorus exhibits a total of six Raman active modes, including $B_{1g,}B_{3g}^{1}, B_{3g}^{2}, A_{g}^{1}, B_{2g}$ and A_{g}^{2}.[79-81, 95, 96] However, the modes $B_{1g,}B_{3g}^{1}$ and B_{3g}^{2} are rarely observed experimentally, due to their significantly low intensities[97]. Conversely, the remaining three modes (A_{g}^{1}, B_{2g} and A_{g}^{2}) are prominently observed in experimental studies. These three modes correspond to specific vibrational characteristics of the P-P atoms in directions: out-of-plane, in-plane zig-zag, and in-plane armchair, respectively. It is worth noting that the analogous crystal structure of b-As to b-P allows for the observation of the same Raman active modes in black arsenic as well.

In Raman spectra of pristine As_yP_{1-y} alloys, three major regions of peaks, depending on the atomic mass, are observed, Raman modes associated with P-P bonds, identified as A_{g}^{1}, B_{2g} and A_{g}^{2}, corresponding to out-of-plane, in-plane along zig-zag direction and in-plane along armchair directions, respectively, are seen in the high-frequency region (≈350 – 470 cm^{-1}). Further, Raman modes associated with As-As bonds labelled as A_{g}^{1}, B_{2g} and A_{g}^{2} are seen in the low frequency region of (≈ 200 –270 cm^{-1}). The vibrational modes

corresponding to the P-P and As-As bonds are represented in Figure 3.02. Finally, two vibrational modes associated with As-P bonds are seen in the mid-region (≈ 300 –370 cm^{-1}). As arsenic concentration of the alloy increases, a decrease in peak intensities for P-P vibrational modes were observed, whereas peak intensities corresponding to As-As vibrations were increased. It is reasonable because P-P vibrations become less prominent when more P atoms are replaced by As atoms in the lattice. As-P vibrational modes also show a reasonable behavior with the increasing arsenic concentration with their intensity increasing gradually from zero for BP (y = 0) to the maximum value for b-$As_{0.5}P_{0.5}$ (x = 0.5) and then gradually decreasing again to zero for gray As (y = 1).

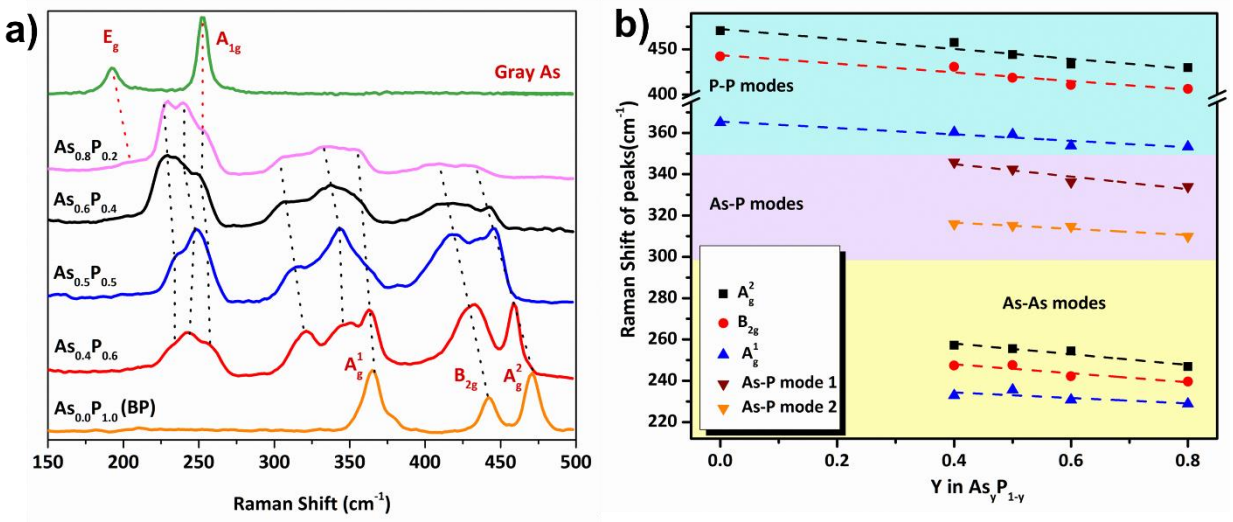

Figure 3.01: (a) Raman spectra for pristine BP, precursor As, and b-As_yP_{1-y} alloys with different chemical compositions. (b) Raman shift vs arsenic concentration (y) for P-P (top), As-P (middle), and As-As (bottom) vibrational modes. Dotted lines provide guide to the eye with linear fits.

It is also observed that peaks of alloy samples are red shifted (w.r.t. BP sample) with increasing arsenic concentration (Figure 3.01(b)). In the context of this study, the terms "red shift" and "blue shift" relate to the frequency. Notably, an interesting observation was made regarding the P-P vibrations in relation to the As concentration. It was found that the modes B_{2g} and A^2_g exhibit larger shifts compared to the A^1_g mode, with factors of 2.2 and 2.4, respectively, as the As concentration increases. This observation is intriguing, particularly considering the similar trends reported in Li-intercalated BP with increasing Li concentration (by a factor of approximately 1.5) [54], as well as in BP under increasing uniaxial strain (by a factor of approximately 1.4)[98].

This finding is in accordance with the increasing amount of arsenic–arsenic bonds and the decreasing contribution of phosphorous–phosphorous bonds, as well as the change in bond strength and bond lengths in the system upon arsenic substitution.

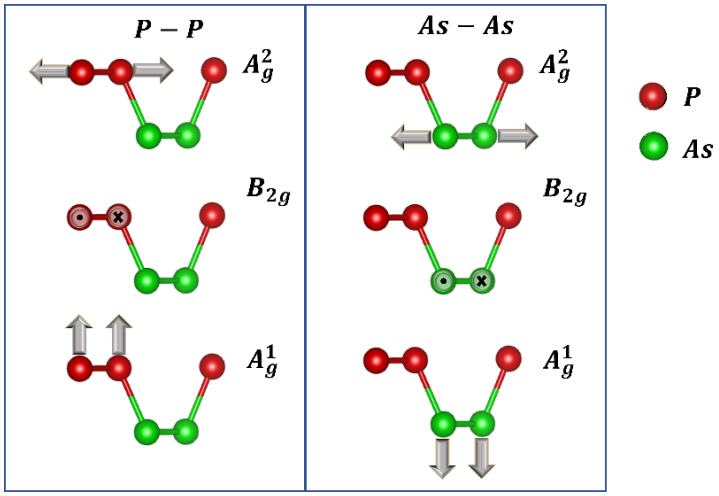

Figure 3.02: The vibrational modes associated with P-P and A-As bonds in b-As_yP_{1-y}

The Raman spectra of precursor As (Figure 3.01 (a)) is rather interesting. It is known that rhombohedral gray As with the A7 structure belongs to the *R3m* space group.

It has three Raman active modes, two-fold degenerate E_g modes and one A_{1g} mode, where the E_g mode corresponds to the in-plane vibrational mode, whereas A_{1g} mode belongs to the out-of-plane vibrational mode[78]. It is further confirmed by our observation of Raman spectrum with two peaks clearly visible at 193cm^{-1} (E_g) and 253cm^{-1} (A_{1g}). It is found that b-As is a metastable phase. Calculated formation energy of b-As is ~0.04 eV/atom higher than that of most stable phase of g-As. Even the combination of b-As with g-As (e.g., 87.5% b-As with 12.5% g-As) is energetically lower than pure b-As (by ~ 5 meV/atom), indicating the possibility of their co-existence. The co-existence of rhombohedral and orthorhombic phases can also be found in the b-As_yP_{1-y} alloys with high As concentration (see the shoulder around 200 cm^{-1} in Figure 3.01 (a)) and illustrated in Figure 3.03.

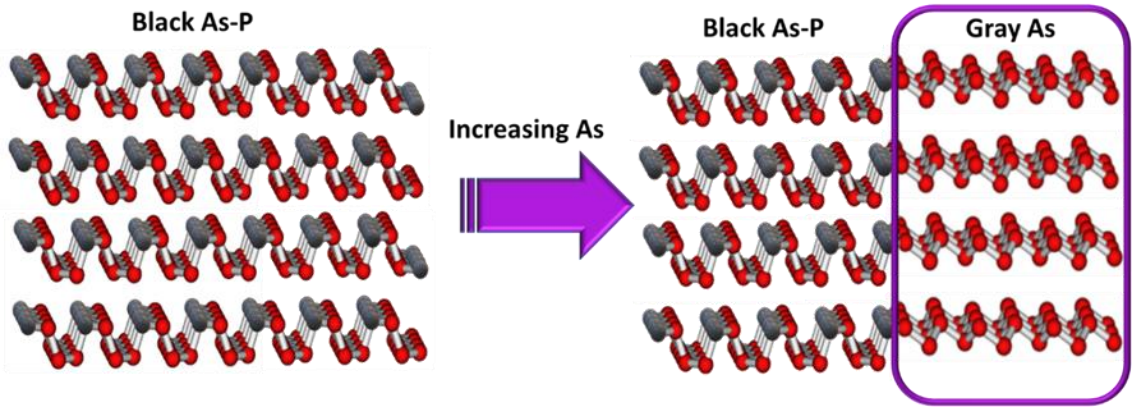

Figure 3.03: A schematic illustrating the segregation of excess As during the synthesis of a high As concentration b-As_yP_{1-y} alloy.

3.1.2. Structural properties of pristine b-As_yP_{1-y} alloys

Next, we characterized each sample using XRD. Figure 3.04(a) shows the XRD pattern of each sample between 10-80^0. The XRD patterns showed the symmetry consistent

with the same type of crystal structure, i.e., orthorhombic puckered structure with the *Cmca* space group, which is characteristic for BP and b-As_yP_{1-y} alloys. For all samples, the strongest observed peaks were of (0*k*0)-type, consistent with flake morphology of the particles in these samples. Additional weak peaks were also observed in some samples, most notably in b-$As_{0.5}P_{0.5}$. However, as shown in Figure 3.04, all peaks originated from the same orthorhombic puckered structure phase. The relative intensity between (0*k*0) and mixed-index peaks depends on the thickness of the flakes; the thicker the flakes the stronger the mixed-index peaks. This can be clearly seen for the XRD pattern of a coarse-grain reference BP sample also shown in Figure 3.04.

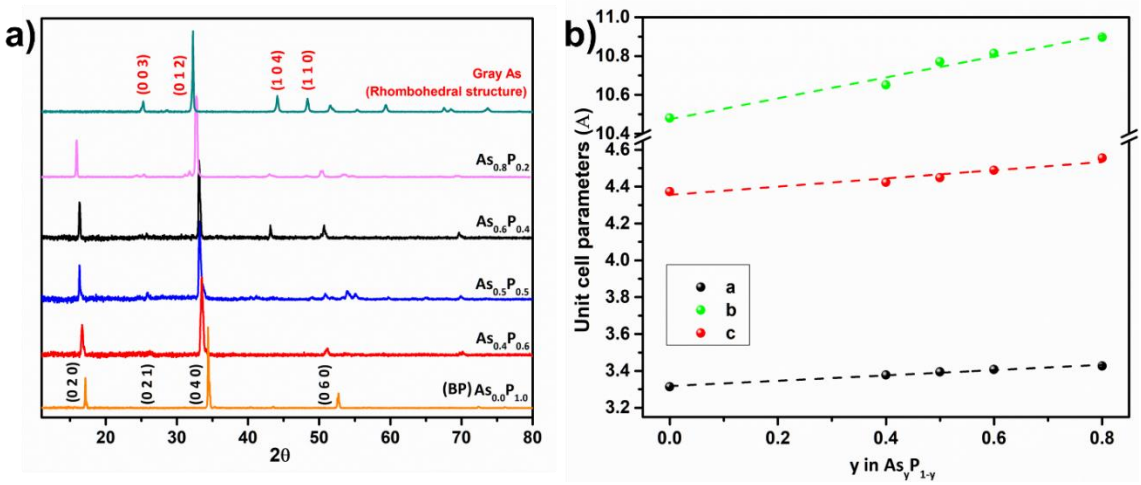

Figure 3.04: (a) XRD patterns for pristine BP, precursor As, and b-As_yP_{1-y} alloys with different chemical compositions. (b) The unit cell (orthorhombic) parameters extracted from the XRD data against the alloy composition y. Dotted lines provide guide to the eye with linear fits.

The XRD measurements showed a systematic expansion of the crystal structure with the increase of arsenic concentration, y. This can be seen in all three lattice constants, *a*, *b* and *c*, extracted from XRD data and summarized in Table 3.1. The observed increment in the c/a ratio suggests, that a higher relative lattice expansion along the c-axis in

comparison to the a-axis as the concentration of arsenic increases. This is consistent with the crystal structure and the preferential deformation direction of the orthorhombic puckered structure.

Gray arsenic exhibits a rhombohedral crystal structure with the R3m space group. Interestingly, several X-ray diffraction (XRD) peak positions closely resemble those observed in the orthorhombic BP structure. Notably, the XRD peaks at approximately 25^0 and 32.5^0 represent (0 0 3) and (0 1 2) crystallographic planes, of the rhombohedral gray arsenic phase, respectively. In contrast, orthorhombic BP exhibits peaks corresponding to the crystallographic planes (0 2 1) and (0 4 0), with closely proximate angles as mentioned above.

Table 3.1: Values of lattice constants, a, b and c, measured from XRD analysis.

Samples	a (Å)	b (Å)	c (Å)	c/a
BP	3.314	10.480	4.373	1.320
b-$As_{0.4}P_{0.6}$	3.347	10.651	4.423	1.321
b-$As_{0.5}P_{0.5}$	3.354	10.771	4.449	1.326
b-$As_{0.6}P_{0.4}$	3.378	10.813	4.488	1.330
b-$As_{0.8}P_{0.2}$	3.416	10.896	4.565	1.336

Lattice parameter identification

b-As_yP_{1-y} exhibits the same crystal structure symmetry as BP. Crystallographic information from the PDF-2 database has been used to fit the BP XRD data initially and the lattice parameters were tuned to fit with b-As_yP_{1-y} alloys. For the b-$As_{0.8}P_{0.2}$ and intercalated samples, Gray As crystallographic information were used in addition to BP to determine lattice parameters.

The Bruker software Diffrac Eva 4.3 was used to evaluate the lattice parameters of the synthesized b-As_yP_{1-y} alloys. XRD patterns were recorded for each composition, and BP crystallographic information file is loaded (PDF 00-047-01626) and subsequently, the "tune cell" option in the Diffrac Eva software was used.

The procedure initiated by focusing on the (0k0) type reflections and performing parameter tuning. Since (0k0) reflections depend only on one parameter, they were utilized to tune “b” parameter without affecting other parameters. Particularly, the strongest reflections, such as (020), (040), and (060), were used to tune the “b” parameter to align with the peak positions. Exact peak positions were determined employing “peak search” tool in Diffrac Eva. Subsequently, the (002), (021), and (022) reflections were employed to tune the “c” parameter, taking into account the potential weakness of the (002) reflection in certain samples. Following this, indices such as (200), (202), (131), (112), and other mixed indices were employed to tune the “a” parameter.

In the $As_{0.8}P_{0.2}$ sample and the intercalated samples, a rhombohedral crystal structure, (similar to gray As and belonging to the R3m space group) emerged. Additional peaks resulting from phase segregation were matched by tunning the lattice parameters of gray As (PDF 01-072-1048). First “c” parameter was tuned matching with (003) and (006) reflections. Then mixed indices including (012) were used to tune “a” parameter. Only the “a” and “c” parameters required to be tuned, since the “a” and “b” parameters are dependent. As an example, intercalated b-$As_{0.6}P_{0.4}$ is shown in figure 3.05.

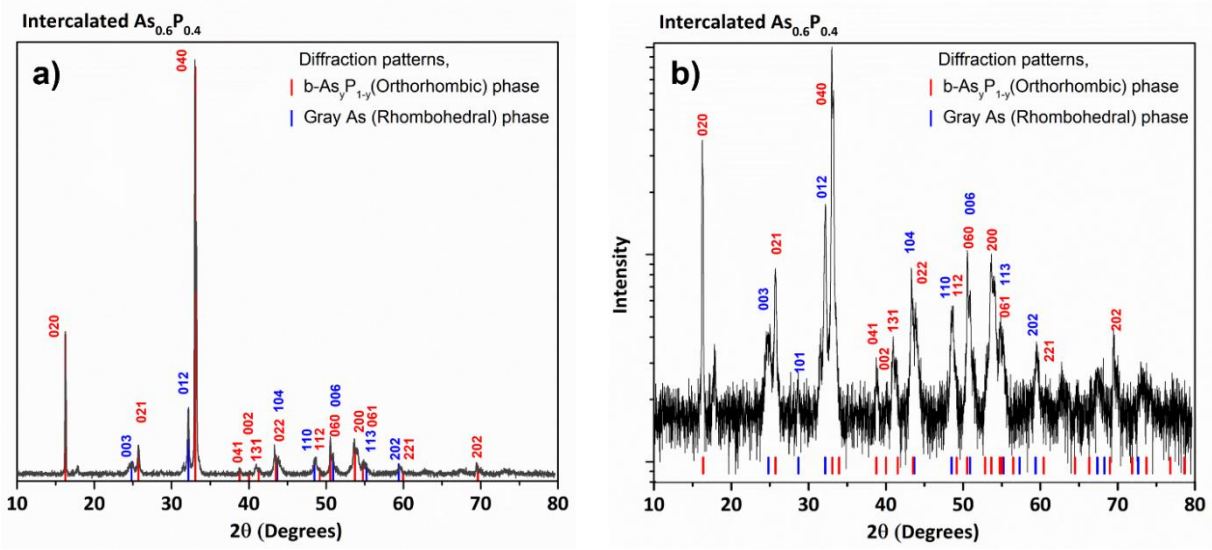

Figure 3.05: (a) The XRD pattern of intercalated $As_{0.6}P_{0.4}$ alloy. (b) Logarithmic scale representation of the XRD pattern. The red and blue stick patterns indicate matched diffraction peak positions, tuning BP and Gray As phases respectively.

3.1.3. Morphology and elemental compositions of pristine b-As_yP_{1-y} alloys

All samples were also characterized using TEM and EDS analysis. and the results are summarized in the following.

As predicted, the TEM imaging, as illustrated in Figure 3.06, confirmed the flake morphology, which is characteristic of layered materials, for both black phosphorus (BP) and the b-As_yP_{1-y} samples. HRTEM analysis of individual flakes revealed the presence of large single-crystalline regions displaying distinct lattice fringes, indicative of the orthorhombic puckered structure. The SAED patterns obtained from these individual flakes predominantly exhibited the characteristics of a single crystalline nature, demonstrating symmetry of the orthorhombic puckered structure with the Cmca space group, which is characteristics for BP. These findings align with our previous research work conducted by Manthila et al., thereby reinforcing the systematic expansion of the crystal structure observed with an increasing concentration of As[33]. The lattice expansion coefficient with

the As concentration, determined to be 0.0645. Notably, the calculated c/a ratio illustrates a greater expansion along the c-axis compared to the a-axis, supporting the crystallographic insights derived from our XRD measurements. Furthermore, the lattice expansion was substantiated by the observed increase in the values of d-spacings for several crystallographic planes, as found through HRTEM and SAED analysis.

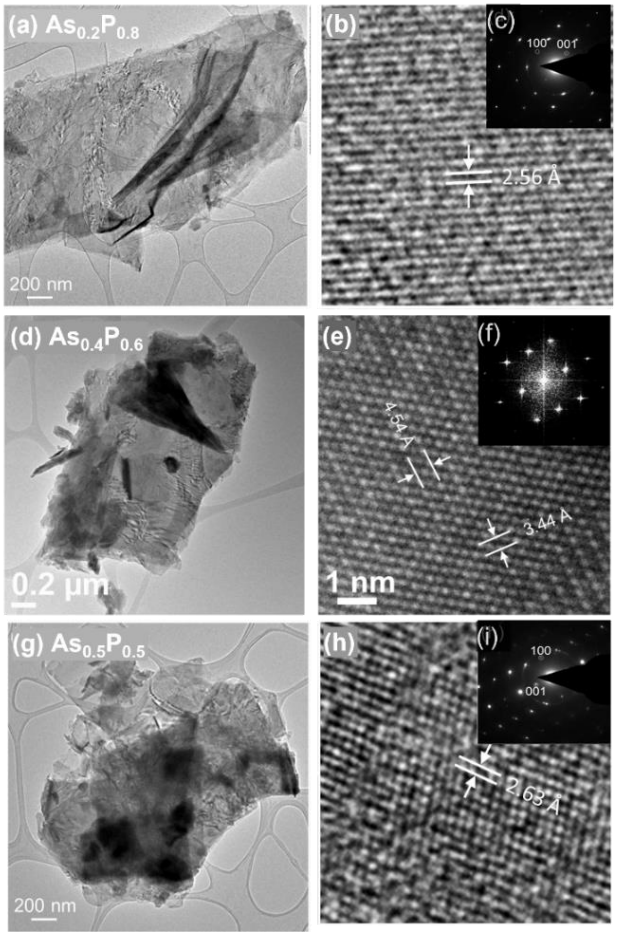

Figure 3.06: TEM characterization of $As_{0.2}P_{0.8}$, $As_{0.4}P_{0.6}$ and $As_{0.5}P_{0.5}$ samples. The left panel (a, d, g) Low-magnification and right panel (b, e, h) HRTEM images of $As_{0.2}P_{0.8}$, $As_{0.4}P_{0.6}$ and $As_{0.5}P_{0.5}$ flakes respectively. The insets of the right panel show the FFT of each HRTEM images.

At a larger scale, the examined alloyed materials exhibited a polycrystalline nature, as evidenced by the HRTEM and SAED analyses. Within the larger grains, distinct domains with varying orientations were observed, along with the presence of extended structural defects, such as dislocations, and structural inhomogeneity, exhibited as heavily distorted atomic planes. These features were frequently observed in HRTEM images. The occurrence of structural defects and lattice distortions was further revealed in the arcing of diffraction spots observed in SAED patterns acquired from larger sample areas. A representative example of such observations is illustrated in Figure 3.07.

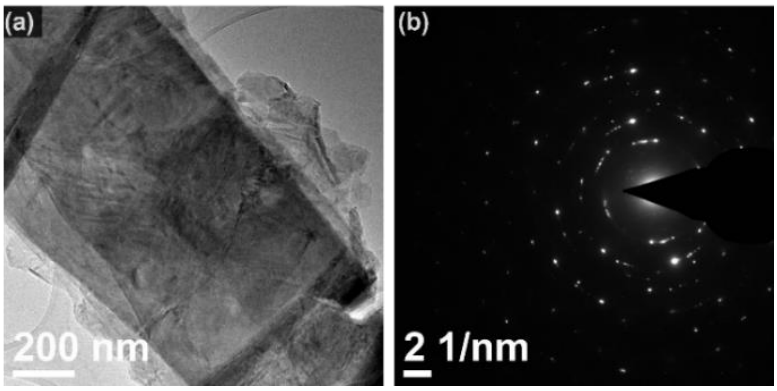

Figure 3.07: TEM and FFT images showing defects in b-$As_{0.4}P_{0.6}$ flake.

Phosphorous and arsenic were found to be homogenously distributed within the b-As_yP_{1-y} samples, as shown by phosphorus (P-K) and arsenic (As-K) EDS mapping (Figure 3.09, left and middle panels). Moreover, the EDS spectra from the investigated samples showed the gradual change of the intensity ratio between As-K and P-K lines with decreasing nominal concertation of arsenic from y = 1 (precursor-As) to y = 0 (BP) (Figure 3.09 right panels).

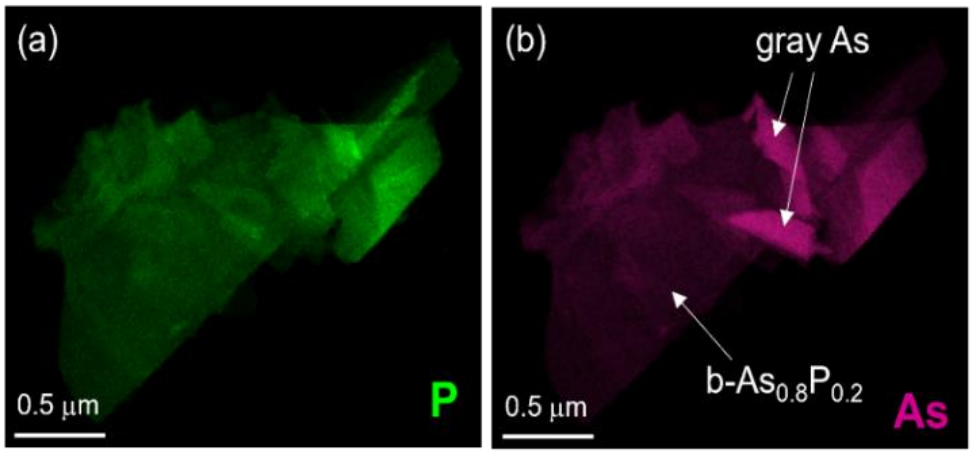

Figure 3.08: (a) P-K and (b) As-K elemental maps of a b-$As_{0.8}P_{0.2}$ flake with two small g-As particles attached to it (shown in b).

However, the sample with highest As concentration (y = 0.8), contain arsenic segregated regions. Increased As concentration cause part of the sample to undergo such structural change. This is also consistent with EDS elemental mapping of this sample where excess of As particles were observed in addition to b-$As_{0.8}P_{0.2}$ flakes (see example EDS mapping in Figure 3.08). However, the samples exhibited a variation in composition distribution within different grains, as evidenced by a standard deviation of approximately 0.05.

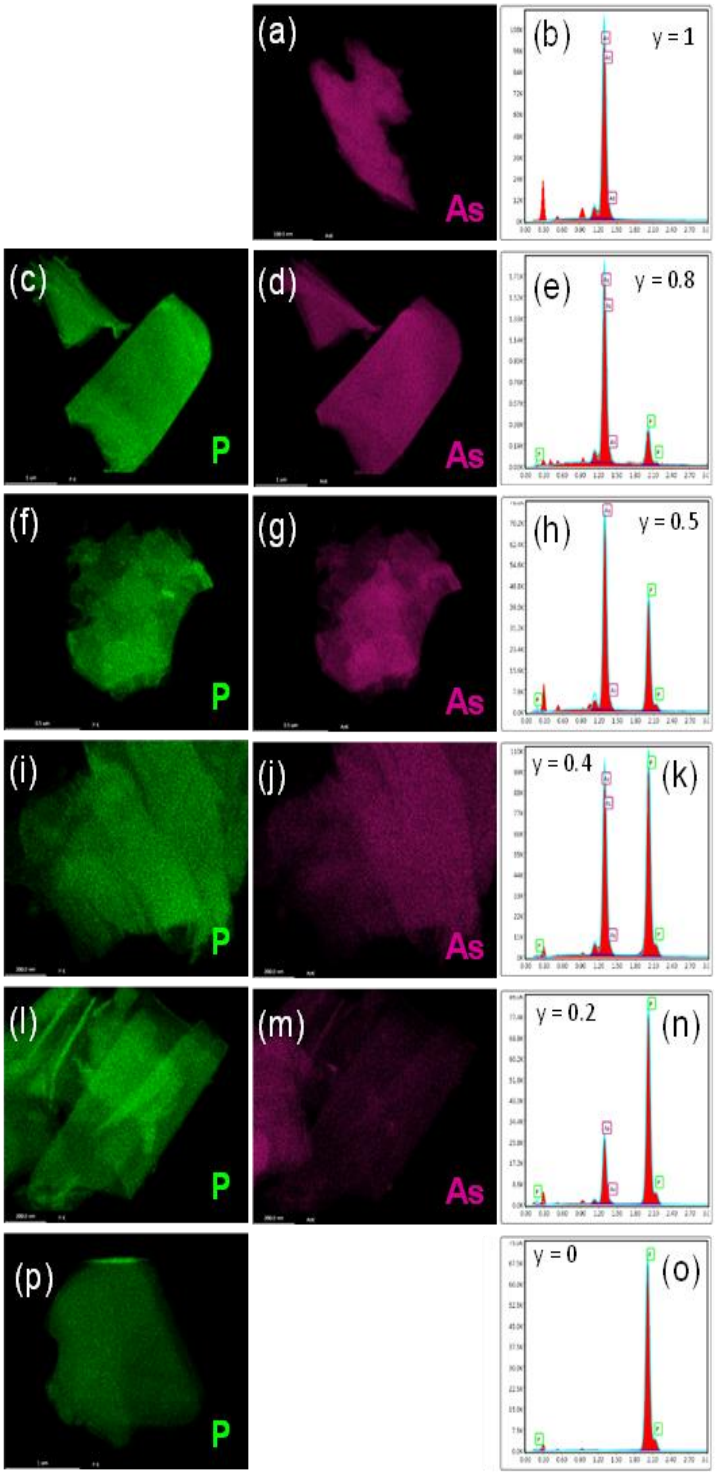

Figure 3.09: EDS analysis of b-As_yP_{1-y} ($1 \geq y \geq 0$) samples: P-K elemental maps (left panels), As-K elemental maps (middle panels), and EDS spectra (right panels).

In summary, all b-As_yP_{1-y} alloys were found to exhibit a layered morphology along with a reasonably homogeneous elemental composition.

3.2. Electrochemical Li intercalation

Based on our previous study, which revealed the structural expansion caused by Li intercalation in BP, it is of significance to investigate the impact of Li intercalation on b-As_yP_{1-y} alloys. Raman spectroscopy is employed as a technique to observe alterations in the atomic vibrational modes, providing valuable insights into the intercalation mechanism.

In this experimental approach, the intercalation process is facilitated through the application of a discharge current to the system. This is achieved using a standard electrochemical cell setup, wherein the intercalants assume the role of the anode electrode and the host materials serve as the cathode electrode. The number of intercalated Li atoms per b-As_yP_{1-y} molecule, or the degree of lithiation (x), is determined by employing the following equation:

$$x = \frac{MIt}{e\,N_A m}$$

Where, M, I, e, N_A, and m are the molar mass of b-As_yP_{1-y}, discharge current, electron charge, Avogadro's number, and b-As_yP_{1-y} mass (active mass), respectively. As all the parameters are constants for a given cell, and if the discharge current is also constant (galvanostatic), the degree of lithiation (x) is linearly proportional to the discharge time(t).

3.2.1. Structural and vibrational properties upon Li intercalation

We then, performed detailed analyses to understand the atomic mechanism of the effects of Li intercalation on the structural properties of b-As_yP_{1-y} alloys in terms of

(i) the charge transfer from Li,

(ii) the peak area, shift of Raman spectrums and relative change of the intensity of the new Raman peak, and

(iii) the characteristics of XRD patterns before and after Li intercalation.

Figure 3.10 (a) shows the Galvanostatic discharge curves for samples with varying As concentration y in b-As_yP_{1-y} used for in-situ Raman spectroscopy. The results for precursor-As are also shown. The open circuit voltage (OCV) for each sample was seen to depend on the As concentration *y*, as shown in Figure 3.10 (b). For all the samples with orthorhombic phase, the OCV showed a monotonic increase with the increasing As concentration. However, precursor-As (g-As) with rhombohedral phase, shows a clear deviation from this behavior. The open-circuit voltage of an electrochemical cell depends on the electrochemical potentials of the constituent materials and the theoretical voltage is determined by the Nernst Equation.

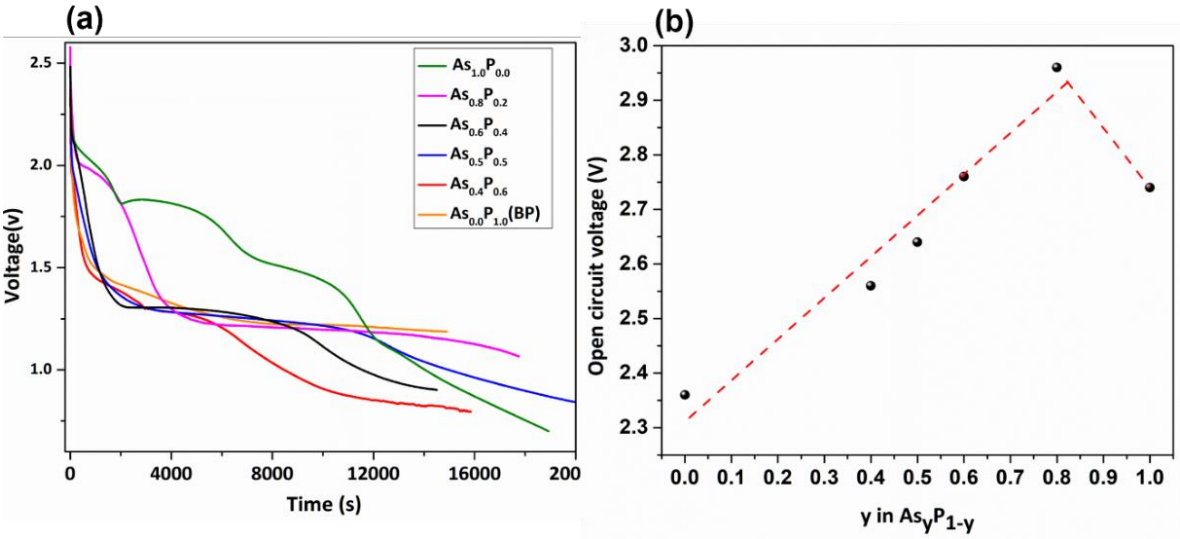

Figure 3.10: (a) Galvanostatic discharge curves for samples with varying As concentration, y in b-As_yP_{1-y} used for in-situ Raman spectroscopy. The results for precursor-As are also shown. (b) Open circuit voltage (OCV) as a function of As concentration y.

Open circuit voltage

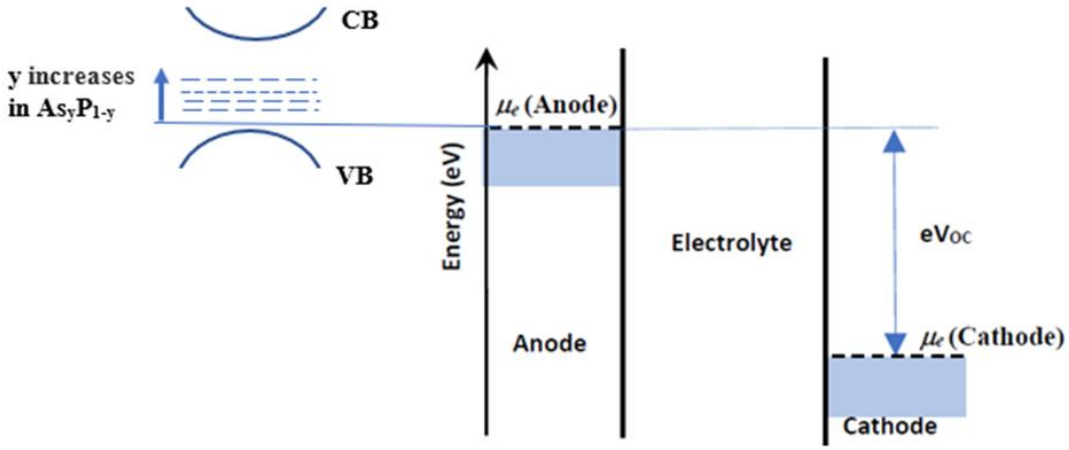

Figure 3.11: Electrochemical potential diagram of an electrochemical cell

Ideally, during the discharge process, the electrodes undergoing redox reactions, enable electrons to flow through the external circuit in the direction from anodes with higher Fermi energy to cathode material with a lower one. Therefore, the open-circuit voltage of the cell system satisfies,

$$FV_{oc} = -\Delta E_F = \mu_A - \mu_C$$

where F represents Faraday's constant. For the common solid electrode materials, the Fermi energy level depends on the material's work function.

Our previous study (Karki et al.) has shown that BP (As_0P_1) is a p-type semiconductor with the thermoelectric power (TEP) value ~ +323 mV/K at room temperature[33]. As y increases in As_yP_{1-y}, the TEP value is seen to decrease monotonically reaching ~ 8 mV/K for y=0.8. This implies the Fermi energy for BP (y=0) lies closer to the valence band edge and moves towards the center of the band as y increases. This makes the $\mu_A - \mu_C$ increase as y increases and hence the V_{OC}.

To study the effect of electrochemical Li intercalation on the structures of b-As_yP_{1-y} alloys, we intercalated Li in the samples and present the results of Li-intercalation in each of the b-As_yP_{1-y} by investigating the evolution of the Raman spectra in-situ during the intercalation. Figure 3.12 consists of Raman spectra and degree of lithiation x in Li_x(b-As_yP_{1-y}) for different b-As_yP_{1-y} alloys with varying *y*. In each Raman spectrum, three major regions of peaks corresponding to P-P bonds (≈ 300 – 470 cm^{-1}), As-As bonds (≈ 200 – 300 cm^{-1}), and As-P bonds (≈ 300 – 400 cm^{-1}) are observed. The shaded area around 200 cm^{-1} in each spectrum (except BP) identifies the evolution of a new peak as a result of intercalation. It is believed that the new peak developed during the lithiation in b-As_yP_{1-y} alloys is associated with a small amount of rhombohedral g-As phase developing from orthorhombic b-As_yP_{1-y} in the samples with mixed composition after a threshold degree of lithiation in each sample. This peak is identified as the E_g mode of g-As. Careful investigation by systematic curve fitting procedure reveals the existence of A_{1g} mode of the g-As phase in addition to the E_g mode. However, the proximity of the presence of A_g^2 mode (b-As phase) of the b-As_yP_{1-y} alloy and the A_{1g} mode of the g-As phase makes this analysis difficult.

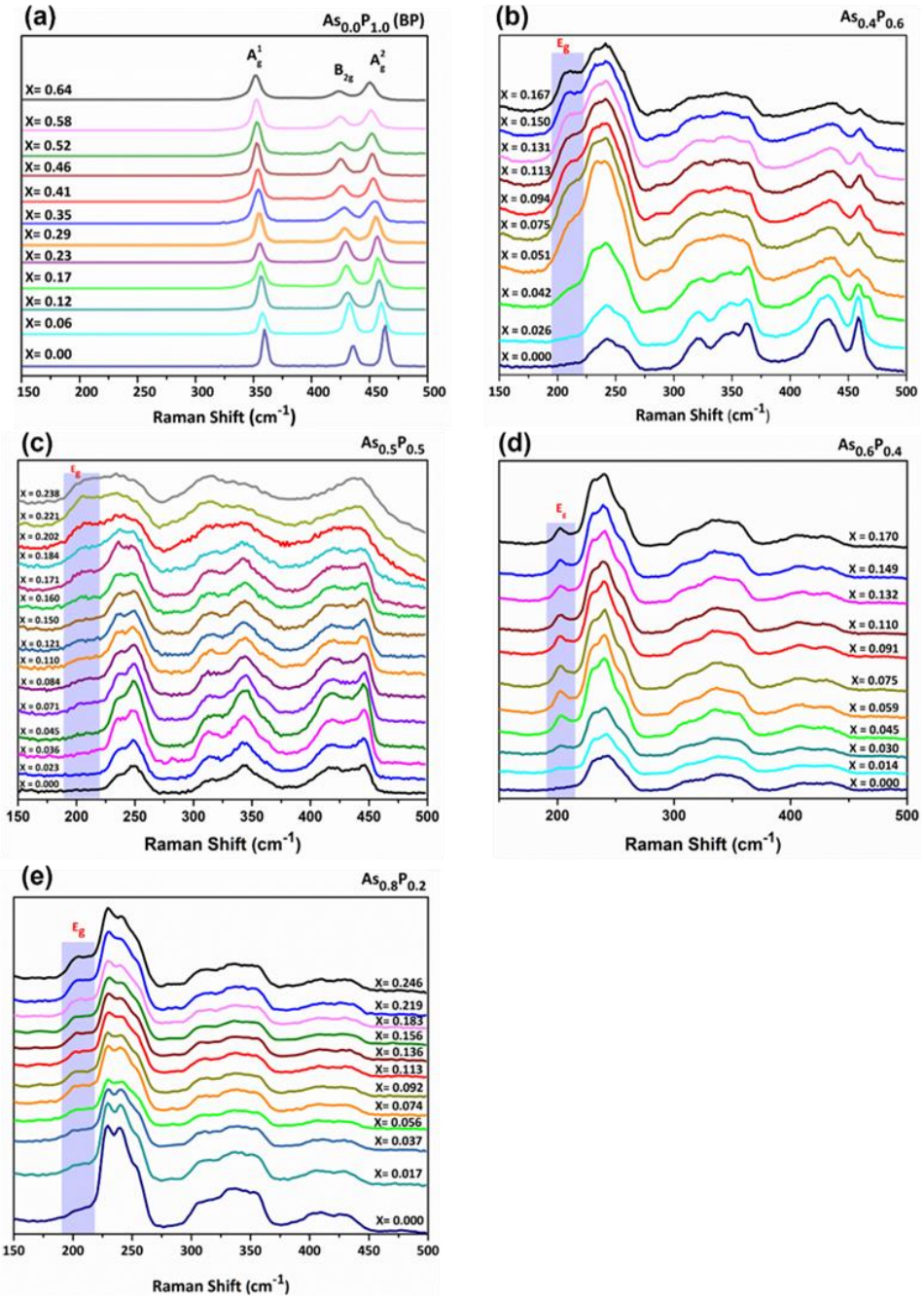

Figure 3.12: Comparison of Raman spectra at different instances of time during the Li intercalation for varying As concentration, y in b-As_yP_{1-y}; (a) y = 0 (b) y = 0.4 (c) y = 0.5, (d) y = 0.6 (e) y = 0.8. The shaded area in each spectrum identifies the evolution of a new peak (identified as the E_g mode of g-As) as a result of intercalation. Corresponding intensity maps of Raman spectra during Li intercalation are provided in Figure 3.13.

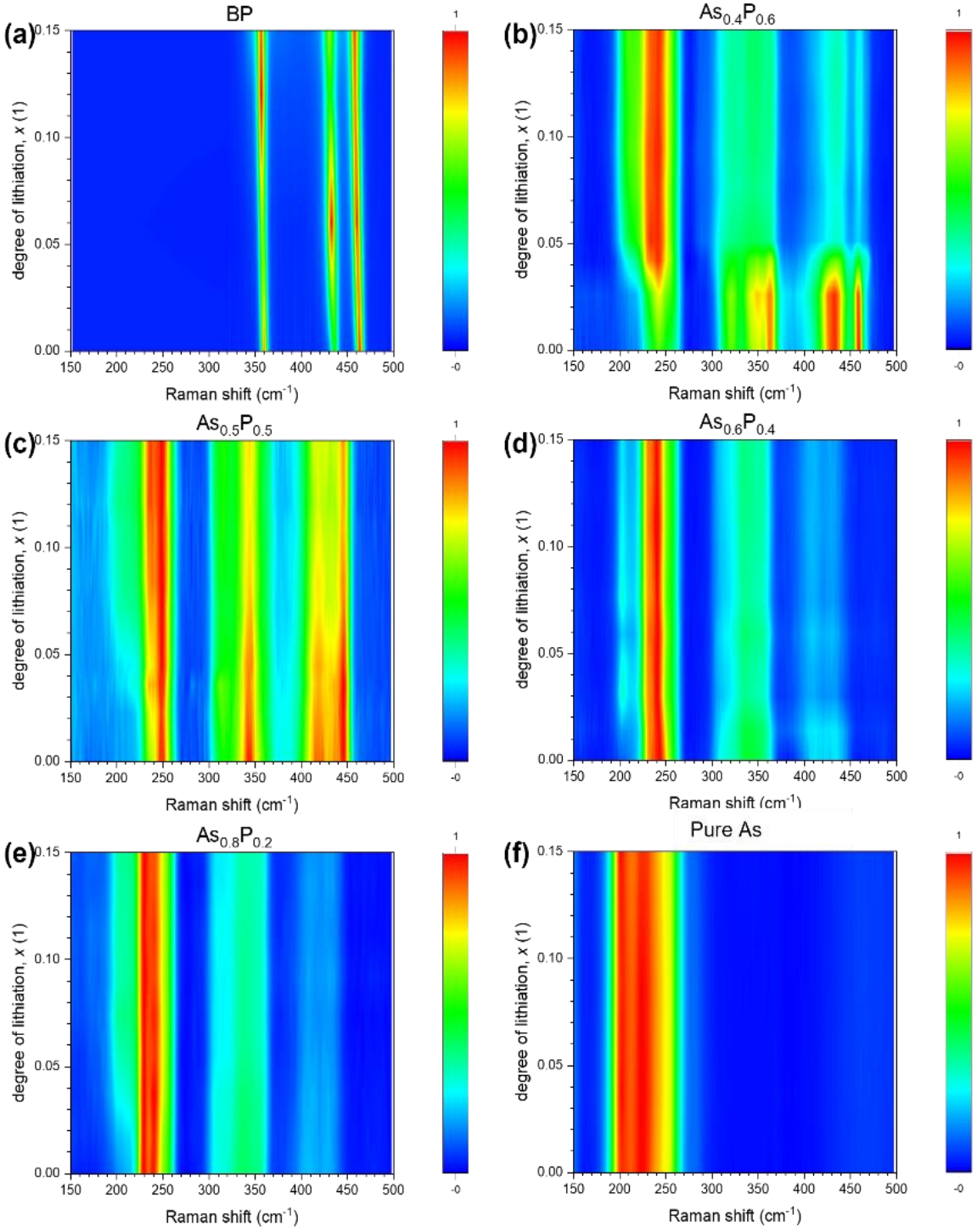

Figure 3.13: Maps of Raman signal vs. lithiation degree for different b-As_yP_{1-y} alloys; (a) y = 0 (b) y = 0.4 (c) y = 0.5, (d) y = 0.6 (e) y = 0.8.

Figure 3.13 shows the Raman intensities (integrated areas) of P-P, As-As, and As-P peaks normalized to the total intensity for samples with varying As concentration, y in b-As_yP_{1-y}; (a) y = 0 (b) y = 0.4 (c) y = 0.5, (d) y = 0.6 (e) y = 0.8. For all the samples, the normalized intensity of P-P bands and As-P bands are seen to decrease as the intercalation progresses. However, for the sample with y = 0.8, the changes are minimal. For the sample with y = 0.4, the normalized intensity of P-P and As-P bands are higher compared to the As-As band prior to the intercalation (x = 0). During the intercalation, while the intensity for P-P and As-P bands decrease, the intensity of As-As band increases rapidly and saturates implying emergence of the g-As phase. The sample with y = 0.5 shows somewhat similar behavior except for the changes of the intensity of the P-P and As-P bands are somewhat less. For the sample with y = 0.6, the normalized intensity of the As-As band is larger than that of P-P and As-P bands before the intercalation due to the higher As concentration of the pristine sample but undergoes similar changes upon intercalation. For the sample with y = 0.8, the intensity of As-As bonds is much higher than that of P-P and As-P bands in the pristine state and all the intensities show negligible changes upon intercalation. The faster quenching of P-P bands compared to P-As and As-As bands, observed during intercalation, is consistent with the faster environmental degradation of BP compared to b-As_yP_{1-y} alloys.[27]

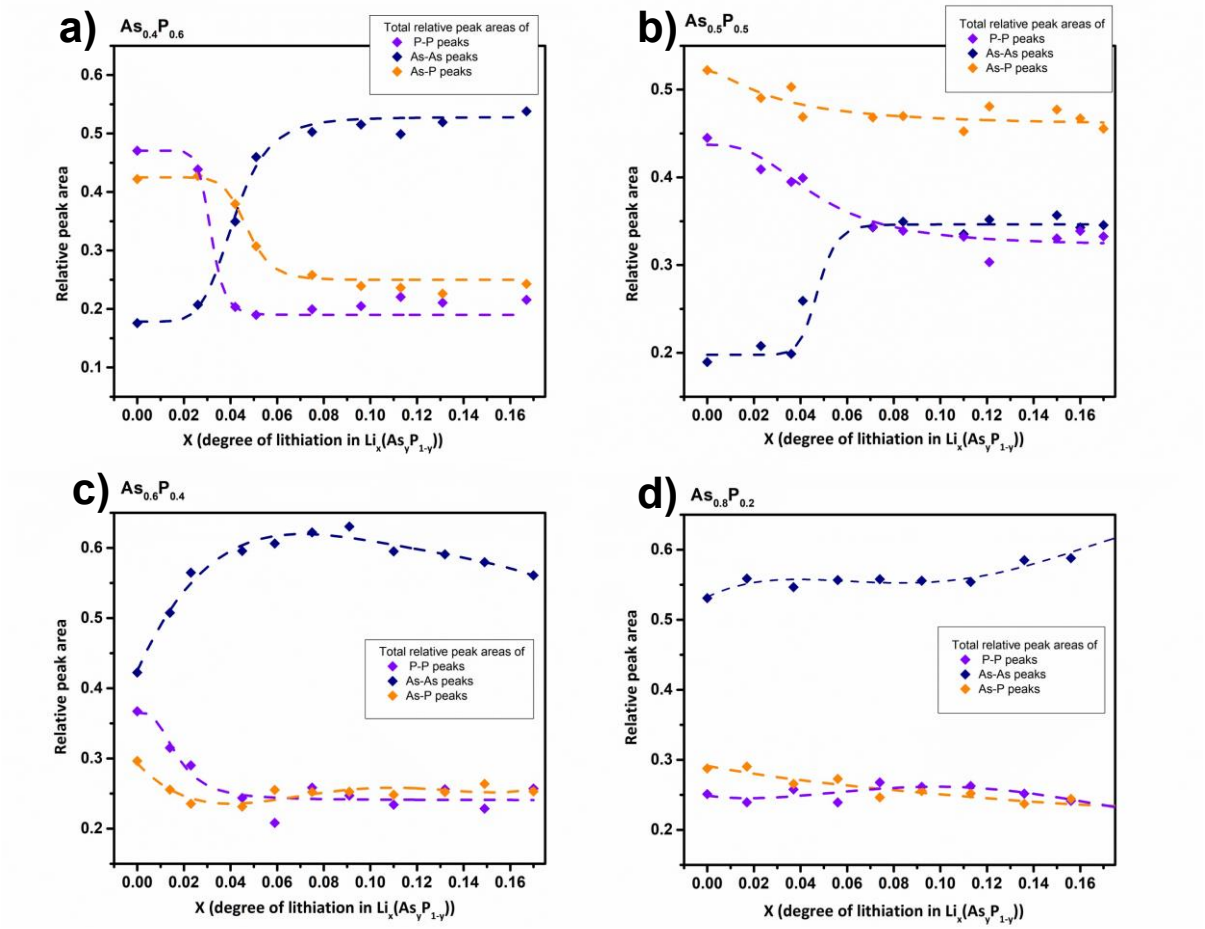

Figure 3.14: Comparison of Raman peak intensities (integrated area) of P-P, As-As, and As-P peaks normalized to the total intensity for varying As concentration, y in b-As_yP_{1-y}; (a) y = 0.4 (b) y = 0.5 (c) y = 0.6, (d) y = 0.8 The As-As peak constitutes of b-As (A^1_g, B_{2g} and A^2_g) and g-As (A_{1g} and E_g).

Figure 3.15 (a) shows the Raman shifts of the new peak plotted against the degree of lithiation, *x* in Li_x(b-As_yP_{1-y}) for varying y. We define the critical concentration of Li where the new modes (E_g and A_{1g} modes of g-As) appear to emerge as X_i. For each b-As_yP_{1-y} alloy composition, we monitored the formation and evolution of the E_g mode's intensity by carefully and systematically deconvoluting Raman spectra measured at each lithiation stage (i.e., at each level of lithiation, *x*), including pristine (non-lithiated) samples. The intensity of the E_g peak was found to be negligible for all samples until X_i. Only for

the largest y value of 0.8, the new peaks are already present in the as prepared sample (i.e., $X_i = 0$) indicating partial development of arsenic in the form of g-As crystal structure due to the instability caused by excessive As. For other samples, X_i increases linearly as y decreases, as shown in Figure 3.15 (b). This behavior can be explained as more degree of Li intercalation is required to cause bond breaking and drive the process of g-As developing from b-As_yP_{1-y} alloys with low y. Next, the critical x value, X_c, where the Raman shift starts to downshift after the maximum upshift is indicative of the completion of the phase segregation process driven by the intercalation. Since this process is governed by the interplays among thermodynamic and kinetic factors, the dependance of X_C on y is not monotonic. Finally, the slopes of the initial rise ($X_i < x < X_c$) and the subsequent decrease ($x > X_c$) are shown in Figures 3.15 (c) and (d), respectively. Each slope is seen to increase (positively) and decrease (negatively) respectively with y. As the arsenic concentration (y) increases, the segregation of the g-As phase from b-As_yP_{1-y} alloys becomes more prominent and as a result Li-intercalation imparts further strain on the As-As bonds. Therefore, as y increases, the blue shifting of the new peak increases somewhat linearly up to X_c as seen in Figure 3.15 (c). Beyond X_c, the two phases (g-As and b-As_yP_{1-y}) are well segregated, and the charge transfer is the dominant mechanism for Raman shifting. It is also reasonable to presume that once the phases are completely segregated, the sample with higher y values will have a reduced effect on the g-As phase due to charge transfer as seen in Figure 3.15 (d). This is because the segregated g-As phase in higher y value samples has higher strains on As-As bonds (blue-shift) and compensates for the charge transfer induced red-shift.

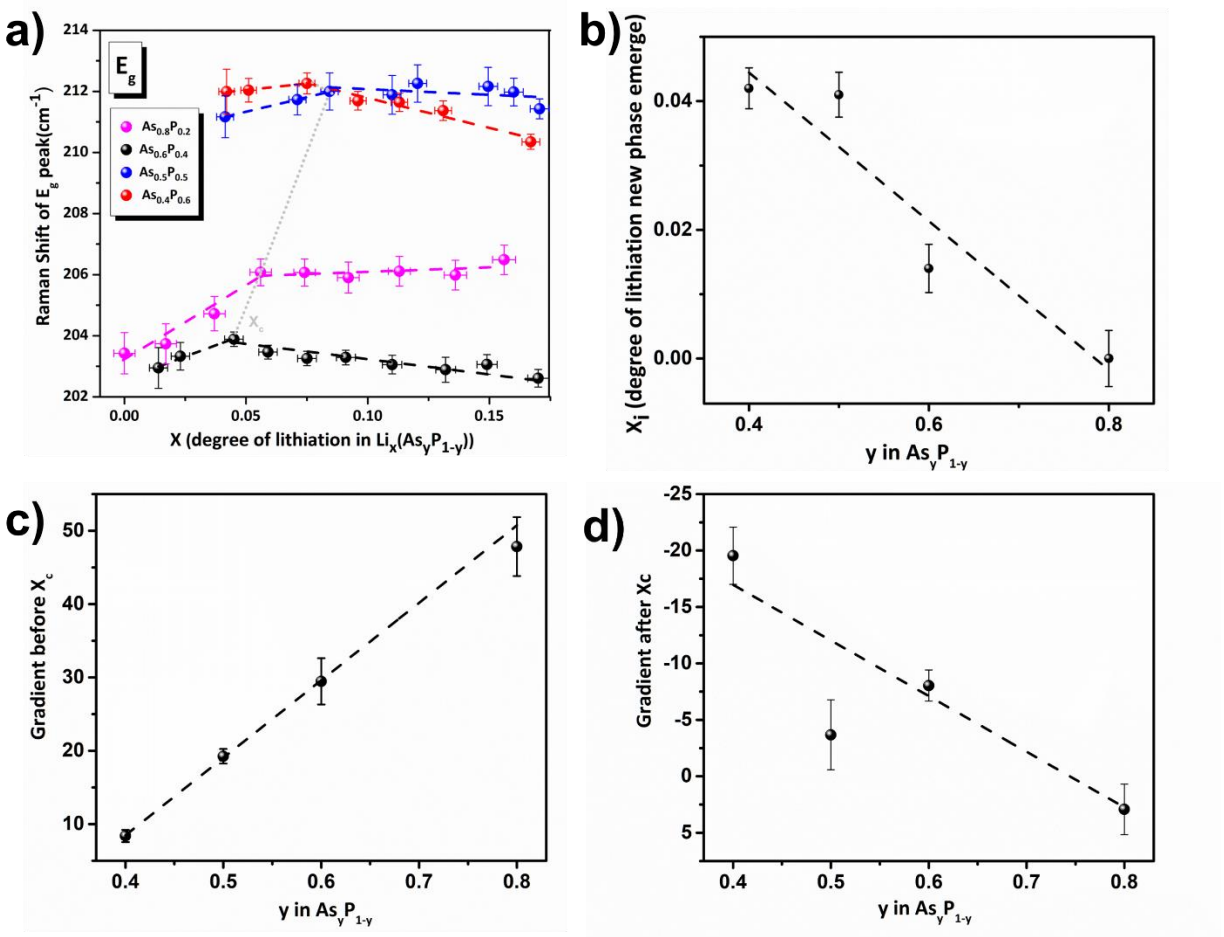

Figure 3.15: (a) Raman shifts of the E_g peak plotted against the degree of lithiation, x in $Li_x(b\text{-}As_yP_{1-y})$. The critical x value, X_c, where the Raman shift starts to downshift after the maximum upshift is marked guided in dashed gray line.(**b)** The initial x value, X_i, where the new mode (E_g mode of g-As) appears to emerge, **(c)** the slopes of the initial rise ($X_i < x < X_c$), and **(d)** the subsequent decrease ($x > X_c$) are also plotted.

To elucidate this point, we looked at the relative change of the intensity of the new peak (E_g mode of the g-As) normalized to the intensity at X_i, i.e., $(\Delta I/I)$ as a function of x in $Li_x(b\text{-}As_yP_{1-y})$ for samples with varying y as shown in Figure 3.16. The dotted lines are the guides to the eye. The relative change of the intensity of the new peak $(\Delta I/I)$ shows a systematic increase as y increases from 0.4 to 0.6 by reaching higher peak values as well as higher saturated values for higher x values. For these three samples, the new peak only

starts to appear after a non-zero intercalation level, X_i. However, for the highest y value of 0.8, the new peak is already present (X_i =0) in the pristine sample and the relative change remains low as seen in Figure 3.16 implying at y = 0.8, part of the sample is already undergoing phase separation from orthorhombic (b-As_yP_{1-y}) to rhombohedral phase (g-As), yet another part still remains as orthorhombic b-As_yP_{1-y}. For other samples, Li-intercalation is believed to drive the development of this phase segregation. The A_{1g} mode of the g-As phase is also expected to exhibit similar behavior, but the proximity of the presence of the A_g^2 mode of b-As phase of b-As_yP_{1-y} alloy and the A_{1g} mode of the g-As phase limits accurate and reliable determination of the A_{1g} mode of the g-As phase.

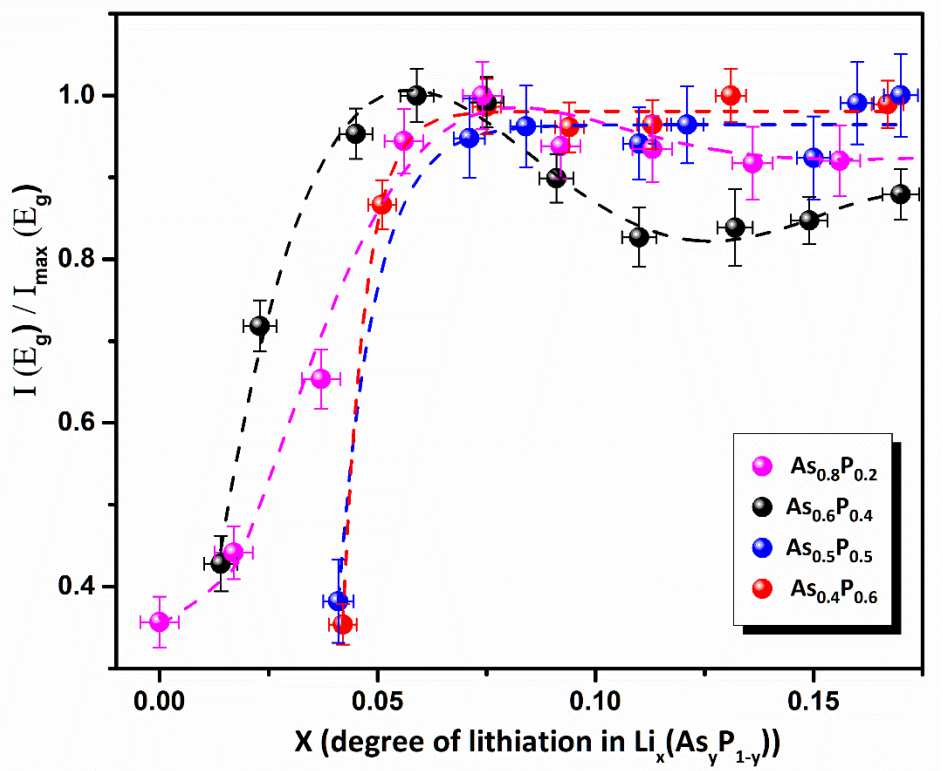

Figure 3.16: The relative change of the intensity of the E_g peak of gray As normalized to the intensity at X_i ($\Delta I/I$) as a function of x in Li_x(b-As_yP_{1-y}) for samples with varying y. The dotted lines are the guides to the eye.

Figure 3.17 shows the XRD patterns for pristine BP and b-As_yP_{1-y} alloys with different chemical compositions before and after Li intercalation. The inset shows the

blown-up view of the (040) peak before and after Li intercalation of each sample with varying alloy composition, *y*. In each sample, the 2θ value is seen to decrease after intercalation implying the expansion of the interplanar spacing. In order to understand whether the lattice expansion occurred isotropically in all directions, the position of several peaks in b-$As_{0.5}P_{0.5}$ XRD pattern was analyzed before and after the intercalation. These results shown in Table 3.2 were used to evaluate the relative lattice expansion along the main three crystallographic directions, i.e. along a-, b-, and c-axis (Table 3.3). It can be seen that the largest lattice expansion occurred along the c-direction. This is consistent with the expected expansion of such hinge-like structure, as reported recently for Li-intercalation in BP[54].

Further, a new peak (2θ = 32.5°) adjacent to the (040) peak appears to emerge after Li-intercalation. This can be attributed to a local structural change of at least part of the sample from orthorhombic to rhombohedral due to Li intercalation. However, the sample with highest As concentration (y = 0.8), exhibits such features even in the pristine state (prior to the intercalation). This is consistent with the Raman results confirming structural segregation due to the increased As concentration causing part of the sample to undergo such structural change. This is also consistent with EDS elemental mapping of this sample where excess of As particles were observed in addition to b-$As_{0.8}P_{0.2}$ flakes (see example EDS mapping in Figure 3.08).

Table 3.2: XRD peak positions before and after intercalation for sample b-$As_{0.5}P_{0.5}$.

h k l	**$As_{0.5}P_{0.5}$**		
	Pristine	**Intercalated**	**Relative change**
	$2\theta_p$ (deg)	**$2\theta_i$ (deg)**	**$\Delta\theta/\theta_p$**
0 2 0	16.45	16.39	-0.0037
0 2 1	25.96	25.77	-0.0071
0 4 0	33.25	33.12	-0.0038
1 1 1	34.23	34.05	-0.0053
0 6 0	50.82	50.62	-0.0040
0 6 1	55.12	54.86	-0.0048
1 3 2	55.59	55.20	-0.0071

Table 3.3: Lattice parameters for sample b-$As_{0.5}P_{0.5}$ before and after intercalation.

lattice parameter	**$As_{0.5}P_{0.5}$**		
	Pristine	**Intercalated**	**Relative change**
a (Å)	3.395	3.405	0.0029
b (Å)	10.771	10.811	0.0037
c (Å)	4.449	4.490	0.0092

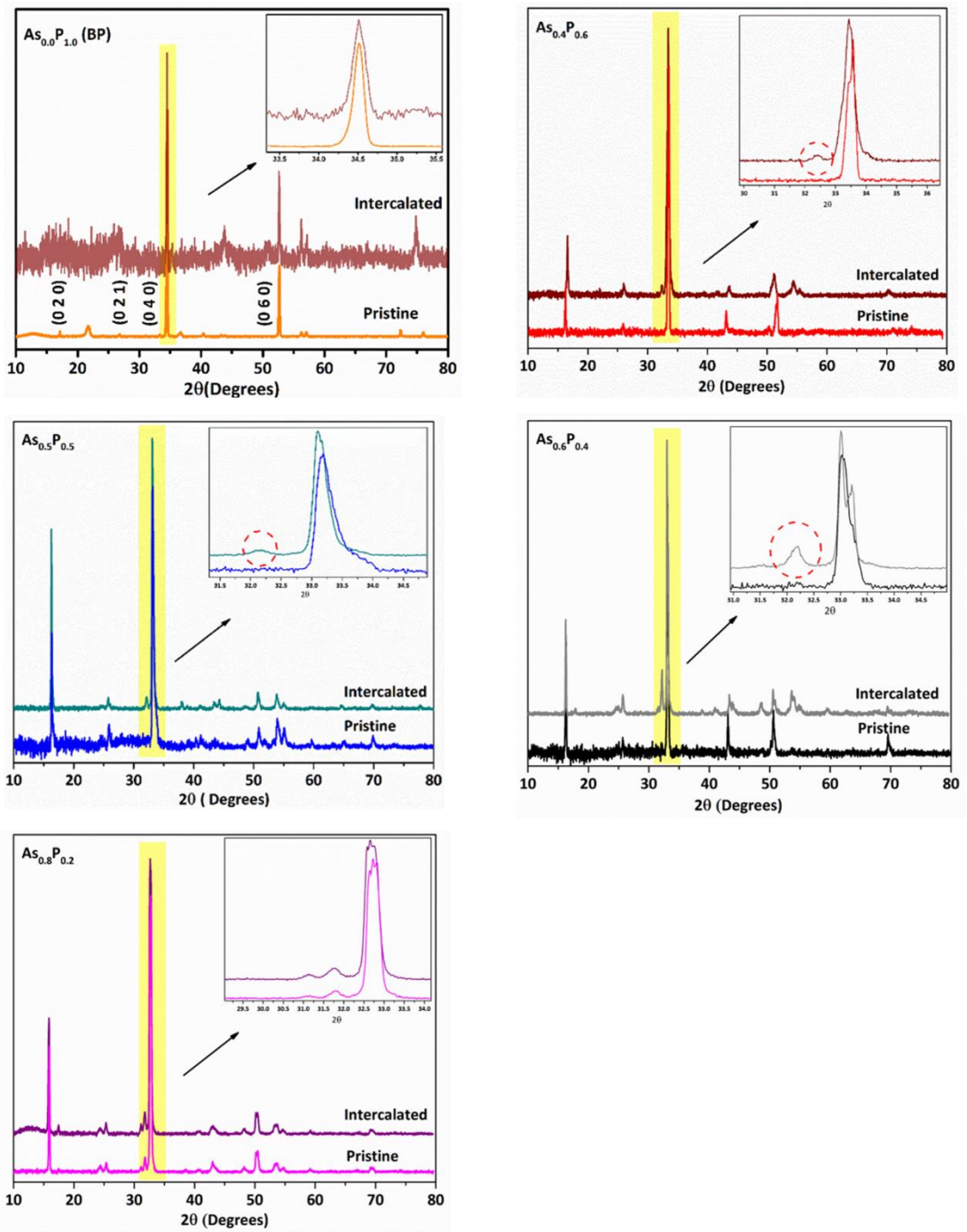

Figure 3.17: XRD patterns for pristine BP, precursor As and b-As_yP_{1-y} alloys with different chemical compositions before and after Li intercalation. The inset shows the blown-up view of the (040) peak before and after Li intercalation of each sample with varying alloys composition y.

The crystallite size and lattice strain

Bulk samples consisting of crystals with sizes smaller than 8mm were synthesized. For the electrochemical cell, samples were crushed to make the cathode. Consequently, the particle size is highly dependent on the mechanical process, which may introduce inconsistencies. Assuming that all samples have the same particle size, the Williamson–Hall method is used to calculate the crystallite size and lattice strain.

The broadening of peaks is indicative of grain refinement and the presence of significant strain within the material. The instrumental broadening ($\beta_{hkl}, \text{instrumental}$) was estimated for range of diffraction angles using NaCl as a reference. The following equation is used to calculate corrected (instrumental broadening) full width at half maximum[99].

$$\beta_{hkl} = [(\beta_{hkl}, \text{measured})^2 - (\beta_{hkl}, \text{instrumental})^2]^{1/2}$$

The average crystallite size (D) was calculated from XRD peak widths based on the Debye – Scherrer equation,

$$D = \frac{K\lambda}{\beta_{hkl} \cos\theta}$$

Where K is the shape factor (0.9), λ is the wavelength of the incident X-ray (λ = 0.1540 nm), and θ is the Bragg angle. The calculation of strain (ε) induced in crystals resulting from crystal imperfections and distortions involve the formula,

$$\varepsilon = \frac{\beta_{hkl}}{4 \tan\theta}$$

Using the equations mentioned above, the total broadening of the peaks is determined by considering both the crystallite size and strain present in the material.

$$\beta_{hkl} = \frac{K\lambda}{D\cos\theta} + 4\varepsilon \tan\theta$$

By rearranging the equations, we get[100],

$$\beta_{hkl}\cos\theta = 4\varepsilon \sin\theta + \frac{K\lambda}{D}$$

A linear plot is generated by plotting $\beta_{hkl}\cos\theta$ vs 4sin θ. The y-intercept of the linear fit can be used to determine the crystallite size(D), while the slope of the fit corresponds to the strain (ε). This method was used to determine the crystallite size and lattice strain of each sample.

Table 3.4: Calculated crystallite size and lattice strain values of b-As_yP_{1-y} alloys

Y	Crystallite Size (nm)		Lattice Strain	
	Pristine	Intercalated	Pristine	Intercalated
0	97.938	48.969	0.0008	0.0003
0.4	124.649	80.655	0.0034	0.0046
0.5	137.113	72.165	0.0042	0.0026
0.6	88.460	50.783	0.0015	0.0016
0.8	195.877	137.113	0.0042	0.0055

According to the obtained results, an overall increase in crystallite size was observed with an increase in As concentration. This can be attributed to the larger diameter of As atoms compared to P atoms, causing slight outward displacement of As atoms within

the primitive unit cell. Consequently, we evidenced an expansion of the unit cell parameters occurred with increasing As concentration, leading to an increment in crystallite sizes. Intercalation, on the other hand, resulted in a decrease in crystallite size. This can be attributed to the exfoliation of the layers and subsequent cracking of the crystallites caused by intercalation. The reported reduction in crystallite size during Na intercalation into Bi suggests particle pulverization or cracking of the crystallites as a result of intercalation[101].

A slight increasing trend in lattice strain was also observed with increasing As concentration and due to intercalation, although these changes were minimal. It should be noted that because of the low quality of our XRD data, it may restrict our ability to draw conclusions regarding subtle changes.

Finally, we carefully analyzed the influence of intercalation on all the P-P, As-As, and As-P Raman peaks for all 4 samples with varying *y* values as shown in Figure 3.18. The first raw from left to right in Figure 3.18 represents the Raman shifts as a function of the degree of lithiation for A_g^2, B_{2g} and A_g^1 vibrational modes of the P-P bonds, respectively. The middle row shows the Raman shifts for the two As-P modes due to the Li-intercalation. The third raw from left to right in Figure 3.17 represents the Raman shifts as a function of the degree of lithiation for A_g^2, B_{2g} and A_g^1 vibrational modes of the As-As bonds, respectively.

All the P-P modes for all 4 samples except the A_g^1 mode of the sample with y = 0.8 show a redshift (or negligible change) up to X_c (during the completion of the segregation process) consistent with the donor type charge transfer to the b-As_yP_{1-y} phase thereby softening the Raman mode. Beyond X_c, all the modes except the A_g^1 mode of the sample

with y = 0.8 undergo an upshift (or negligible change) consistent with bond shortening (hardening of the Raman mode) due to the strain imparted on the b-As_yP_{1-y} phase by the segregated and strained g-As phase. The anomalous behavior of the P-P A_g^1 of the sample with y = 0.8 (upshift) can be understood as the pristine sample is already phase segregated and the Li-intercalation imposes additional strain on the b-As_yP_{1-y} phase.

The As-P bonds for all the samples except the sample with y = 0.8 show negligible or slight downshift for $x < X_c$ due to donor type charge transfer mechanism. The anomalous behavior (upshift) of the sample with y = 0.8, is due to the phase segregation of the pristine sample prior to the Li intercalation. For $x < X_c$, both modes for all 4 samples undergo a redshift (or negligible shift) due to charge transfer.

All the As-As modes of all the samples except the sample with y = 0.8 show a similar behavior of initial downshift (or negligible shift) for $x < X_c$ followed by a blueshift (or negligible change) for $x > X_c$. Again, the anomaly in the sample with y = 0.8 (upshift for $x < X_c$) is due to the phase segregation of the pristine sample undergoing additional strain due to Li-intercalation.

In addition to the effects discussed earlier, there can be some complications arising from some other factors discussed below. In the case of Li intercalation into layered vdW solids, the metal ion insertion has been reported to induce an increase of the lattice constant at the basal plane when the sample is supported on a substrate. It is also likely the flake can undergo compressive strain due to the constraint from the metal substrate. However, the effect of the substrate is minimum in our case due to the larger thickness of the samples containing many layers. Meanwhile, the electron doping will cause the Raman modes softening to lower wavenumber. Alkali metal intercalation leads to an increase in the

electron density of a crystal and, hence, an increase in bond lengths and decrease in vibrational frequencies.

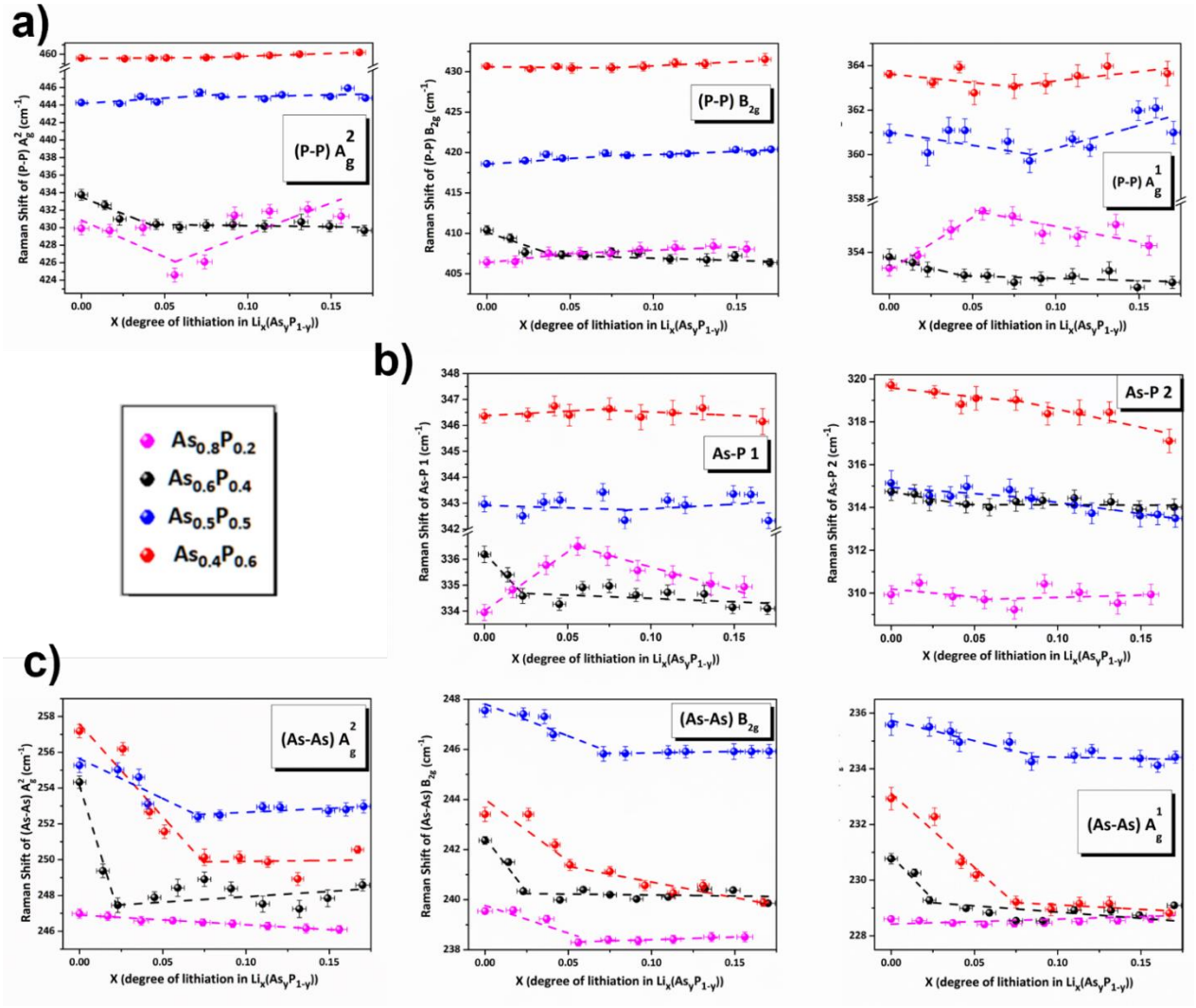

Figure 3.18: Raman shifts plotted against the degree of lithiation, x in $Li_x(b\text{-}As_yP_{1-y})$ for (a) P-P modes (A^1_g, B_{2g} and A^2_g) (b) As-P modes and (c) As-As modes (A^1_g, B_{2g} and A^2_g). The dotted lines are linear fits at different intercalation regions.

Overall, the movement of the Raman bands will be a synergetic effect of these two factors, i.e., strain (compressive) and electron doping. At various stages of Li intercalation, the doping effect competes with strain effects and the Raman bands shifts accordingly. Phase segregation will also contribute to the overall Raman shifts. During different stages of the intercalation, depending on the initial material, one effect dominates over the other,

for different Raman bands. On the other hand, the in-plane vibrations (B_{2g} and A_g^2) provides information on the in-plane strain, while the out-of-plane mode (A_g^1) gives evidence for the interaction with the substrate. The softening of A_g^1 mode suggests reduction of interlayer van der Waals forces (i.e., decoupling effect), leading to weaker restoration force in the vibrational mode.

Further, the starting material is most likely a mixture of alloys with slightly varying compositions. Additionally, a small amount of rhombohedral arsenic can be present in samples with mixed composition most likely as an unreacted residue of the reaction mixture. According to Raman and XRD, the content of rhombohedral arsenic is slightly higher in the sample with higher As concentration (b-$As_{0.8}P_{0.2}$).

3.2.2. Theoretical calculations

The experimental results on Li intercalated BP were backed by first principal calculations based on density function theory (DFT). The credit of this theoretical work goes to Dr. Ming Yu and Tasnim Kazi.

To understand such Li induced structural segregation from a b-As_yP_{1-y} alloy to a combined system of b-$As_{y-p}P_{1-y+p}$ alloys plus g-As (where *p* denotes the percentage of As atoms segregated from b-As_yP_{1-y} alloys forming g-As), we calculated the cohesive energies of b-As_yP_{1-y} alloys and compared with combined systems with the *p* value of 12.5%, as an example. As shown in Table 3.5(a), the combined systems are energetically stable than the b-As_yP_{1-y} alloys, the richer the As concentration, the lower the relative energy, supporting the coexistence of b-As_yP_{1-y} alloys with g-As. We also analyzed the relative cohesive

energy of combined system (i.e., b-$As_{y+p}P_{1-y-p}$ alloys plus blue P) to the b-As_yP_{1-y} alloys (Table 3.5 (b)) and found that the combined system is energetically higher (unstable) than b-As_yP_{1-y} alloys. The exception is found in As-rich b-$As_{0.875}P_{0.125}$ alloy, where the relative energy is lower in the combined system (-0.0128 eV/atom, Table 3.4 (b)). But it is still higher than that of the combined system with g-As (-0.0677 eV/atom, Table 3.5 (a)). Thus, the b-$As_{0.875}P_{0.125}$ alloy prefers to segregate with g-As, instead of blue P. This is because that, even though the formation energy of blue P is slightly higher than BP (~0.0058 eV/atom Table 3.6 (b)), blue P is a metastable structure. The g-As, on the other hand, is the most stable structure, and b-As is a metastable structure (~0.0415 eV/atom, Table 3.6 (a)). Therefore, it is energetically favorable to segregate g-As from b-As_yP_{1-y} alloys.

Table 3.5: The calculated cohesive energies of b-As_yP_{1-y} (E alloy) and combined system with 12.5% of g-As ($E_{combine}$) (a) or 12.5% of blue-P (b), as well as the relative energy ΔE (the 4th column).

(a)

b-As_yP_{1-y}	**E_{alloy} (eV/atom)**	**$E_{combine}$ (eV/atom)**	**$\Delta E=(E_{combine}-E_{alloy})$ (eV/atom)**
b-$As_{0.125}P_{0.875}$	-5.4293	-5.4530	-0.0237
b-$As_{0.25}P_{0.75}$	-5.3372	-5.3608	-0.0236
b-$As_{0.375}P_{0.625}$	-5.2435	-5.2803	-0.0368
b-$As_{0.5}P_{0.5}$	-5.1626	-5.1983	-0.0356
b-$As_{0.625}P_{0.375}$	-5.0728	-5.1275	-0.0547
b-$As_{0.75}P_{0.25}$	-4.9955	-5.0490	-0.0534
b-$As_{0.875}P_{0.125}$	-4.9136	-4.9813	-0.0677

(b)

b-As_yP_{1-y}	**E_{alloy} (eV/atom)**	**$E_{combine}$ (eV/atom)**	**$\Delta E=(E_{combine}-E_{alloy})$ (eV/atom)**
b-$As_{0.125}P_{0.875}$	-5.4293	-5.3611	0.0681
b-$As_{0.25}P_{0.75}$	-5.3372	-5.2791	0.0580
b-$As_{0.375}P_{0.625}$	-5.2435	-5.2084	0.0350
b-$As_{0.5}P_{0.5}$	-5.1626	-5.1298	0.0328
b-$As_{0.625}P_{0.375}$	-5.0728	-5.0622	0.0106
b-$As_{0.75}P_{0.25}$	-4.9955	-4.9905	0.0050
b-$As_{0.875}P_{0.125}$	-4.9136	-4.9265	-0.0128

Table 3.6: Formation energy of As_yP_{1-y} with orthorhombic (a) and rhombohedral (b) phases, respectively.

(a)

Orthorhombic As_yP_{1-y}	**E_f (eV/atom)**
$As_{0.0}P_{1.0}$	0
$As_{0.125}P_{0.875}$	0.0237
$As_{0.25}P_{0.75}$	0.0341
$As_{0.375}P_{0.625}$	0.0463
$As_{0.5}P_{0.5}$	0.0456
$As_{0.625}P_{0.375}$	0.0538
$As_{0.75}P_{0.25}$	0.0496
$As_{0.875}P_{0.125}$	0.0499
$As_{1.0}P_{0.0}$	0.0415

(b)

Rhombohedral As_yP_{1-y}	E_f (eV/atom)
$As_{0.0}P_{1.0}$	0.0058
$As_{0.167}P_{0.833}$	0.0319
$As_{0.33}P_{0.67}$	0.0376
$As_{0.5}P_{0.5}$	0.0449
$As_{0.67}P_{0.33}$	0.0348
$As_{0.833}P_{0.167}$	0.0239
$As_{1.0}P_{0.0}$	0

To understand the local atomic structural changes of b-As_yP_{1-y} alloys under Li intercalation at atomic scale, we performed the structural analysis within the framework of the density functional theory (DFT). The role played by the Li atoms during the Li intercalation in the b-$As_{0.375}P_{0.625}$ alloy was studied by inserting Li atoms at the most preferential adsorption sites along the zigzag valley[22,102]. A full relaxation process was performed allowing all atoms to freely move in the unit cell and releasing all restrictions on the lattice symmetry and the unit cell volume. Figure 3.18(a) shows the optimized structures of b-$As_{0.375}P_{0.625}$ under the Li intercalation process with various Li concentration (x). It was found that with increasing the Li concentration, the structural symmetry of the b-$As_{0.375}P_{0.625}$ alloy and the atomic bonds (e.g., P-P, As-P, and As-As bonds) underwent successive changes (indicated by the dashed-black circles in Figure 3.18). For instance, at x = 0.125, the layer-layer stacking arrangement changes from the symmetric AB stacking to an antisymmetric AB stacking. At x = 0.25, the structural symmetry changes from orthorhombic to rhombohedral (which can be seen the significant increase of lattice angle

α in Table 3.7) but maintains the symmetric AB stacking. When the Li concentration reached a critical concentration X_c, a local structural transition (e.g., at $x = 0.375$) was found to take place. Some armchair bonds (especially As-As bonds) started to break (see figure 3.19 and the 4th column in Table 3.7), resulting in series of segments along the zigzag direction. Some of them show six-membered rings linked in trans-decalin fashion, forming rhombohedral nanoribbons. When the Li concentration x reaches 0.5, the shape of the lattice symmetry changes from rhombohedral back to the orthorhombic (see the lattice angle α in Table 3.7) and more armchair bonds are broken, forming a co-existence of the rhombohedral nanoribbons and buckled zigzag chains. These changes in the local structure reflect the effect of Li intercalation on the atomic structure, lowering the structural symmetry. Especially, the rhombohedral nanoribbons, induced by Li intercalation at $x \geq 0.375$, characterize the feature of A7 symmetry.

Table 3.7: Bond lengths and lattice angles of b-$As_{0.375}P_{0.625}$ alloy during the Li intercalation process with different Li concentration (x).

x	**P-P (Å)**	**As-P (Å)**	**As-As (Å)**	**α (degree)**	**β (degree)**	**ϒ (degree)**
0.125	2.26	2.38	2.60	99.09	89.99	89.86
0.25	2.26	2.39	2.57	111.96	89.99	90.00
0.375	2.25	2.39	-	67.35	89.99	90.00
0.5	2.23	2.40	-	92.49	90.09	90.04

Furthermore, the charge redistribution during Li intercalation in real space was evaluated from the difference of the electron charge density $\Delta\rho$, defined as $\Delta\rho = \rho_{total} - \rho_{alloy} - \rho_{Li}$, where ρ_{total} is the total electron charge density of the combined

system, ρ_{alloy} and ρ_{Li} are the electron charge densities associated with b-$As_{0.375}P_{0.625}$ alloy and Li atoms in the combined system, respectively. As shown in the insets of Figure 3.18, each Li atom is found to transfer about 0.97 *e* to the alloy. As the Li intercalation progresses, the amount of charge transfer is seen to increase accordingly (see Table 3.8). It was found that Li atoms act as a 'catalyst' in the 'reactive region' of the lone pair of P (As) atoms, leading to a bond breaking and subsequently, a local atomic structural transformation from orthorhombic to an assembly of rhombohedra-like nanoribbons. It should be noticed that the structural analysis based on the DFT modeling is at the atomic scale within the primary unit cell size (8 atoms) and hence can only characterize the bond breaking/reforming process. The development of rhombohedral phase (*e.g.*, g-As) segregated from b-As_yP_{1-y} alloys during Li intercalation observed in our experiments took place at entire sample, and such molecular dynamic process for a large size of system is beyond the ability of DFT computation. Since the energy barrier for atoms to migrate and diffuse after bond breaking is much higher (by over several eV/atom), a large-scale supercell containing at least several hundred atoms is required for the computations.

Table 3.8: Average net charge transfer of b-$As_{0.375}P_{0.625}$ under different Li concentration (x).

x	**As (*e*)**	**P (*e*)**	**Li (*e*)**
0.125	0.165	-0.299	1.000
0.25	-0.024	-0.373	0.969
0.375	-0.157	-0.487	0.973
0.5	-0.267	-0.618	0.968

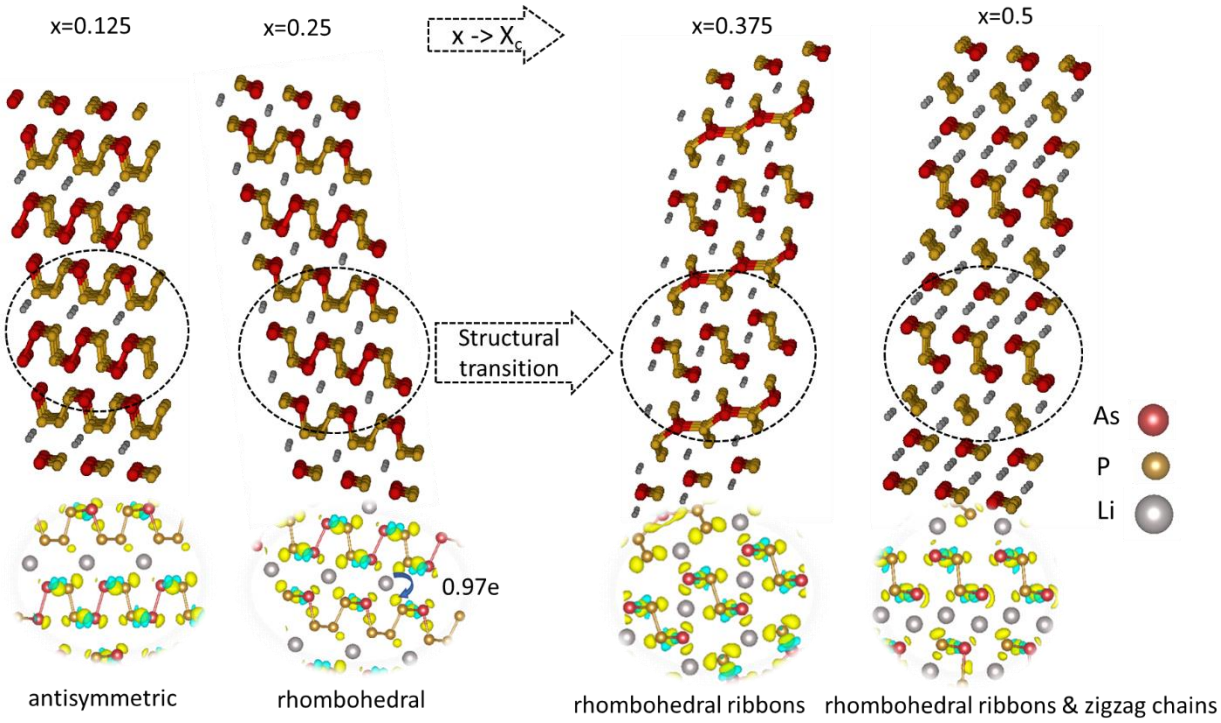

Figure 3.19: The schematic illustration of stabilized structures of b-$As_{0.375}P_{0.625}$ alloy during the Li intercalation process with different Li concentrations (x).

The successive changes in the structure were indicated by dashed-black circles. A local structural transition occurs when the Li concentration x reaches to the critical concentration X_c. The insets under each structure are the net charge redistribution (at the isosurface of $9x10^{-4}$ e/Å^3) among b-$As_{0.375}P_{0.625}$ alloy and Li atoms. The yellow/blue contours denote the electron accumulation/depletion. The blue arrow denotes ~ 0.97 e/Li transferred to b-$As_{0.375}P_{0.625}$ alloy. The red, yellow, and grey balls denote the As, P, and Li atoms, respectively.

In-depth analysis of the intercalation mechanism into b-As_yP_{1-y} reveals its promising potential as an anode material, evidenced by its higher open circuit voltage and enhanced discharge cycle performance. Moreover, the potential of b-As_yP_{1-y} in Li-ion

batteries is further supported by BP being a promising anode material for lithium ion batteries[102].

Further research is required to gain in-depth understand to the effects of lithium intercalation on the electronic structure, conductivity, and mechanical properties of the intercalated structure. In particular, this can be further advanced to investigate the strain induced by intercalating alkali metals with varying atomic radii. Such investigations can provide valuable information for modeling the relationship between the atomic diameter of the intercalant, the stress generated on the structure, and the As concentration. The knowledge gained from these studies can be leveraged to enhance existing applications.

3.3. Vibrational Properties of b-As_yP_{1-y} under high-pressure

The high-pressure experiments were conducted using a Diamond Anvil Cell (DAC) setup. The DAC (Diacell HeliosDAC Almex EasyLab) consisted of two 800μm culet diamonds, which held the sample in between, supported by a gasket and pressurized. The b-As_yP_{1-y} alloys were subjected to hydrostatic pressure using Dimethylformamide (DMF) as pressure medium in the sample chamber. The experimental procedure is described in detail in Chapter 02.

Pressure calibration inside DAC was done using the Photoluminescence spectra of the Ruby-R2 line shift (include in Chapter 02). Subsequently, the sample was loaded into the DAC, and in-situ Raman spectra were collected while applying pressure. The peak parameters of the Raman spectra were analyzed using Fityk software.

3.3.1. Computational Scheme

The computational scheme provides further insight into possible pressure-induced alterations. Credit for the first-principles calculations presented here goes to Dr. Ming Yu, Dr. Rajib Khan Musa, and Tasnim Kazi.

The structural analysis for b-As_yP_{1-y} alloys under pressure was conducted using density functional theory (DFT)[103,104] implemented in the Vienna ab initio simulation package[105], employing a plane wave basis set code. The electron-ion interaction was described using the projector augmented wave (PAW) algorithm[106], and the Perdew–Burke–Ernzerhof (PBE)[107] generalized gradient approximation (GGA) approach[108] was utilized for the exchange-correlation functional. The van der Waals interaction was taken into account using the zero damping DFT-D3 method proposed by Grimme *et. al.* [109].

To construct b-As_yP_{1-y} alloys, A 2 x 2 x 2 rectangular unit cell of black phosphorous containing 64 P atoms was initially considered. The distribution of As atoms in the alloys was optimized by randomly substituting P atoms with As atoms within the unit cell. Among the total of 64 P atoms per unit cell, there are $\frac{64!}{n!(64-n)!}$ possible configurations to substitute n P atoms with n As atoms, but many configurations can be reduced through symmetry analysis. A full structural relaxation process was then performed, without any restriction on the unit cell volume, unit cell shape, or atomic positions. To investigate the effect of the pressure on the structural evolution of b-As_yP_{1-y} alloys, a hydrostatic pressure ranging from 0 GPa to 13 GPa was applied.

3.3.2. High-pressure response of b-As_yP_{1-y}

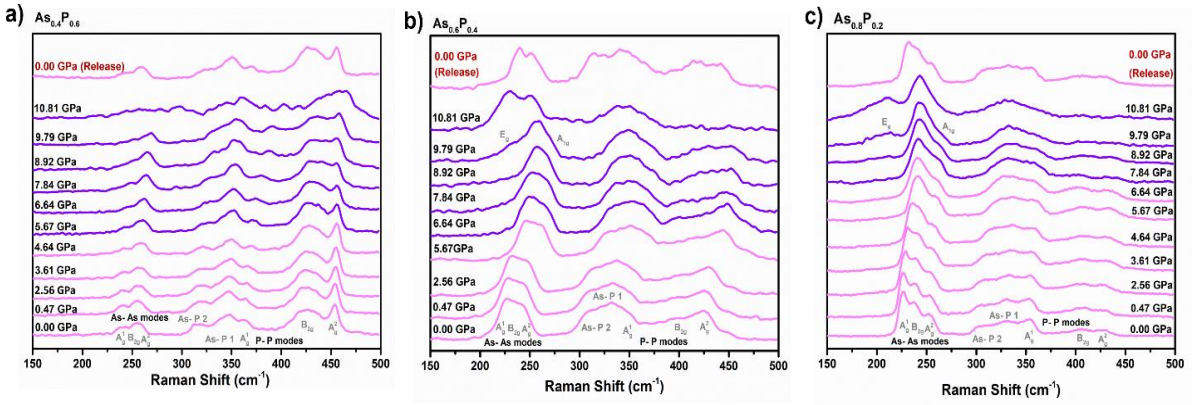

Figure 3.20: In situ Raman spectra obtained at different pressure values for three b-As_yP_{1-y} samples with y = 0.4, 0.6, and 0.8. The spectrum after the pressure was released is also shown for each sample. The spectra indicated in pink and violet correspond to pressure regions I & II, respectively.

Figure 3.20 presents the Raman spectra of all three b-As_yP_{1-y} samples under varying pressure. The spectra exhibit three main regions of peaks. In the high-frequency region (≈ 340 – 470 cm^{-1}), Raman modes associated with P-P bonds are observed and labelled as A_g^1 , B_{2g} and A_g^2 , corresponding to out-of-plane, in-plane along the zigzag direction, and in-plane along the armchair directions, respectively. Furthermore, in the low frequency region of (≈ 200 – 270 cm^{-1}), Raman modes associated with As-As bonds are observed and labelled as A_g^1, B_{2g} and A_g^2. The mid-region (≈ 300 –360 cm^{-1}) exhibits two vibrational modes associated with As-P bonds.

It has been reported that with increasing As concentration, the peak positions related to As-As modes and P-P modes systematically redshift at zero pressure. [33] As the arsenic concentration in the alloy increases, a decrease in peak intensities for P-P vibrational modes is observed, while peak intensities corresponding to As-As vibrations increase.

Under hydrostatic pressure, samples with y=0.4 and 0.6 show shifting and broadening of all peaks as the pressure increases up to 9.79 GPa. Subsequently, the spectra of each sample return to their original state when the pressure is released.

All the spectra were fitted with three peaks associated with As-As modes, three peaks associated with P-P modes, and two peaks associated with P-As modes using Lorentzian line shape analysis. As the pressure increases, the Raman spectra exhibit significant changes, such as shifting and broadening of all peaks. In general, changes of peak intensities provide evidence for a change in atomic orientations, while changes in peak positions and peak broadening provide evidence for structural compression due to pressure.

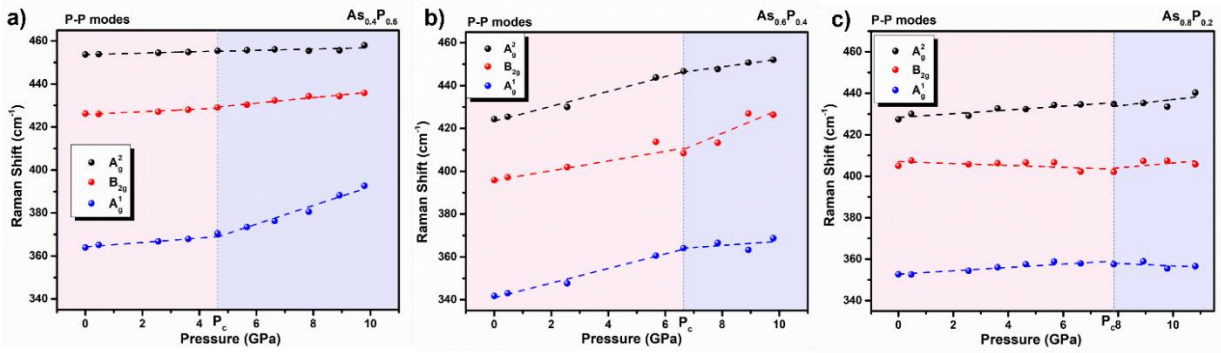

Figure 3.21: P-P peak positions versus pressure of all three b-As_yP_{1-y} samples with y=0.4 (a), y=0.6 (b), and y=0.8 (c), respectively. Dotted lines are linear fits in distinct pressure regions.

Figure 3.21 illustrates the Raman peak positions of the three P-P vibrational modes as a function of pressure for all three b-As_yP_{1-y} samples. In the case of the sample with y=0.4 (Fig. 3.20 (a)), all three peaks exhibit an overall blueshift with increasing pressure up to 9.79 GPa. The analysis of the peak shift with pressure reveals different behavior in two different pressure regions as discussed below.

In Region I (highlighted with pink), all three modes experience a linear blueshift (upshift) with increasing pressure up to a maximum applied pressure, P_c = 4.64 GPa. Subsequently, in Region II (highlighted with blue in Fig. 3.21 (a)), the modes exhibit a blueshift at varying rates within the pressure range of 4.64 - 9.79 GPa. The application of hydrostatic pressure compresses the sample from all directions, resulting in shortened bond lengths and increased vibrational energy, which is reflected as an upshift of the phonon modes in the Raman spectra. This phenomenon is referred to as "pressure induced hardening of phonon modes".

Again, in Region II, an upshift is observed for all modes with increasing pressure, albeit at a slower rate compared to the Region I. It is believed that some pressure-induced structural reorganization occurs during this phase, leading to subtle changes in the structure that result in less compression of the bond lengths. This expansion of bond lengths may indicate the temporary formation of a new local structure. Under these pressure conditions, the material transitions toward a new partially equilibrium state.

For the sample with y=0.6 (Fig. 3.21 (b)), all three peaks display an overall blueshift with increasing pressure up to 9.79 GPa. Similar to the previous sample, the Raman modes exhibit distinct behaviors in two pressure regions. In Region I, all three modes undergo a linear upshift with increasing pressure up to a maximum applied pressure, P_c = 6.64 GPa. This is followed by a linear blueshift at a different rate in Region II, as observed in Fig. 3.21 (b), within the pressure rang of 6.64 - 9.79 GPa.

However, the sample withy=0.8 (Fig. 3.21 (c)) exhibits somewhat different characteristics within the accessible pressure range. A linear upshift is observed for the A^1_g and A^2_g modes, while the B_{2g} mode shows almost no shift with increasing pressure up to a

maximum applied pressure, P_c = 7.84 GPa (Region I). Subsequently, for pressures greater than 7.84 GPa, the modes show an upshift (or weak dependence) at a different rate compared to the Region I.

The y dependence of P_c on y is shown in Figure 3.22.

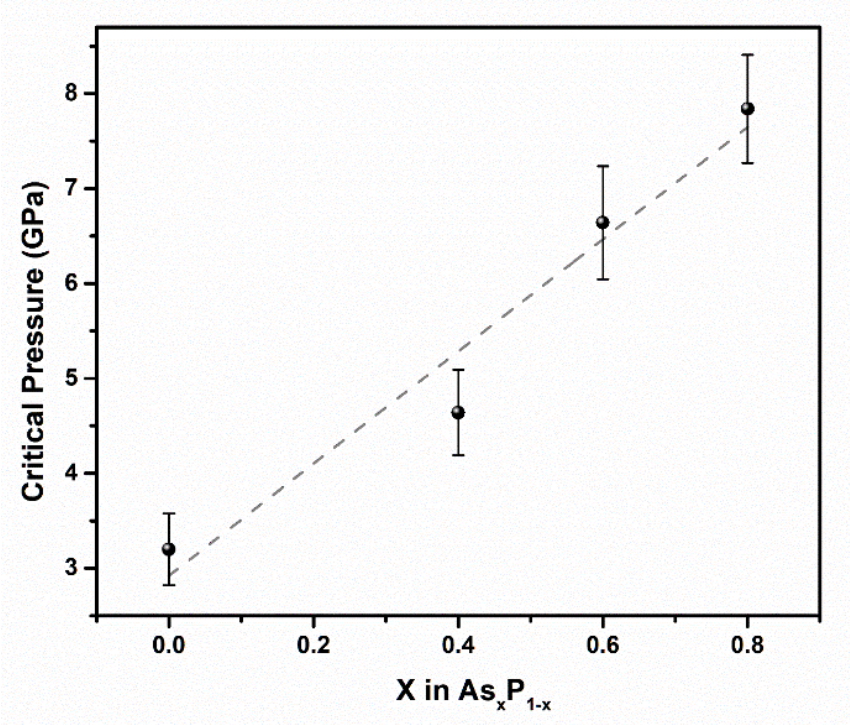

Figure 3.22: The As concentration, y (in As_yP_{1-y}) dependance of the critical pressure, Pc.

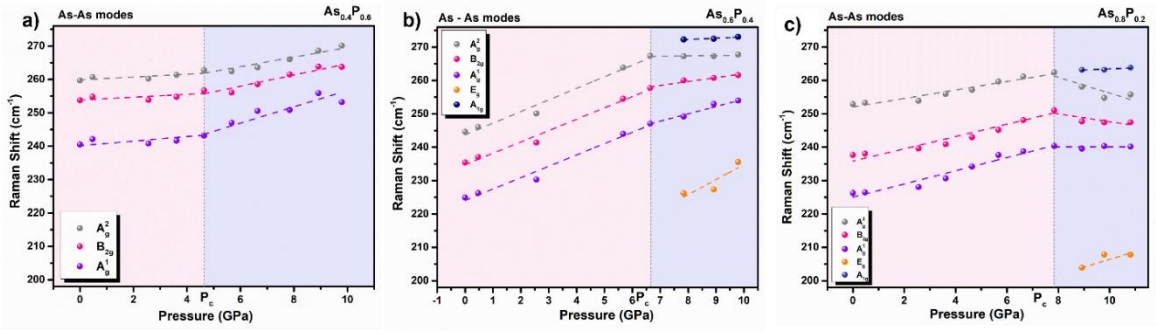

Figure 3.23: As-As peak positions versus pressure profiles of all three b-As_yP_{1-y} samples with y=0.4 (a), y=0.6 (b), and y=0.8 (c), respectively. Dotted lines are linear fits in two distinct pressure regions. The peak positions of the new modes (identified as segregated gray As) emerged, in samples with higher As concentrations (y= 0.6 and 0.8) are shown in orange and dark blue.

Figure 3.23 illustrates the Raman peak positions of the three As-As vibrational modes as a function of pressure for the three b-As_yP_{1-y} samples. All three peaks for the samples with y=0.4 and 0.6 exhibit an overall blueshift with increasing pressure, but at different rates within the two regions. In the case of the sample with y=0.6, new peaks identified as the E_g mode and A_{1g} mode of g-As emerge in Region II and undergo an upshift with increasing pressure. Interestingly, for the sample with y=0.8, all the peaks show a redshift in the second region. The E_g and A_{1g} modes appear to emerge in the second pressure region of this sample and undergo a blueshift as the pressure continues to increase.

It is believed that that a small amount of rhombohedral g-As segregates from orthorhombic b-As_yP_{1-y} in the samples with y=0.6 and 0.8 after surpassing a threshold pressure value in each sample. The downward shifting of the Raman modes in Region II can be interpreted as the elongation of the As-As bonds of the b-As_yP_{1-y} phase at or near the grain boundary with the g-As phase, which undergoes compressive structural changes. The Raman spectra were found to recover upon the release of the pressure for all three samples.

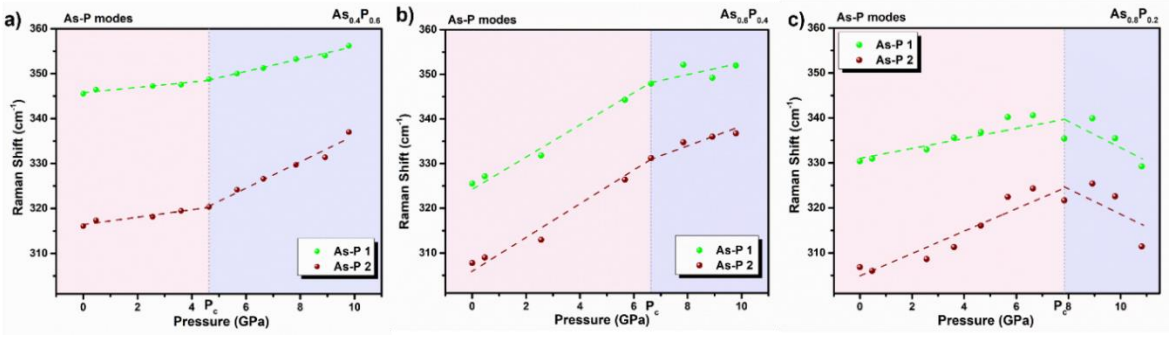

Figure 3.24: As-P peak positions versus pressure of all three b-As_yP_{1-y} samples with y = 0.4 (a), y = 0.6 (b), and y = 0.8 (c), respectively. Dotted lines are linear fits in distinct pressure regions.

Fig. 3.24 shows the Raman peak positions of the two As-P vibrational modes as a function of pressure for the three b-As_yP_{1-y} samples. All three peaks for the samples with y=0.4 and 0.6 show an overall blueshift with increasing pressure at different rates within the two regions. However, the sample with y=0.8, both peaks show a red shift in the second region. Again, this is consistent with the elongation of the As-P bonds of the b-As_yP_{1-y} phase at or near the grain boundary with the g-As phase which undergoes compressive structural changes.

To understand the different Raman characteristics in two different pressure regimes (Regions I and II), we analyzed the lattice constants, volume, and bond lengths (including armchair and zigzag bonds) under pressure using our DFT results. According to our DFT calculations, bond lengths along the armchair direction monotonically decrease with pressure by approximately 0.03-0.05 Å, as shown in the top panel of Figure 3.25. This indicates a hardening of phonon modes, which is consistent with the experimental observation of an upshift in Raman A_g^2 modes.

However, by comparing the structural parameters (refer to Figure 3.25), we found that the dominant changes in bond lengths and the lattice constants under pressure mainly occur along the zigzag direction. As depicted in the bottom panel of Figure 3.25, the bond lengths along the zigzag direction initially remain unchanged or slowly decrease with pressure in the first regime, and then abruptly extend to larger values by approximately 0.2-0.4 Å in the second regime. The transition point is observed to depend on the As concentration. These changes in bond lengths along the zigzag direction suggest a local structural change from cis-like to trans-like bonding under pressure.

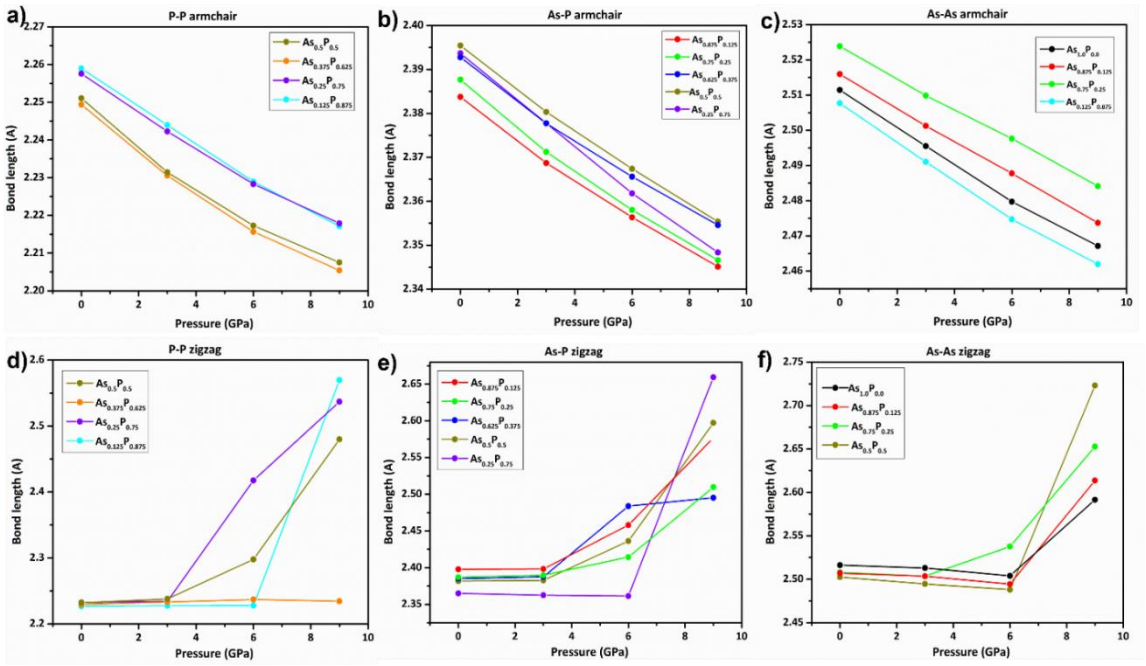

Figure 3.25: P-P, As-P, and As-As bond lengths of b-As_yP_{1-y} alloys under pressure. Top panel (a-c) indicates P-P, As-P and As-As bonds along the armchair direction and bottom panel (d-f) along zigzag direction, respectively.

The increase in bond lengths along the zigzag in the second regime leads to a softening of vibration modes, which is consistent with the redshift of As-As and As-P modes of the sample with the highest As concentration (y=0.8). It is possible that the presence of the g-As phase, which undergoes compressive structural changes, in close proximity to the b-As_yP_{1-y} phase may also influence the As bonds.

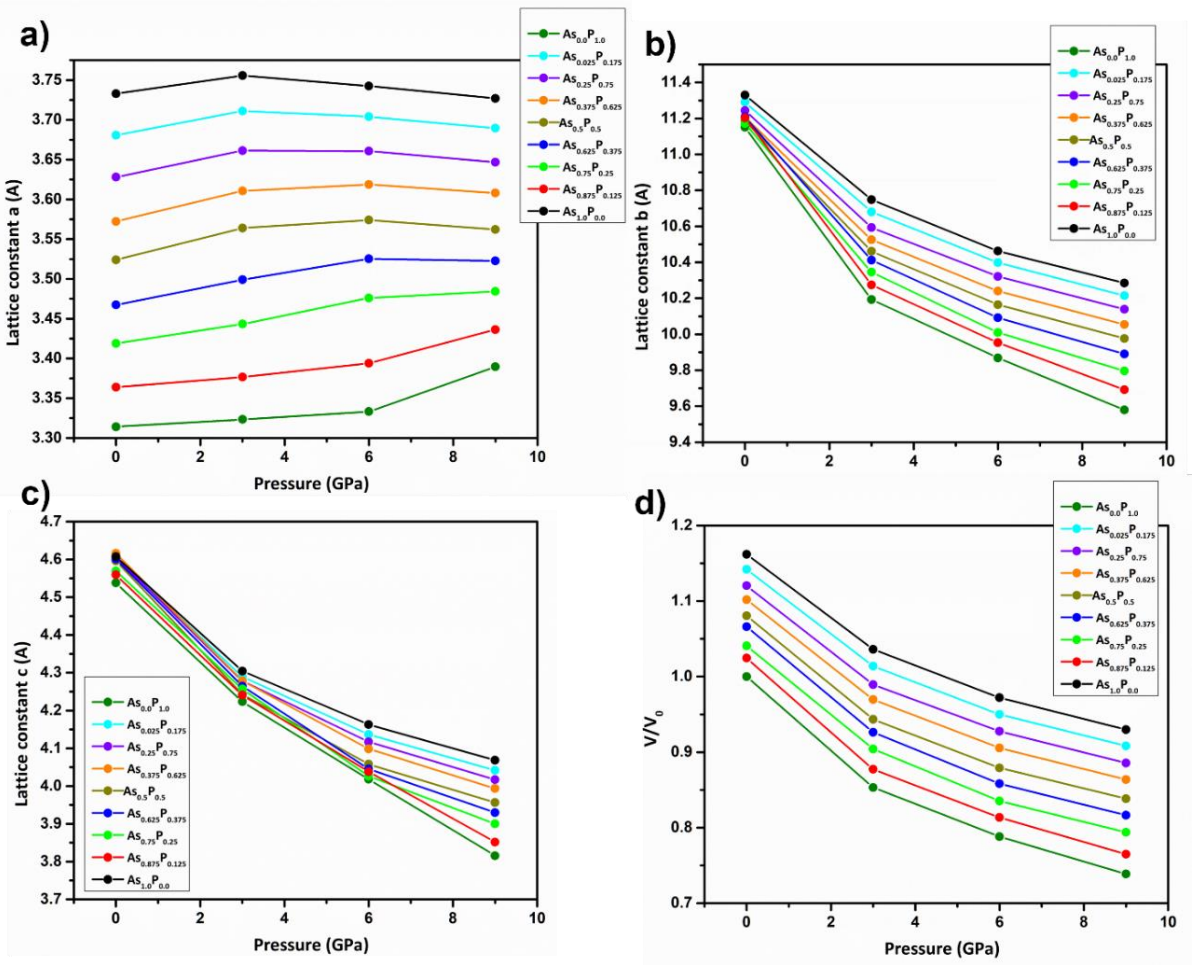

Figure 3.26: The lattice constants along the zigzag (a), vertical (b), and armchair (c) directions of b-As_yP_{1-y} alloys under the pressure. (d) the ration of the volume V of b-As_yP_{1-y} alloys under the pressure, where V_0 is the volume of BP under zero pressure.

CHAPTER 4
CONCLUSIONS

Extensive research has been conducted on 2D materials over time. The particular focus has been on strain engineering, due to its potential to induce phase transitions and structural transformations, leading to the emergence of new functionalities and applications. This study focused on examining the effects of strain on the b-As_yP_{1-y} alloys, which are classified as 2D materials, utilizing intercalation and high-pressure techniques. Intercalation serves as a highly versatile technique, capable of modifying interlayer interactions, introducing dopants into 2D materials, altering their electronic structure, and even transforming them into entirely distinct structures or phases. Owing to its versatility, intercalation has employed across diverse technologies, serving as a critical tool for controlling the properties of layered materials, facilitating their transition across phase diagrams, and triggering significant structural transformations[48]. On the other hand, high-pressure technology is extensively employed in materials science to amplify the electronic and atomic structure of materials, thereby adjusting diverse material properties as well. By subjecting materials to high-pressure conditions, the inter-atomic volume can be drastically reduced, leading to notable densification effects or an amplification in reactivity. This project includes thorough investigation of the impact of intercalation and high-pressure on the lattice structure of b-As_yP_{1-y} alloys.

The vibrational properties of BP are of significant importance, particularly considering the similarity of its properties to the b-As_yP_{1-y} alloys under investigation. The in-situ Raman spectra revealed a redshift in all three Raman vibrational modes (phonon modes) with increasing degrees of lithiation. This redshift can be attributed to a decrease in vibrational energy (frequency) between the P atoms, resulting from the stretching and weakening of intralayer and interlayer bonds upon insertion of guest species into the BP structure.

Furthermore, XRD analysis confirmed that intercalation did not induce a phase change, as evidenced by the absence of peak shifts or the appearance of new peaks in the XRD patterns. However, a significant reduction in intensity of (0k0) reflections indicated a decrease in thickness of coherently bonded BP flakes upon lithiation. This reduction can be attributed to the partial effective exfoliation of BP flakes, as the insertion of Li weakens or breaks interlayer van der Waals bonds along the out-of-plane direction. The intercalation process exhibits high in-plane anisotropy, with the channels along the ZZ direction found to be the preferred pathway for Li intercalation due to their lower energy profile compared to the AM direction. Interestingly, this result deviates from the theoretical prediction of the transition to the blue phosphorene phase induced by Li intercalation, indicating a discrepancy between the experimental findings and the theoretical expectations.

Stimulated by the potential insights gained from investigating the behavior of BP, the scope of this study was extended to a series of b-As_yP_{1-y} alloys. The specific alloys focused on in this study were $As_{0.4}P_{0.6}$, $As_{0.5}P_{0.5}$, $As_{0.6}P_{0.4}$, and $As_{0.8}P_{0.2}$. Raman spectroscopy analysis revealed the presence of three distinct atomic vibrational (phonon) modes originating from As-As bonding, As-P bonding, and P-P bonding. The P-P bonds exhibited A^1_g, B_{2g}, and A^2_g Raman modes, corresponding to out-of-plane, in-plane along

the zig-zag direction, and in-plane along the armchair direction, respectively, within the frequency range of 350-470 cm^{-1}. Similarly, the A^1_g, B_{2g}, and A^2_g phonon modes attributed to As-As bonds were identified in the lower frequency region ranging from 200-270 cm^{-1}. Additionally, two phonon modes arising from As-P bonds were observed in the intermediate frequency range of 270-350 cm^{-1}. Notably, all these phonon modes exhibited a redshift with increasing As concentration, resulting from changes in bond strengths and bond lengths as P atoms were progressively substituted by As atoms. Furthermore, a comparative increase in the peak intensities of As-As vibrations and a decrement in P-P peak intensities were observed with increasing As concentration. This observation can be attributed to the increasing prominence of As-As vibrations and the decreasing prominence of P-P vibrations as more P atoms were replaced by As atoms within the lattice structure.

Additional characterization using X-ray diffraction (XRD) patterns, in conjunction with transmission electron microscopy (TEM) data, revealed a systematic expansion of the lattice structure with increasing As concentration (y). This As-dependent increase in unit cell parameters was attributed to a slight outward displacement of the primitive unit cell, as the atomic diameter of As is larger than that of P. Therefore, the lattice structure expansion becomes more pronounced as the As concentration increases. Moreover, the XRD results further confirmed that the b-As_yP_{1-y} alloys possess an orthorhombic puckered structure analogous to BP.

The gray arsenic (As) exhibits three Raman active modes, namely, two-fold degenerate E_g modes and one A_{1g} mode. The E_g modes correspond to the in-plane vibrational mode, while the A_{1g} mode pertains to the out-of-plane vibrational mode, which manifests as two distinct Raman peaks observed at approximately 193 cm^{-1} and 253 cm^{-1}.

X-ray diffraction (XRD) analysis confirmed the crystal structure of gray As to be rhombohedral, belonging to the R3m space group. Notably, theoretical calculations suggest that the coexistence of rhombohedral (gray As) and orthorhombic (b-As) phases in b-As_yP_{1-y} alloys is energetically favorable.

Electrochemical Li intercalation of b-As_yP_{1-y} alloys was studied *in-situ* using Raman spectroscopy. At the outset, intercalation dependent alternations in eight vibrational modes identified in b-As_yP_{1-y} in Raman spectra were tracked. During the initial stages of the intercalation process, all modes of all the samples showed a downshift due to donor-type charge transfer causing softening of phonon modes. Above a composition-dependent intercalation threshold, two new peaks emerged identified as the E_g and A_{1g} modes of g-As indicating an intercalation-driven structural phase segregation process. Above the intercalation threshold, all the peaks showed an upshift due to the strain imparted (and bond shortening) on the b-As_yP_{1-y} phase by the segregated (and also strained) g-As phase. Our computational modeling revealed the co-existence of g-As in the As_yP_{1-y} alloys with high As concentrations due to thermodynamic instability and also a local atomic structural transition taking place at a critical Li concentration during the intercalation process.

Further reinforcing evidence to intercalation driven lattice expansions incorporated with phase segregation, XRD patterns indicate a downshift in 2θ values.

A new peak (2θ = 32.5°) adjacent to the (040) peak of orthorhombic structure appears to emerge after Li-intercalation. The rhombohedral gray As also demonstrates a peak associated with (012) around 2θ =32.5°. This can be attributed to a local structural change of at least part of the sample from orthorhombic to rhombohedral due to Li intercalation. However, the sample with highest As concentration (y = 0.8), exhibits such features even

in the pristine state (prior to the intercalation). This is consistent with the Raman results confirming potential structural segregation due to the increased As concentration causing part of the sample to undergo such structural change.

Then with the knowledge of induced structural segregation caused by Li intercalation in b-As_yP_{1-y}, it's interesting to experiment its response under of high-pressure conditions. The Diamond Anvil Cell is utilized to apply high-pressure conditions and observed alternations of vibrational modes by in-situ Raman spectra. Notably, the peak shifting of the phonon mode is a useful tool for analyzing the strain behavior of two-dimensional materials. Our previous work on BP under high-pressure demonstrated an overall blueshift of the Raman modes, due to increase in atomic vibrational energy of the structure, caused by the triaxial stress generated by the hydrostatic pressure. While out-of-plane mode of the pristine BP was found to be blue shifting monotonically with increasing pressure, the two in-plane modes of the pristine BP were found to be responding differently in three different pressure regions. In detail, a blue shift (0-3.2 GPa), followed by a red shift (3.2-5.2 GPa) and then again, a blue shift (>5.2 GPa) was observed in in-plane modes. The cause of downshift in the mid pressure region can be a result of pressure-induced reorganization in the lattice structure.

Then, the structural evolution of black arsenic-phosphorous (b-As_yP_{1-y}) alloys with varying arsenic concentrations were studied under hydrostatic pressure using in-situ Raman spectroscopy. Significant pressure-induced shifts were observed in all vibrational modes corresponding to P-P bonds (A^1_g, A^2_g, B_{2g}), As-As bonds (A^1_g, A^2_g, B_{2g}), and As-P bonds for different As concentrations.

For alloys with lower As concentrations, a regime (Region I) characterized by a monotonic upshift of all modes was observed, indicating phonon hardening due to hydrostatic pressure. In a second regime (Region II), a linear blueshift (or negligible change in some modes) at a reduced rate with pressure was observed, suggesting local structural reorganization in the samples and less compression of bond lengths.

The accessible pressure ranges are categorized into two regions, namely Region I and Region II, based on the distinctive characteristics exhibited by phonon modes in each composition. The alloy with a higher As concentration also exhibited two distinct regimes within the accessible pressure limit. In Region I, there was a blueshift of all modes, while in Region II, a downward shift of As-As, and As-P Raman modes (and some P-P modes) was observed. Interestingly, the emergence of new peaks identified as the E_g mode and A_{1g} modes of the g-As phase was observed in this pressure range, indicating compressive strain. These anomalous changes in Region II confirmed the formation of a new local structure, interpreted as the elongation of the P-P, As-As, and As-P bonds along the zigzag direction in the b-As_yP_{1-y} phase at or near the grain boundary with the emergence of the g-As phase undergoing compressive structural changes.

Future work

The current work on intercalation and high-pressure studies on b-As_yP_{1-y} paves the way to new insights and research interests. The formation of new local structure in b-As_yP_{1-y} implies some potential of phase transition, which is possible to result in material with starkly different properties. Most interestingly, our research group revealed that b-$As_{0.2}P_{0.8}$

alloy exhibit extremely high thermopower of 803 μV/K at room temperature and a metallic behavior with negligible thermopower for higher As concentrations as of $As_{0.83}P_{0.17}$ and As_1P_0. Furthermore, 4-probe resistance was reported to be decreasing 3 times compared to BP, with the increase of As content of b-As_yP_{1-y} alloys from y = 0 to 1. All these interesting discoveries revealed that black arsenic phosphorus is an excellent thermoelectric material for thermoelectric devices.

In addition, the degradation study performed by our group include investigating the effects of oxygen and humidity on BP and b-As_yP_{1-y} alloys. It reported that b-As_yP_{1-y} ($y<0.83$) is more stable than BP. The Raman spectroscopic data reveal that P-P peak intensities degrade upon exposure to oxygen and moisture. After being exposed to ambient conditions, it was determined that the normalized thermos electric power (TEP) and four-probe resistance of b-As_yP_{1-y} were relatively stable compared to BP. This was attributed to the charge transfer between the oxygen redox potential of air and the Fermi energy (EF) of the semiconductors.

It is intriguing to identify and understand a trend between this factor and the size of intercalant atoms. Li has a small atomic radius of 0.182 nm and Na has intermediate atomic radius of 0.19nm. Therefore, accommodating an intercalant like Na, has a potential to enhance the effect of intercalation on the crystal structure. Our group is currently working on Na intercalation into b-As_yP_{1-y} and has reported an interesting preliminary result of formation of nano ribbons. Using different sizes of intercalants could assist to obtain systematic understanding of intercalation induced strain generated on b-As_yP_{1-y} structure. It could use to predict relative strain and composition dependent responses of each. Moreover, it would rather be interesting to investigate the synergistic effect of intercalation

and high-pressure in b-As_yP_{1-y} alloys, which may lead to outcomes and applications beyond imagination.

REFERENCES

1. Shanmugam, V.; Mensah, R. A.; Babu, K.; Gawusu, S.; Chanda, A.; Tu, Y.; Neisiany, R. E.; Försth, M.; Sas, G.; Das, O., A Review of the Synthesis, Properties, and Applications of 2D Materials. *Particle & Particle Systems Characterization* **2022,** *39* (6), 2200031.
2. Irshad, R.; Tahir, K.; Li, B.; Sher, Z.; Ali, J.; Nazir, S., A revival of 2D materials, phosphorene: Its application as sensors. *Journal of Industrial and Engineering Chemistry* **2018,** *64*, 60-69.
3. Kang, S.; Lee, D.; Kim, J.; Capasso, A.; Kang, H. S.; Park, J.-W.; Lee, C.-H.; Lee, G.-H., 2D semiconducting materials for electronic and optoelectronic applications: potential and challenge. *2D Materials* **2020,** *7* (2), 022003.
4. Glavin, N. R.; Muratore, C.; Snure, M., Toward 2D materials for flexible electronics: opportunities and outlook. *Oxford Open Materials Science* **2021,** *1* (1), itaa002.
5. Wang, Q. H.; Kalantar-Zadeh, K.; Kis, A.; Coleman, J. N.; Strano, M. S., Electronics and optoelectronics of two-dimensional transition metal dichalcogenides. *Nature nanotechnology* **2012,** *7* (11), 699-712.
6. Grigorenko, A. N.; Polini, M.; Novoselov, K., Graphene plasmonics. *Nature photonics* **2012,** *6* (11), 749-758.
7. Chen, D.; Tang, L.; Li, J., Graphene-based materials in electrochemistry. *Chemical Society Reviews* **2010,** *39* (8), 3157-3180.
8. Rajapakse, M. C., Intercalation and high pressure studies of black phosphorous-pathways to novel materials and physics. **2021**.
9. Raccichini, R.; Varzi, A.; Passerini, S.; Scrosati, B., The role of graphene for electrochemical energy storage. *Nature materials* **2015,** *14* (3), 271-279.
10. Bae, S.; Kim, H.; Lee, Y.; Xu, X.; Park, J.-S.; Zheng, Y.; Balakrishnan, J.; Lei, T.; Ri Kim, H.; Song, Y. I., Roll-to-roll production of 30-inch graphene films for transparent electrodes. *Nature nanotechnology* **2010,** *5* (8), 574-578.
11. Ge, J.-F.; Liu, Z.-L.; Liu, C.; Gao, C.-L.; Qian, D.; Xue, Q.-K.; Liu, Y.; Jia, J.-F., Superconductivity above 100 K in single-layer FeSe films on doped SrTiO 3. *Nature materials* **2015,** *14* (3), 285-289.
12. Deng, D.; Novoselov, K.; Fu, Q.; Zheng, N.; Tian, Z.; Bao, X., Catalysis with two-dimensional materials and their heterostructures. *Nature nanotechnology* **2016,** *11* (3), 218-230.
13. Chen, J.; Wu, X. J.; Yin, L.; Li, B.; Hong, X.; Fan, Z.; Chen, B.; Xue, C.; Zhang, H., One-pot synthesis of CdS nanocrystals hybridized with single-layer transition-

metal dichalcogenide nanosheets for efficient photocatalytic hydrogen evolution. *Angewandte Chemie* **2015,** *127* (4), 1226-1230.
14. Qiu, M.; Ren, W. X.; Jeong, T.; Won, M.; Park, G. Y.; Sang, D. K.; Liu, L.-P.; Zhang, H.; Kim, J. S., Omnipotent phosphorene: a next-generation, two-dimensional nanoplatform for multidisciplinary biomedical applications. *Chemical Society Reviews* **2018,** *47* (15), 5588-5601.
15. Roy, S.; Zhang, X.; Puthirath, A. B.; Meiyazhagan, A.; Bhattacharyya, S.; Rahman, M. M.; Babu, G.; Susarla, S.; Saju, S. K.; Tran, M. K., Structure, properties and applications of two-dimensional hexagonal boron nitride. *Advanced Materials* **2021,** *33* (44), 2101589.
16. Zhang, K.; Feng, Y.; Wang, F.; Yang, Z.; Wang, J., Two dimensional hexagonal boron nitride (2D-hBN): synthesis, properties and applications. *Journal of Materials Chemistry C* **2017,** *5* (46), 11992-12022.
17. Teshome, T.; Datta, A., Effect of doping in controlling the structure, reactivity, and electronic properties of pristine and Ca (II)-intercalated layered silicene. *The Journal of Physical Chemistry C* **2017,** *121* (28), 15169-15180.
18. Jamdagni, P.; Kumar, A.; Sharma, M.; Thakur, A.; Ahluwalia, P., Electronic properties and STM images of vacancy clusters and chains in functionalized silicene and germanene. *Physica E: Low-dimensional Systems and Nanostructures* **2017,** *85*, 65-73.
19. Zhu, X.; Liu, B.; Hou, H.; Huang, Z.; Zeinu, K. M.; Huang, L.; Yuan, X.; Guo, D.; Hu, J.; Yang, J., Alkaline intercalation of Ti3C2 MXene for simultaneous electrochemical detection of Cd (II), Pb (II), Cu (II) and Hg (II). *Electrochimica Acta* **2017,** *248*, 46-57.
20. Jung, Y.; Zhou, Y.; Cha, J. J., Intercalation in two-dimensional transition metal chalcogenides. *Inorganic Chemistry Frontiers* **2016,** *3* (4), 452-463.
21. Warschauer, D., Electrical and optical properties of crystalline black phosphorus. *Journal of Applied Physics* **1963,** *34* (7), 1853-1860.
22. Zhang, X.; Xie, H.; Liu, Z.; Tan, C.; Luo, Z.; Li, H.; Lin, J.; Sun, L.; Chen, W.; Xu, Z., Black phosphorus quantum dots. *Angewandte chemie international edition* **2015,** *54* (12), 3653-3657.
23. Qiao, J.; Kong, X.; Hu, Z.-X.; Yang, F.; Ji, W., High-mobility transport anisotropy and linear dichroism in few-layer black phosphorus. *Nature communications* **2014,** *5* (1), 1-7.
24. Morita, A.; Sasaki, T., Electron-phonon interaction and anisotropic mobility in black phosphorus. *Journal of the Physical Society of Japan* **1989,** *58* (5), 1694-1704.
25. Liu, H.; Du, Y.; Deng, Y.; Peide, D. Y., Semiconducting black phosphorus: synthesis, transport properties and electronic applications. *Chemical Society Reviews* **2015,** *44* (9), 2732-2743.
26. Liu, H.; Neal, A. T.; Zhu, Z.; Luo, Z.; Xu, X.; Tománek, D.; Ye, P. D., Phosphorene: an unexplored 2D semiconductor with a high hole mobility. *ACS nano* **2014,** *8* (4), 4033-4041.
27. Abu, U. O.; Vithanage, D.; Vitharana, A.; Jasinski, J. B.; Sumanasekera, G., Degradation Studies of Air-Exposed Black Phosphorous and Black Arsenic Phosphorous. *ChemEngineering* **2023,** *7* (2), 18.

28. Chen, Y.; Chen, C.; Kealhofer, R.; Liu, H.; Yuan, Z.; Jiang, L.; Suh, J.; Park, J.; Ko, C.; Choe, H. S., Black arsenic: a layered semiconductor with extreme in-plane anisotropy. *Advanced materials* **2018,** *30* (30), 1800754.
29. Wang, C.; Xia, Q.; Nie, Y.; Rahman, M.; Guo, G., Strain engineering band gap, effective mass and anisotropic Dirac-like cone in monolayer arsenene. *AIP Advances* **2016,** *6* (3), 035204.
30. Sun, J.; Lin, N.; Ren, H.; Tang, C.; Yang, L.; Zhao, X., The electronic structure, mechanical flexibility and carrier mobility of black arsenic–phosphorus monolayers: a first principles study. *Physical Chemistry Chemical Physics* **2016,** *18* (14), 9779-9787.
31. Yu, L.; Zhu, Z.; Gao, A.; Wang, J.; Miao, F.; Shi, Y.; Wang, X., Electrically tunable optical properties of few-layer black arsenic phosphorus. *Nanotechnology* **2018,** *29* (48), 484001.
32. Sun, Y.; Shuai, Z.; Wang, D., Lattice thermal conductivity of monolayer AsP from first-principles molecular dynamics. *Physical Chemistry Chemical Physics* **2018,** *20* (20), 14024-14030.
33. Karki, B.; Rajapakse, M.; Sumanasekera, G. U.; Jasinski, J. B., Structural and Thermoelectric Properties of Black Arsenic–Phosphorus. *ACS Applied Energy Materials* **2020,** *3* (9), 8543-8551.
34. Shi, X.; Wang, T.; Wang, J.; Xu, Y.; Yang, Z.; Yu, Q.; Wu, J.; Zhang, K.; Zhou, P., Synthesis of black arsenic-phosphorus and its application for Er-doped fiber ultrashort laser generation. *Optical Materials Express* **2019,** *9* (5), 2348-2357.
35. Liu, Y.; Wang, H.; Wang, S.; Wang, Y.; Wang, Y.; Guo, Z.; Xiao, S.; Yao, Y.; Song, Q.; Zhang, H., Highly efficient silicon photonic microheater based on black arsenic–phosphorus. *Advanced Optical Materials* **2020,** *8* (6), 1901526.
36. Luxa, J.; Bouša, D.; Zoller, F.; Fattakhova-Rohlfing, D.; Sofer, Z., Black phosphorus–arsenic alloys for lithium ion batteries. *FlatChem* **2020,** *19*, 100143.
37. Long, M.; Gao, A.; Wang, P.; Xia, H.; Ott, C.; Pan, C.; Fu, Y.; Liu, E.; Chen, X.; Lu, W.; Nilges, T.; Xu, J.; Wang, X.; Hu, W.; Miao, F., Room temperature high-detectivity mid-infrared photodetectors based on black arsenic phosphorus. *Science Advances* **2017,** *3* (6), e1700589.
38. Yuan, S.; Shen, C.; Deng, B.; Chen, X.; Guo, Q.; Ma, Y.; Abbas, A.; Liu, B.; Haiges, R.; Ott, C., Air-stable room-temperature mid-infrared photodetectors based on hBN/black arsenic phosphorus/hBN heterostructures. *Nano letters* **2018,** *18* (5), 3172-3179.
39. Liu, B.; Köpf, M.; Abbas, A. N.; Wang, X.; Guo, Q.; Jia, Y.; Xia, F.; Weihrich, R.; Bachhuber, F.; Pielnhofer, F., Black arsenic–phosphorus: layered anisotropic infrared semiconductors with highly tunable compositions and properties. *Advanced Materials* **2015,** *27* (30), 4423-4429.
40. Shu, Y.; Guo, J.; Fan, T.; Xu, Y.; Guo, P.; Wang, Z.; Wu, L.; Ge, Y.; Lin, Z.; Ma, D., Two-dimensional black arsenic phosphorus for ultrafast photonics in near-and mid-infrared regimes. *ACS Applied Materials & Interfaces* **2020,** *12* (41), 46509-46518.
41. Xie, M.; Zhang, S.; Cai, B.; Huang, Y.; Zou, Y.; Guo, B.; Gu, Y.; Zeng, H., A promising two-dimensional solar cell donor: Black arsenic–phosphorus monolayer with 1.54 eV direct bandgap and mobility exceeding 14,000 cm2 V− 1 s− 1. *Nano Energy* **2016,** *28*, 433-439.

42. Liang, J.; Hu, Y.; Zhang, K.; Wang, Y.; Song, X.; Tao, A.; Liu, Y.; Jin, Z., 2D layered black arsenic-phosphorus materials: Synthesis, properties, and device applications. *Nano Research* **2021**, 1-16.
43. Pumera, M.; Sofer, Z., 2D monoelemental arsenene, antimonene, and bismuthene: beyond black phosphorus. *Advanced Materials* **2017,** *29* (21), 1605299.
44. Zhu, Z.; Tománek, D., Semiconducting layered blue phosphorus: a computational study. *Physical review letters* **2014,** *112* (17), 176802.
45. Xu, Y.; Shi, Z.; Shi, X.; Zhang, K.; Zhang, H., Recent progress in black phosphorus and black-phosphorus-analogue materials: properties, synthesis and applications. *Nanoscale* **2019,** *11* (31), 14491-14527.
46. Shojaei, F.; Kang, H. S., Electronic structure and carrier mobility of two-dimensional α arsenic phosphide. *The Journal of Physical Chemistry C* **2015,** *119* (34), 20210-20216.
47. Shi, J.; Chen, L.-Q., Strain Engineering in Functional Materials. AIP Publishing LLC: 2019; Vol. 125, p 082201.
48. Rajapakse, M.; Karki, B.; Abu, U. O.; Pishgar, S.; Musa, M. R. K.; Riyadh, S. S.; Yu, M.; Sumanasekera, G.; Jasinski, J. B., Intercalation as a versatile tool for fabrication, property tuning, and phase transitions in 2D materials. *npj 2D Materials and Applications* **2021,** *5* (1), 1-21.
49. Stark, M. S.; Kuntz, K. L.; Martens, S. J.; Warren, S. C., Intercalation of layered materials from bulk to 2D. *Advanced Materials* **2019,** *31* (27), 1808213.
50. Dresselhaus, M. S.; Dresselhaus, G., Intercalation compounds of graphite. *Advances in physics* **2002,** *51* (1), 1-186.
51. Pruvost, S.; Berger, P.; Hérold, C.; Lagrange, P., Nuclear microanalysis: An efficient tool to study intercalation compounds containing lithium. *Carbon* **2004,** *42* (10), 2049-2056.
52. Bissessur, R.; Scully, S. F., Intercalation of solid polymer electrolytes into graphite oxide. *Solid State Ionics* **2007,** *178* (11-12), 877-882.
53. Zhou, D.; Liu, R.; He, Y. B.; Li, F.; Liu, M.; Li, B.; Yang, Q. H.; Cai, Q.; Kang, F., SiO2 hollow nanosphere-based composite solid electrolyte for lithium metal batteries to suppress lithium dendrite growth and enhance cycle life. *Advanced Energy Materials* **2016,** *6* (7), 1502214.
54. Rajapakse, M.; Musa, R.; Abu, U. O.; Karki, B.; Yu, M.; Sumanasekera, G.; Jasinski, J. B., Electrochemical Li Intercalation in Black Phosphorus: In Situ and Ex Situ Studies. *The Journal of Physical Chemistry C* **2020,** *124* (19), 10710-10718.
55. Xu, K., Nonaqueous liquid electrolytes for lithium-based rechargeable batteries. *Chemical reviews* **2004,** *104* (10), 4303-4418.
56. Zheng, H.; Jiang, K.; Abe, T.; Ogumi, Z., Electrochemical intercalation of lithium into a natural graphite anode in quaternary ammonium-based ionic liquid electrolytes. *Carbon* **2006,** *44* (2), 203-210.
57. Wan, J.; Lacey, S. D.; Dai, J.; Bao, W.; Fuhrer, M. S.; Hu, L., Tuning two-dimensional nanomaterials by intercalation: materials, properties and applications. *Chemical Society Reviews* **2016,** *45* (24), 6742-6765.
58. Li, X.-L.; Li, Y.-D., MoS2 nanostructures: synthesis and electrochemical Mg2+ intercalation. *The Journal of Physical Chemistry B* **2004,** *108* (37), 13893-13900.

59. Sun, L.-Q.; Li, M.-J.; Sun, K.; Yu, S.-H.; Wang, R.-S.; Xie, H.-M., Electrochemical activity of black phosphorus as an anode material for lithium-ion batteries. *The Journal of Physical Chemistry C* **2012,** *116* (28), 14772-14779.
60. Morales, J.; Santos, J.; Tirado, J., Electrochemical studies of lithium and sodium intercalation in MoSe2. *Solid State Ionics* **1996,** *83* (1-2), 57-64.
61. Shokhen, V.; Zitoun, D., Electrochemical intercalation of sodium in vertically aligned molybdenum disulfide for hydrogen evolution reaction. *FlatChem* **2019,** *14*, 100086.
62. Shioyama, H.; Fujii, R., Electrochemical reactions of stage 1 sulfuric acid—graphite intercalation compound. *Carbon* **1987,** *25* (6), 771-774.
63. Zhang, R.; Waters, J.; Geim, A. K.; Grigorieva, I. V., Intercalant-independent transition temperature in superconducting black phosphorus. *Nature communications* **2017,** *8* (1), 1-7.
64. Maruyama, Y.; Suzuki, S.; Osaki, T.; Yamaguchi, H.; Sakai, S.; Nagasato, K.; Shirotani, I., Electronic properties of black phosphorus single crystals and intercalation compounds. *Bulletin of the Chemical Society of Japan* **1986,** *59* (4), 1067-1071.
65. Xia, W.; Zhang, Q.; Xu, F.; Ma, H.; Chen, J.; Qasim, K.; Ge, B.; Zhu, C.; Sun, L., Visualizing the electrochemical lithiation/delithiation behaviors of black phosphorus by in situ transmission electron microscopy. *The Journal of Physical Chemistry C* **2016,** *120* (11), 5861-5868.
66. Abate, Y.; Akinwande, D.; Gamage, S.; Wang, H.; Snure, M.; Poudel, N.; Cronin, S. B., Recent progress on stability and passivation of black phosphorus. *Advanced Materials* **2018,** *30* (29), 1704749.
67. Yau, S.-L.; Moffat, T. P.; Bard, A. J.; Zhang, Z.; Lerner, M. M., STM of the (010) surface of orthorhombic phosphorus. *Chemical physics letters* **1992,** *198* (3-4), 383-388.
68. Castellanos-Gomez, A.; Vicarelli, L.; Prada, E.; Island, J. O.; Narasimha-Acharya, K.; Blanter, S. I.; Groenendijk, D. J.; Buscema, M.; Steele, G. A.; Alvarez, J., Isolation and characterization of few-layer black phosphorus. *2D Materials* **2014,** *1* (2), 025001.
69. Sang, D. K.; Wang, H.; Guo, Z.; Xie, N.; Zhang, H., Recent developments in stability and passivation techniques of phosphorene toward next-generation device applications. *Advanced Functional Materials* **2019,** *29* (45), 1903419.
70. Lu, Z.; Jiang, K.; Chen, G.; Wang, H.; Cui, Y., Lithium electrochemical tuning for electrocatalysis. *Advanced Materials* **2018,** *30* (48), 1800978.
71. Sood, A.; Xiong, F.; Chen, S.; Wang, H.; Selli, D.; Zhang, J.; McClellan, C. J.; Sun, J.; Donadio, D.; Cui, Y., An electrochemical thermal transistor. *Nature communications* **2018,** *9* (1), 4510.
72. Piermarini, G.; Block, S., Ultrahigh pressure diamond-anvil cell and several semiconductor phase transition pressures in relation to the fixed point pressure scale. *Review of Scientific Instruments* **1975,** *46* (8), 973-979.
73. McMillan, P. F., New materials from high-pressure experiments. *Nature materials* **2002,** *1* (1), 19-25.
74. Mao, H.-K.; Hemley, R. J., New windows on the Earth's deep interior. *Reviews in Mineralogy and Geochemistry* **1998,** *37* (1), 1-32.

75. Mayanovic, R. A.; Jayanetti, S.; Anderson, A. J.; Bassett, W. A.; Chou, I.-M., Relaxation of the structure of simple metal ion complexes in aqueous solutions at up to supercritical conditions. *The Journal of chemical physics* **2003,** *118* (2), 719-727.
76. Badding, J.; Parker, L.; Nesting, D., High pressure synthesis of metastable materials. *Journal of Solid State Chemistry* **1995,** *117* (2), 229-235.
77. Rajapakse, M.; Musa, M. R. K.; Vithanage, D.; Abu, U.; Karki, B.; Yu, M.; Jasinski, J. B.; Sumanasekera, G., Vibrational Properties of Pristine and Lithium-Intercalated Black Phosphorous under High-Pressure. *Annalen der Physik n/a* (n/a), 2100187.
78. Gao, C.; Li, R.; Zhong, M.; Wang, R.; Wang, M.; Lin, C.; Huang, L.; Cheng, Y.; Huang, W., Stability and phase transition of metastable black arsenic under high pressure. *The Journal of Physical Chemistry Letters* **2019,** *11* (1), 93-98.
79. Ribeiro-Soares, J.; Almeida, R.; Cançado, L. G.; Dresselhaus, M. S.; Jorio, A., Group theory for structural analysis and lattice vibrations in phosphorene systems. *Physical Review B* **2015,** *91* (20), 205421.
80. Akahama, Y.; Kobayashi, M.; Kawamura, H., Raman study of black phosphorus up to 13 GPa. *Solid state communications* **1997,** *104* (6), 311-315.
81. Bao, H.-Q.; Li, R.-B.; Xing, H.-D.; Qu, C.; Li, Q.; Qiu, W., Crystalline orientation identification of phosphorene using polarized raman spectroscopy without analyzer. *Applied Sciences* **2019,** *9* (11), 2198.
82. Ali, A. S., Application of nanomaterials in environmental improvement. *Nanotechnology and the Environment* **2020**.
83. Biostructure, C. Scanning Electron Microscope Service. https://www.creative-biostructure.com/scanning-electron-microscope-service.htm.
84. Goldstein, J. I.; Newbury, D. E.; Michael, J. R.; Ritchie, N. W.; Scott, J. H. J.; Joy, D. C., *Scanning electron microscopy and X-ray microanalysis*. springer: 2017.
85. Abd Mutalib, M.; Rahman, M.; Othman, M.; Ismail, A.; Jaafar, J., Scanning electron microscopy (SEM) and energy-dispersive X-ray (EDX) spectroscopy. In *Membrane characterization*, Elsevier: 2017; pp 161-179.
86. Inkson, B. J., Scanning electron microscopy (SEM) and transmission electron microscopy (TEM) for materials characterization. In *Materials characterization using nondestructive evaluation (NDE) methods*, Elsevier: 2016; pp 17-43.
87. Dubrovinsky, L.; Dubrovinskaia, N.; Bykova, E.; Bykov, M.; Prakapenka, V.; Prescher, C.; Glazyrin, K.; Liermann, H.-P.; Hanfland, M.; Ekholm, M., The most incompressible metal osmium at static pressures above 750 gigapascals. *Nature* **2015,** *525* (7568), 226-229.
88. Weir, C.; Lippincott, E.; Van Valkenburg, A.; Bunting, E., Infrared studies in the 1-to 15-micron region to 30,000 atmospheres. *Journal of research of the National Bureau of Standards. Section A, Physics and chemistry* **1959,** *63* (1), 55.
89. Ackmann, P., *Diamonds in the rough: key performance indicators for reticles and design sets*. SPIE: 2008; Vol. 7122.
90. Gupta, Y.; Shen, X., Potential use of the ruby R 2 line shift for static high-pressure calibration. *Applied physics letters* **1991,** *58* (6), 583-585.
91. Piermarini, G. J.; Block, S.; Barnett, J. D.; Forman, R. A., Calibration of the pressure dependence of the R1 ruby fluorescence line to 195 kbar. *Journal of Applied Physics* **2008,** *46* (6), 2774-2780.

92. Barnett, J.; Block, S.; Piermarini, G., An optical fluorescence system for quantitative pressure measurement in the diamond-anvil cell. *Review of scientific instruments* **1973,** *44* (1), 1-9.
93. Shen, G.; Wang, Y.; Dewaele, A.; Wu, C.; Fratanduono, D. E.; Eggert, J.; Klotz, S.; Dziubek, K. F.; Loubeyre, P.; Fat'yanov, O. V., Toward an international practical pressure scale: A proposal for an IPPS ruby gauge (IPPS-Ruby2020). *High Pressure Research* **2020,** *40* (3), 299-314.
94. Syassen, K., Ruby under pressure. *High Pressure Research* **2008,** *28* (2), 75-126.
95. Villegas, C. E.; Rocha, A.; Marini, A., Anomalous temperature dependence of the band gap in black phosphorus. *Nano letters* **2016,** *16* (8), 5095-5101.
96. Yagmurcukardes, M.; Bacaksiz, C.; Unsal, E.; Akbali, B.; Senger, R. T.; Sahin, H., Strain mapping in single-layer two-dimensional crystals via Raman activity. *Physical Review B* **2018,** *97* (11), 115427.
97. Kandemir, A.; Iyikanat, F.; Sahin, H., Monitoring the crystal orientation of black-arsenic via vibrational spectra. *Journal of Materials Chemistry C* **2019,** *7* (5), 1228-1236.
98. Karki, B.; Freelon, B.; Rajapakse, M.; Musa, R.; Riyadh, S. S.; Morris, B.; Abu, U.; Yu, M.; Sumanasekera, G.; Jasinski, J. B., Strain-induced vibrational properties of few layer black phosphorus and MoTe2 via Raman spectroscopy. *Nanotechnology* **2020,** *31* (42), 425707.
99. Bindu, P.; Thomas, S., Estimation of lattice strain in ZnO nanoparticles: X-ray peak profile analysis. *Journal of Theoretical and Applied Physics* **2014,** *8*, 123-134.
100. Mote, V.; Purushotham, Y.; Dole, B., Williamson-Hall analysis in estimation of lattice strain in nanometer-sized ZnO particles. *Journal of theoretical and applied physics* **2012,** *6*, 1-8.
101. Sottmann, J.; Herrmann, M.; Vajeeston, P.; Hu, Y.; Ruud, A.; Drathen, C.; Emerich, H.; Fjellvag, H.; Wragg, D. S., How crystallite size controls the reaction path in nonaqueous metal ion batteries: the example of sodium bismuth alloying. *Chem Mater* **2016,** *28* (8), 2750-2756.
102. Zhang, C.; Yu, M.; Anderson, G.; Dharmasena, R. R.; Sumanasekera, G., The prospects of phosphorene as an anode material for high-performance lithium-ion batteries: a fundamental study. *Nanotechnology* **2017,** *28* (7), 075401.
103. Kohn, W.; Sham, L. J., Self-consistent equations including exchange and correlation effects. *Physical review* **1965,** *140* (4A), A1133.
104. Hohenberg, P.; Kohn, W., Inhomogeneous electron gas. *Physical review* **1964,** *136* (3B), B864.
105. Kresse, G.; Furthmüller, J., Efficient iterative schemes for ab initio total-energy calculations using a plane-wave basis set. *Physical review B* **1996,** *54* (16), 11169.
106. Blöchl, P. E., Projector augmented-wave method. *Physical review B* **1994,** *50* (24), 17953.
107. Perdew, J. P.; Burke, K.; Ernzerhof, M., Generalized gradient approximation made simple. *Physical review letters* **1996,** *77* (18), 3865.
108. Perdew, J. P.; Chevary, J. A.; Vosko, S. H.; Jackson, K. A.; Pederson, M. R.; Singh, D. J.; Fiolhais, C., Atoms, molecules, solids, and surfaces: Applications of the generalized gradient approximation for exchange and correlation. *Physical Review B* **1992,** *46* (11), 6671.

109. Moellmann, J.; Grimme, S., DFT-D3 study of some molecular crystals. *The Journal of Physical Chemistry C* **2014,** *118* (14), 7615-7621.

CURRICULUM VITA

Dinushika Vithanage

Education

Doctor of Philosophy in Physics (PhD) ***(2021 – 2023)***
Department of Physics & Astronomy, University of Louisville, KY - USA

Master of Science in Physics (MS) ***(2019- 2021)***
Department of Physics & Astronomy, University of Louisville, KY - USA

Bachelor of Science in Physics (BSc) ***(2013- 2017)***
Department of Physics, University of Peradeniya - Sri Lanka.

Work Experience

- Electrochemical cell assembly and testing using Voltammetry and Amperometry.
- Material characterization using scanning electron microscopy (SEM), Raman, Photoluminescence (PL), Fourier Transformation Infrared (FTIR) spectroscopy and X-ray diffraction (XRD).
- Synthesize two-dimensional (2D) materials including series of Arsenic-Phosphorous, Phosphorene, Mixed halides, 2D magnetic materials, Transition Metal Dichalcogenides (TMDs) and alloys using "Chemical Vapor Transport (CVT)" crystal growth technique.
- Measurement of thermoelectric power (analog subtraction method) and four-probe resistance of 2D materials.
- Conduct in-situ electrochemical intercalation and in-situ high-pressure experiments (using DAC) on 2D materials via Raman spectroscopy: Property modification of materials upon external factors.
- Operate and maintain ultra-high vacuum systems.
- Implement glassblowing for Pyrex and quartz using oxy-acetylene flame torch.
- Data Analysis: Origin Pro, MATLAB, Mathematica, GSAS II, Diffrac Eva, Match, Vesta, Fityk, Microsoft Office package.

Key Publications

- **Vithanage, D.**; Rajapakse, M.; Tasnim, K.; Musa, M. R. K.; Abu, U. O; Weerahennedige, H.; Yu, M; Sumanasekera, G.; Jasinski, J. B.; High-Pressure response of vibrational properties of b-As_xP_{1-x}: In-situ Raman studies. Nanotechnology Journal 2023
- **Vithanage, D.**; Rajapakse, M.; Tasnim, K.; Abu, U. O; Weerahennedige, H.; Yu, M; Sumanasekera, G.; Jasinski, J. B.; Electrochemical Li intercalation in b-As_yP_{1-y} alloys: In-situ Raman spectroscopy study. The Journal of Allys and Compounds (Under review).
- Abu, U. O.; **Vithanage, D.**; Vitharana, A.; Jasinski, J. B.; Sumanasekera, G., Degradation Studies of Air-Exposed Black Phosphorous and Black Arsenic Phosphorous. ChemEngineering 2023, 7 (2), 18.
- Arnold, W.; Shreyas, V.; Akter, S.; Li, Y.; Halacoglu, S.; Kalutara Koralalage, M. B.; Guo, X.; **Vithanage, D.**; Wei, W.; Sumanasekera, G., Highly Conductive Iodine and Fluorine Dual-Doped Argyrodite Solid Electrolyte for Lithium Metal Batteries. The Journal of Physical Chemistry C.
- Rajapakse, M.; Musa, M. R. K.; **Vithanage, D.**; Abu, U.; Karki, B.; Yu, M.; Jasinski, J. B.; Sumanasekera, G., Vibrational Properties of Pristine and Lithium-Intercalated Black Phosphorous under High-Pressure. Annalen der Physik n/a (n/a), 2100187.
- Abu, U. O.; Musa, M. R. K.; Rajapakse, M.; Karki, B.; **Vithanage, D.**; Yu, M.; Sumanasekera, G.; Jasinski, J. B., Vapor-Phase Intercalation of Cesium into Black Phosphorous. The Journal of Physical Chemistry C 2021, 125 (49), 27440-27448.

Oral & Poster Presentations

- "High-Pressure response of vibrational properties of b-As_xP_{1-x}: In-situ Raman studies", In American Physical Society, March meeting 2023.
- "Electrochemical Li Intercalation in BP and b-As_2P_3 alloy and High-pressure Studies of BP: Raman Spectroscopy Studies", In NNCI Nano + Additive Manufacturing Summit 2022
- "Electrochemical Li Intercalation in BP and b-As_2P_3 alloy and High-pressure Studies of BP: Raman Spectroscopy Studies", In Conn Center LAC Price Event, University of Louisville 2022
- "Li Intercalation Induced Phase Transition in As_2P_3", In Materials Research Society Fall Meeting & Exhibit, Virtual, 2022.
- "A study of thermal conductivity of composite building materials", In PGIS (Postgraduate Institute of Science) Research Congress, University of Peradeniya 2018.

Affiliations

- Member - Materials Research Society (MRS) (2021 - Present)
- Member - American Physical Society (APS) (2022 - Present)
- Coordinator - Sri Lankan Student Association of University of Louisville (2019 - 2022)
- Captain - University Karate Team (Women's), University of Peradeniya, Sri Lanka (2015)
- Vice-Captain - University Karate Team (Women's), University of Peradeniya, Sri Lanka (2014)
- Organizing Team - University Karate Fresher's Meet, University of Peradeniya, Kandy, Sri Lanka (2014, 2015)